이학박사 학위논문

Chemically and Electrically Modulated Scattering Response of Plasmonic Multicomponent Nanostructures

다조성계 플라즈몬 나노 구조의

화학 및 전기적 산란 신호 조절

2022년 2월

서울대학교 대학원

화학부 무기화학

김 재 호

Chemically and Electrically Modulated Scattering Response of Plasmonic Multicomponent Nanostructures

지도 교수 남 좌 민

이 논문을 이학박사 학위논문으로 제출함
2021년 12월

서울대학교 대학원
화학부 무기화학
김 재 호

김재호의 이학박사 학위논문을 인준함
2021년 12월

위 원 장 _____ 김 지 환

부위원장 _____ 남 좌 민

위 원 _____ 홍 병 희

위 원 _____ 임 종 우

위 원 _____ 오 정 욱

\

Abstract

Plasmon resonance, which is a coherent collective oscillation of conductive electrons in the presence of an external electromagnetic field, effectively enhances various optical processes by means of strong light-matter interactions. Especially, plasmonic nanomaterials scatter light with extraordinary efficiency and the increased far-field radiation intensity can be exploited for the advanced design of biosensors, colorimetric methods for naked-eye detection, and smart displays. However, the full potential of the scattering from plasmonic nanomaterials cannot be fully realized by single component-based nanostructures with monotonic and confined properties. On the contrary, multi-component-based systems exhibit diverse properties and opportunities owing to the synergistically combined physicochemical functions of individual components or new features arising from the integrated structures.

In this thesis, I present a chemical and an electrical strategy to modulate scattering response of plasmonic multi-component nanostructures and optimal examples of which showing benefits from the multicomponent systems. Chapter 1 introduces plasmonic properties of multicomponent nanostructures and following advantages of enhanced and modulated plasmonic scattering on applications. In Chapter 2, I developed a highly specific, well-defined Cu polyhedral nanoshell (CuPN) overgrowth chemistry and introduced to enhance light-scattering signal of Au

nanoparticle probes for bio-detection. The CuPNs are exclusively formed on the surface of Au nanoparticles in a controllable manner without any noticeable non-specific signal amplification. This newly developed polymer-mediated multicomponent core-shell formation chemistry was shown as a means of the development of the naked-eye-based highly sensitive and quantitative detections of DNA and viruses. Chapter 3 includes new-found anomalous electrochromic behaviors of Au nanocubes. Plasmon scattering of the nanocubes showed higher shift rate of resonance frequency at the highly negative potential range in reversible manner. This unexpected change beyond classical understandings was attributed to the material-specific quantum mechanical electronic structures of the plasmonic materials. The substantial role of quantum capacitance in plasmonic material, which can be derived from the density of states of the composing metals, was able to be verified for the first time by means of altering the surface element by forming Ag-Au core-shell nanocubes.

Keywords: plasmonic scattering, multicomponent nanoparticle, polyhedral core-shell nanoparticle, biosensor, naked-eye detection, electrochromism

Student Number: 2014-21221

Table of Contents

Self-Citations of the Prior Publications

A portion of this dissertation have appeared in the following papers reported by Jae-Ho Kim as an author under the advice of Prof. Jwa-Min Nam:

In Chapter 1,

"Multicomponent Plasmonic Nanoparticles: From Heterostructured Nanoparticles to Colloidal Composite Nanostructures", M. Ha†, J.-H. Kim†, M. You†, Q. Li, C. Fan, and J.-M. Nam*, *Chemical Reviews* 119, 12208 (2019).

"Surface-Enhanced Raman Scattering-Based Detection of Hazardous Chemicals in Various Phases and Matrices with Plasmonic Nanostructures", J. Choi†, J.-H. Kim†, J.-W. Oh*, and J.-M. Nam*, *Nanoscale* 11, 20379 (2019).

"Metal Nanoparticles for Virus Detection", J.-E. Park†, K. Kim†, Y. Jung†, J.-H. Kim†, and J.-M. Nam*, *ChemNanoMat* 2, 927 (2016).

In Chapter 2,

"Sensitive, Quantitative Naked-Eye Biodetection with Polyhedral Cu Nanoshells", J.-H. Kim†, J.-E. Park†, M. Lin†, S. Kim, G.-H. Kim, S.

Park, G. Ko, and J.-M. Nam*, *Advanced Materials* 29, 1702945 (2017).

"Transformative Heterointerface Evolution and Plasmonic Tuning of Anisotropic Trimetallic Nanoparticles", M. Lin, G.-H. Kim, J.-H. Kim, J.-W. Oh, and J.-M. Nam*, *Journal of the American Chemical Society* 139, 10180 (2017).

In Chapter 3,

"Nontrivial, Unconventional Electrochromic Behaviors of Plasmonic Nanocubes", J.-H. Kim†, S. Cha†, Y. Kim†, J. Son, J.-E. Park, J.-W. Oh* and J.-M. Nam*, *Nano Letters* 21, 7512 (2021).

"Electrochromic Response and Control of Plasmonic Metal Nanoparticles", Y. Kim, S. Cha, J.-H. Kim, J.-W. Oh, and J.-M. Nam*, *Nanoscale* 13, 9541 (2021).

† Represents equal contribution.

\

\

Chapter 1

Introduction: Plasmonic Scattering of Multicomponent Nanostructures

1.1. Light Scattering of Plasmonic Nanomaterials

Being able to modulate light freely might be the biggest dream mankind ever had since being able to handle heat. For the best control of light, an optimal substance will be required. When light interacts with a material, it can pass by (transmission), revert the path (reflection), or diffused (scattering) elastically. The other chance is to lose initial energy of the light and transform it into the internal energy of the substance and this is what we call absorption. The incident light energy is conserved and fractionally converted into the sum of absorbance, reflectance, and transmittance. In plasmonic materials, delocalized electrons can oscillate collectively and coherently in the presence of an externally propagating electromagnetic field. This collective oscillation, that exists at the interface between two materials where the real part of the dielectric permittivity changes its sign across the interface, is called as surface plasmon. While the surface plasmon propagates along the metal-dielectric or metal-air interface, the resonant energy can be either absorbed by materials or evanescently scattered into the space.

The simplest model for understanding this phenomenon is the Drude model based on Maxwell's equation in which the plasma frequency is determined by the dielectric functions of materials at the interface:

$$\varepsilon(\omega) = \varepsilon_{\infty} - \frac{\omega_p^2}{(\omega^2 + i\gamma\omega)} \qquad \textbf{(1.1)}$$

Here, γ represents the damping constant, ω_p is the Drude plasma frequency, and ε_∞ is dielectric constant at infinite frequency.

When the light comes into an object with limited size as a nanoparticle, only certain resonances corresponding to standing waves survive destructive interference and we call these modes as localized surface plasmon resonance (LSPR). The LSPR property is initially decided by the size and shape of a plasmonic particle and the scattering from the particle can be quantitatively described especially well for the spherical shapes.[1] A complete analytical solution of Maxwell's equations for the scattering of electromagnetic wave by particles of any relative size to wavelength was initially established by Gustav Mie in 1908.[2,3] According to the Mie theory, quasistatic description of the scattering cross-section from the dipole resonance can be expressed as,

$$Q_{sc} = \frac{8}{3} q^4 \left| \frac{\varepsilon_d - 1}{\varepsilon_d + 2} \right|^2 \approx \frac{8}{3} \frac{\omega_{SP}^4}{(\omega^2 - \omega_{SP}^2) + (4/9)\, q^6 \omega_{SP}^2} q^4 \qquad \textbf{(1.2)}$$

where q is the dimensionless size proportional to the particle radius, ε_d is the relative dielectric function which is the ratio of dielectric function of the particle and that of the medium ($\varepsilon_{d=}\varepsilon_p/\varepsilon_m$), and ω_{sp} is the frequency of the

dipole surface plasmon. The left formula derived from the quasi-static approximation implies that as the particle size increases, the scattering dramatically increase with roughly by the fourth power while the resonance gradually red shifts. The scattering efficiency would dominate over the absorption efficiency in an overall extinction of light as the nanoparticle size increases.

For larger particles with size comparable to the wavelength of light, quasi-static approximation breaks down due to retardation effects and fully rigorous electrodynamic interpretation is required. Near the resonance frequency, the scattering efficiency of the dipole term decreases as the particle size increases. The overall shift toward lower energies and high-order modes can minimize the absorption represented as interband transitions.

Particles with size negligible to the wavelength of light show absorption-dominant damping of plasmon and such particles will be difficult to be detected by light scattering. A relatively larger proportion of the electromagnetic field will penetrate inside the metal body due to the higher surface-to-volume ratio and results more loss of light energy. Such small particles efficiently convert light energy into energetic hot-carriers or heat; thus, they are promising for photocatalysts, energy harvesting, or photothermal applications.[4] The efficiency can be even improved by enhanced electromagnetic field vis near-field coupling. In addition, small particles are advantageous for colloidal dispersion, bio-chemical collision,

biocompatibility, and renal excretion.

Experimentally there are several ways to measure the scattering signal from plasmonic nanoparticles. Dark-field microscopy is one of the most efficient ways to image the position and scattering color of a material especially with a scale near or smaller than the diffraction limit of light (**Figure 1.1**). Dark-field condenser allows only the scattered light from the specimen to enter objective lens while the most part of the directly transmitted lights be blocked and refracted. The far-field of the scattered light from plasmonic nanoparticles can be imaged, collected, and interpreted by photodetectors such as charge-coupled devices (CCD) or photomultiplier tubes (PMT) connected to a spectrometer.

In conclusion, it is better to exploit large and anisotropic nanoparticles and optimize their plasmonic scattering properties for applications such as sub-wavelength optoelectronic devices, waveguides, super-lenses, data storage, light generation, microscopy, bio-imaging, and bio-photonics.

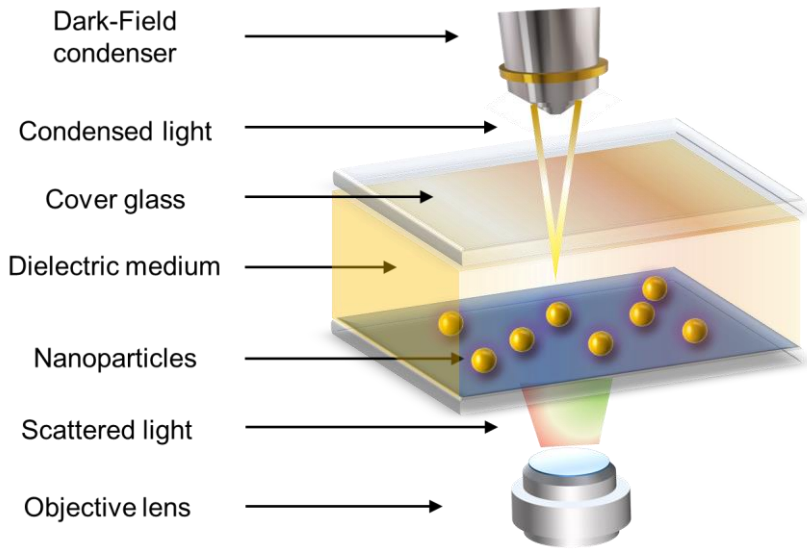

Figure 1.1. Representative set-up of dark-field microscopy for measuring scattered light of plasmonic nanoparticles.

1.2. Plasmonic Multicomponent Nanostructures

Plasmonic nanostructures possessing unique and versatile optoelectronic properties have been vastly investigated over the past decade. There are some materials known to have plasmonic property which have a negative real part of dielectric permittivity. However, only gold and silver has been dominantly used for applications owing to the chemical inertness, low biological cytotoxicity, and Au-S affinity-based facile surface functionalization strategies.[5] Other metals such as aluminum or alkali metals show promising optical properties with acceptably low loss, but their use has been limited yet due to the lack of reliable chemical approaches.[6]

Different real and imaginary part of the dielectric permittivity for different materials determine plasma frequency and absorption properties of a plasmonic nanostructure. Especially, the quality of plasmon in a material is mainly governed by three intrinsic parameters and they are carrier concentration, carrier mobility, and interband losses (**Figure 1.2**).[6] The carrier concentration has to be high enough to provide negative real permittivity. Although slightly tunable by geometrical factors, the LSPR frequency is primarily controlled through the free carrier concentration (n) of the composing material modulated by its high frequency dielectric constant (ε_∞).[7] As simply derived from the Drude model as **Equation 1.3**, there is a positive correlation between carrier concentration (n) and plasma

frequency (ω_p):

$$\omega_p = \sqrt{\frac{ne^2}{\varepsilon_0 m^*}} \qquad \textbf{(1.3)}$$

In this principle, the LSPR frequencies of various materials span from visible to infra-red region (**Figure 1.3**). Meanwhile, lower carrier mobilities and higher interband losses translate to higher material losses and lower quality plasmon. Thus, it is desirable to find a plasmonic material or composite of them with high carrier mobility, suppressed interband loss, and optimized carrier concentration for use in various applications.

Yet, the full potential of plasmonic nanostructure has not been fully exploited, particularly with single-component homogeneous structures with monotonic properties. On the contrary, multi-component-based systems can exhibit diverse properties and additional opportunities owing to the synergistically combined physicochemical functions of individual components or new features arising from the integrated structures (**Figure 1.4**).[8] Plasmonic multicomponent nanoparticles, consisting of a highly conductive metal in addition to dielectric, semiconducting, or other metallic components of different shapes or sizes, exhibit synergistic and new plasmonic properties, which cannot be achieved by the physical mixture of single components. The newly emerging or improved properties can be achieved by integrating the intrinsic properties of individual components,

such as their plasmonic behavior, band structures, dielectric constants, or by induction of heterointerfaces. The complexity, unprecedented controllability, and multifunctionality of multicomponent nanoparticles can guide us to new directions in plasmonic applications. Here, the multicomponent nanostructures can be defined as hybrid structures composed of two or more distinctly definable condensed nanoscale domains, which are different in material compositions.

As mentioned above, it should be noted that new designs and precisely controlled synthesis of plasmonic multicomponent nanostructures are less readily realizable especially in the colloidal phase via wet chemistry and bottom-up approach. There is a long way to go for the synthetic mechanisms of various multicomponent nanomaterials to be understood. However, some chemically direct and assembly-mediated synthetic strategies, such as heteroepitaxial growth, galvanic replacement, ion exchange, physicochemical adsorption, and DNA-mediated self-assembly, have been proposed and proven successful for the preparation of intricate multicomponent nanostructures (**Figure 1.5**).[9,10] For plasmonic noble metals, galvanic replacement is a promising technique to prepare more complex structures especially with hollow body or holes. Ion exchange is also an important tool for diversifying crystal structures of plasmonic compound semiconductors or dielectric domains interfacing with plasmonic metal.

To enhance and modulate scattering property of a plasmonic material, one of the most important principles to directly synthesize a

multicomponent nanoparticle is heterogeneous nucleation. During the heterogeneous nucleation process, monomers of growing material can condense on the pre-synthesized seed. The surface of the seed provides a stable and wettable site for the secondary material and lowers the thermodynamic energy barrier compared to the self-nucleation. Here, the mismatch between the lattice constants of the nucleating crystal and the substrate plays a decisive role in determining the final shape and crystallinity of the multicomponent structure as well as in the energy barrier of heterogeneous nucleation.[11] The surface energy of a particle in a medium is the key factor in deciding whether to form core-shell or Janus-type structures (**Figure 1.6**). During the heteroepitaxial growth, lattice stress across the heterointerface can decide the growing tendency and transform the shape of multicomponent nanostructures, as shown in the case of morphological change from a core-shell to a Janus structures during strain relaxation of Au shells on Pt-based seeds.[9] Finely engineered heterogeneous nucleation and chemical potential incorporated with electrochemistry can even enable designing multicomponent nanoparticles with 3 or more components in desired structures, such as Au-Cu-Ag multi-metallic anisotropic nanoparticles.[12]

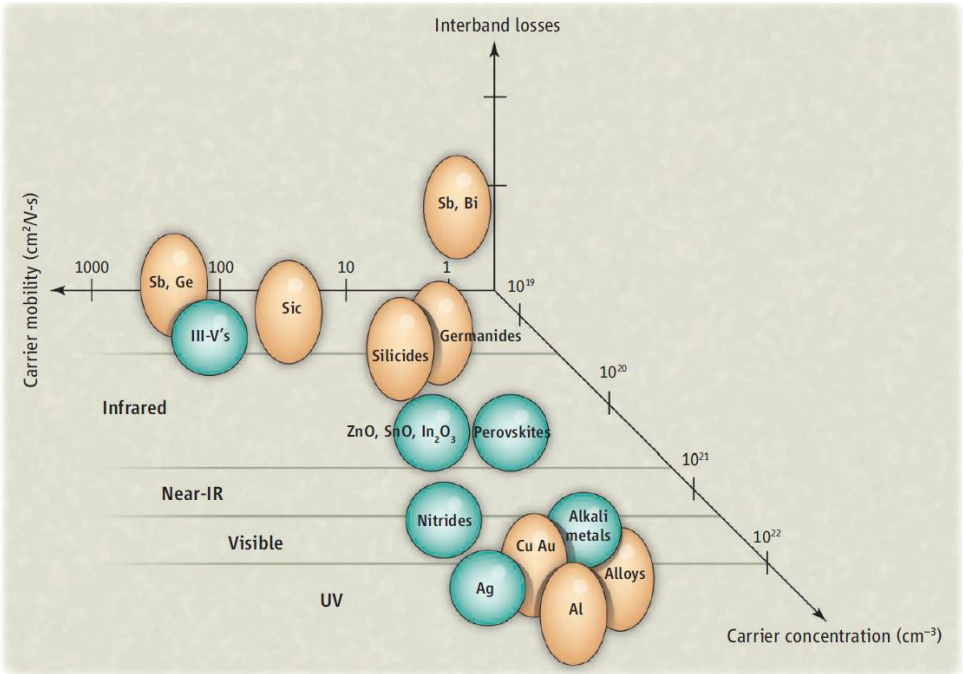

Figure 1.2. Plasmonic metamaterials map with three plasmonic property-deciding parameters for the axis.[6]

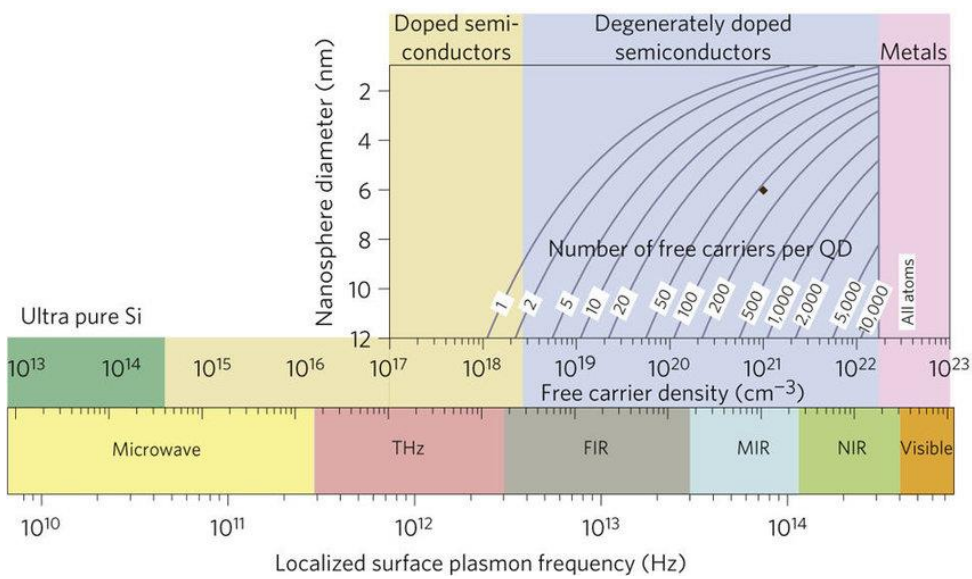

Figure 1.3. Localized surface plasmon resonance frequency dependency on free carrier density and doping constraints of materials.[7]

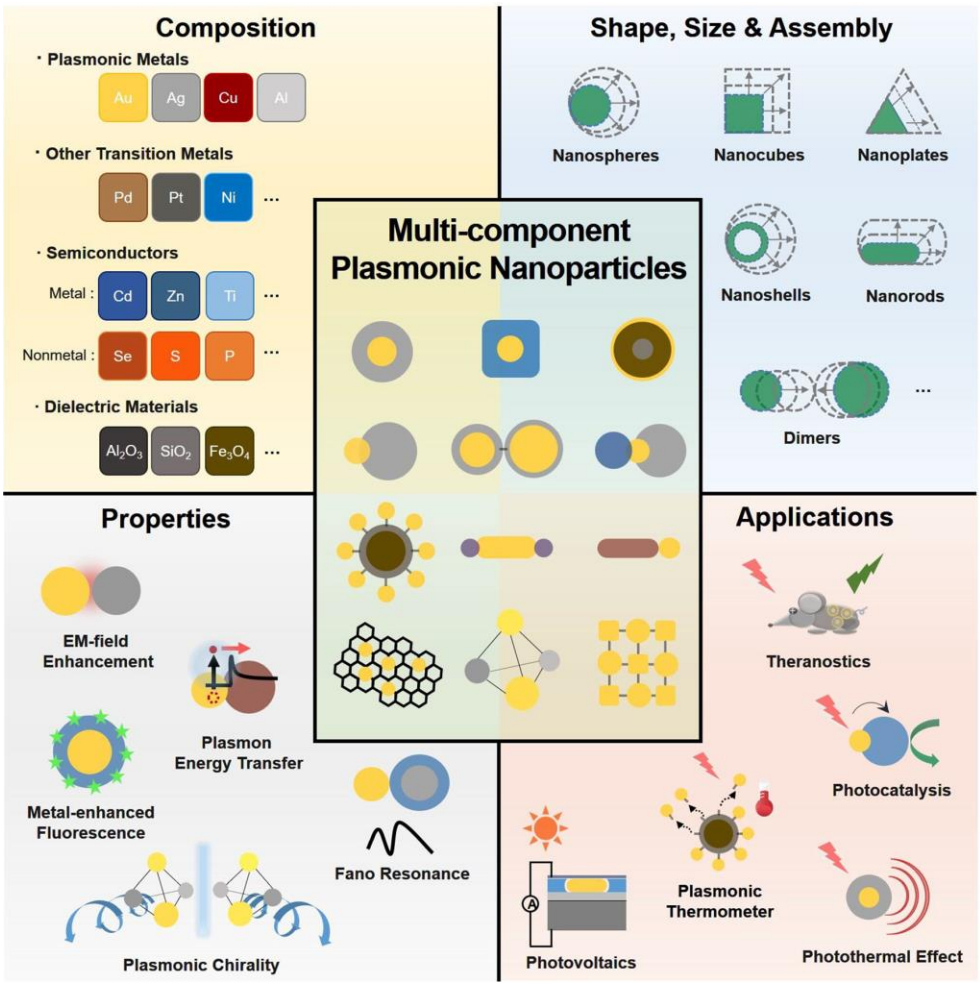

Figure 1.4. Chemical compositions, geometrical morphologies, properties, and applications of multicomponent plasmonic nanomaterials [8]

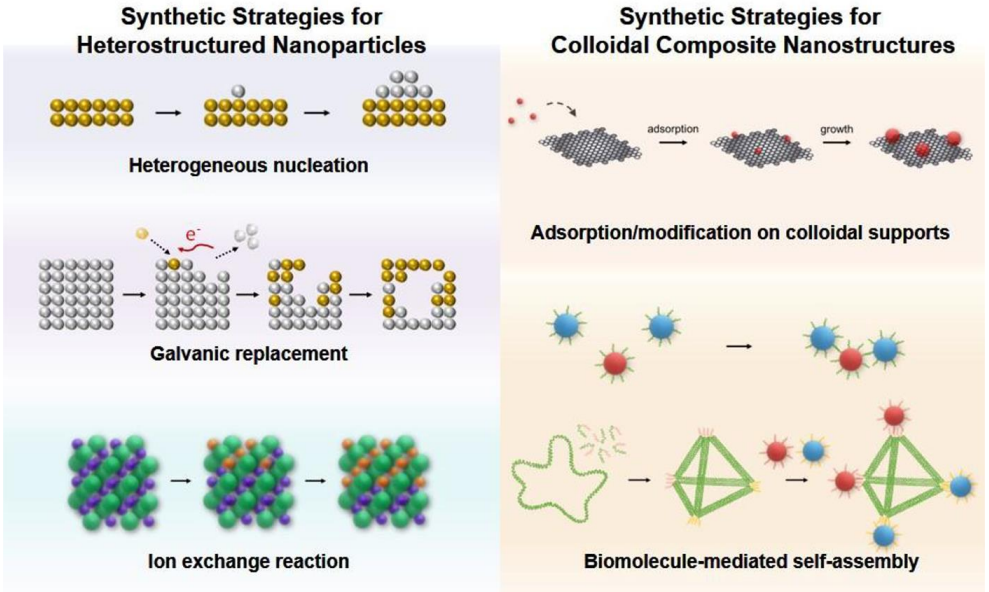

Figure 1.5. Schematic illustration of synthetic strategies for multicomponent plasmonic nanostructures.[8]

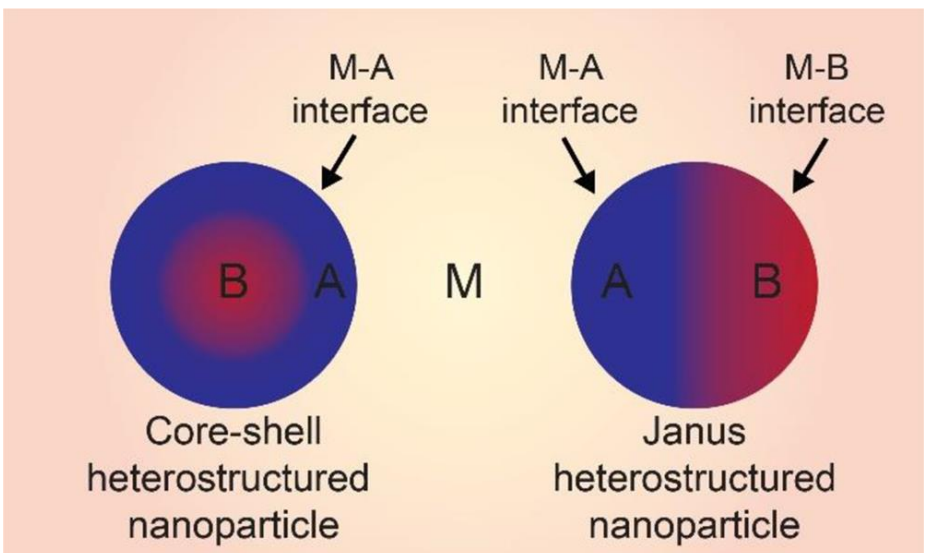

Figure 1.6. Schematic illustration of heterostructured core−shell nanoparticles with M-A interface and Janus nanoparticle with M-A and M-B interface in a medium M.[8]

1.3. Plasmonic Scattering Modulation for Applications

During the plasmon resonance, charge density on the surface can be dramatically increased or decreased. This forms highly condensed electromagnetic field near the surface of plasmonic material, increasing light-matter interaction and enhancing optical processes in the peripheral dielectric environment as well. Plasmonic nanoparticle can have absorption and scattering cross-section much larger than the actual physical size of a particle. Especially in case of plasmonic scattering, optical intensity of a metallic nanoparticle can easily overwhelm that of a molecule. Plasmonic scattering changes direction of radiation, elongates light path, re-radiates incident light strongly, or improves photonic transition process efficiencies.

In the spectroscopical point of view, plasmon-enhanced optical processes can be classified into a few categories. Initially, light can be absorbed or scattered by a plasmonic material, and the effect becomes greater in the nanoparticles. Then, the amplified electromagnetic field on the surface of plasmonic material enhances electronic and vibrational transition probability in the peripheral areas. Through these processes, plasmonic nanomaterial can be used as probes for biosensors, substrates for surface-enhanced Raman scattering (SERS), or auxiliary substances to increase the quantum efficiency of solar cells or quantum dots. Among these, the most

frequently found examples to date where plasmonic particles used for applications were biosensors using plasmonic light-scattering and SERS-based spectroscopies. Especially, metallic nanoparticles have been used to visualize virus detections or enhance specific vibrational signals from traces of toxic molecules.[13,14] Such infectious and acute biomaterials or toxic chemicals with low lethal doses pose a threat to public health (**Figure 1.7**).[15] Thus, it is urgent to develop a new detection method capable of on-site detection, high sensitivity, and simple visualization. Even for display or energy absorption purposes, there remains a lot of potential for improvement using the plasmonic scattering. Thus, now it is wise to discover methods to effectively enhance, quantitatively control, and optimize the scattering of plasmonic nanomaterials.[16]

There are several advantages of modulating the scattering signal. By adjusting the resonance frequency of plasmonic particles, we may tune visible color of the scattering. This confers new functions on biosensors such as diversified colors for multiplexing, avoided absorption band of a matrix, or ability to detect surface chemical conditions. It is also possible to maximize the radiation signal from a fluorophore by fitting the plasmon frequency resonantly to the excitation or emission of the dye. In case of adjusting the scattering intensity, we may amplify the signal to enhance sensitivity for improved detection limit, faster detection process, simplified image recording, or naked-eye visible signals.

The intensity and resonance frequency of plasmonic scattering are

determined by the regional geometry and chemical condition of nanomaterials. There are several common ways to modulate and best optimize the scattering of plasmonic nanomaterials (**Figure 1.8**). First, one can readily control the plasmonic scattering intensity and the wavelength by changing the size and geometrical shape of a plasmonic nanoparticle. One can prepare anisotropic nanoparticle or enlarge the nanoparticle dimension by appropriately applying heterogeneous nucleation on colloidal chemistry. Plasmon resonance modes can also be finely tuned with enhanced electromagnetic near field by placing two or more plasmonic nanoparticles closely. Even charge transfer plasmon mode can be reversibly controlled by switching between capacitive and conductive electronic coupling of LSPR of core-shell nanoparticles.[17] Resonance frequency and damping of plasmon is also deeply influenced by the dielectric constant on the surface. Various dielectric environment can be introduced on the surface of plasmonic nanoparticles as a shell. It is also possible to electrochemically control the color of plasmonic scattering by encapsulating plasmonic nanoparticles with electrochemically active molecular layers (**Figure 1.9,** top left).[14] Electrically driven color-changing of plasmonic metasurfaces was demonstrated to be a promising platform for a next-generation smart display with ultra-thin and low-power features.[18] Plasma frequency and quality of plasmon highly depends on the surface element of plasmonic nanoparticles as well. Exposed surface element can be exchanged by forming a thin film on a substrate or a thin shell on a nanoparticle. For initiation, there are a few

examples of thermodynamically favored underpotential depositions reported for coinage metals forming a thin atomic shell on other metals. Moreover, density of free carriers participating in plasmon resonance can be electrically controlled through capacitive charging and discharging (**Figure 1.9**, lower left). The physical principles behind these approaches are all in accordance with the previously introduced Mie theory and the following equation (2). In electrochemical point of view, plasmonic metal interfaces with an electrode on the one side and a medium on the other side which can be an electrolyte. The Fermi level of the metal maintains equilibrium with the chemical potential of the environment by constantly exchanging charges.[19] Within this field of Plasmoelectronics, resonance frequency, spectral broadness, and radiative intensity of plasmonic scattering can be electrically and electrochemically tuned for desiring applications.[20] At this moment, it is worthwhile to discover an optimal chemistry to prepare multicomponent plasmonic nanoparticles and electrochemical methods to modulate plasmonic scatterings so that the newly emerging and beneficial to be efficiently utilized.

In this thesis, I present a chemical and an electrical strategy to modulate scattering response of plasmonic multi-component nanostructures and optimal examples of which showing benefits from the multicomponent systems (**Figure 1.10**). Chapter 1 introduces plasmonic properties of multicomponent nanostructures and following advantages of enhanced and modulated plasmonic scattering on applications. In Chapter 2, I developed a

highly specific, well-defined Cu polyhedral nanoshell (CuPN) overgrowth chemistry and introduced to enhance light-scattering signal of Au nanoparticle probes for bio-detection. The CuPNs are exclusively formed on the surface of Au nanoparticles in a controllable manner without any noticeable non-specific signal amplification. This newly developed polymer-mediated multicomponent core-shell formation chemistry was shown as a means of the development of the naked-eye-based highly sensitive and quantitative detections of DNA and viruses. Chapter 3 includes new-found anomalous electrochromic behaviors of Au nanocubes. Plasmon scattering of the nanocubes showed higher shift rate of resonance frequency at the highly negative potential range in reversible manner. This unexpected change beyond classical understandings was attributed to the material-specific quantum mechanical electronic structures of the plasmonic materials. The substantial role of quantum capacitance in plasmonic material, which can be derived from the density of states of the composing metals, was able to be verified for the first time by means of altering the surface element by forming Ag-Au core-shell nanocubes.

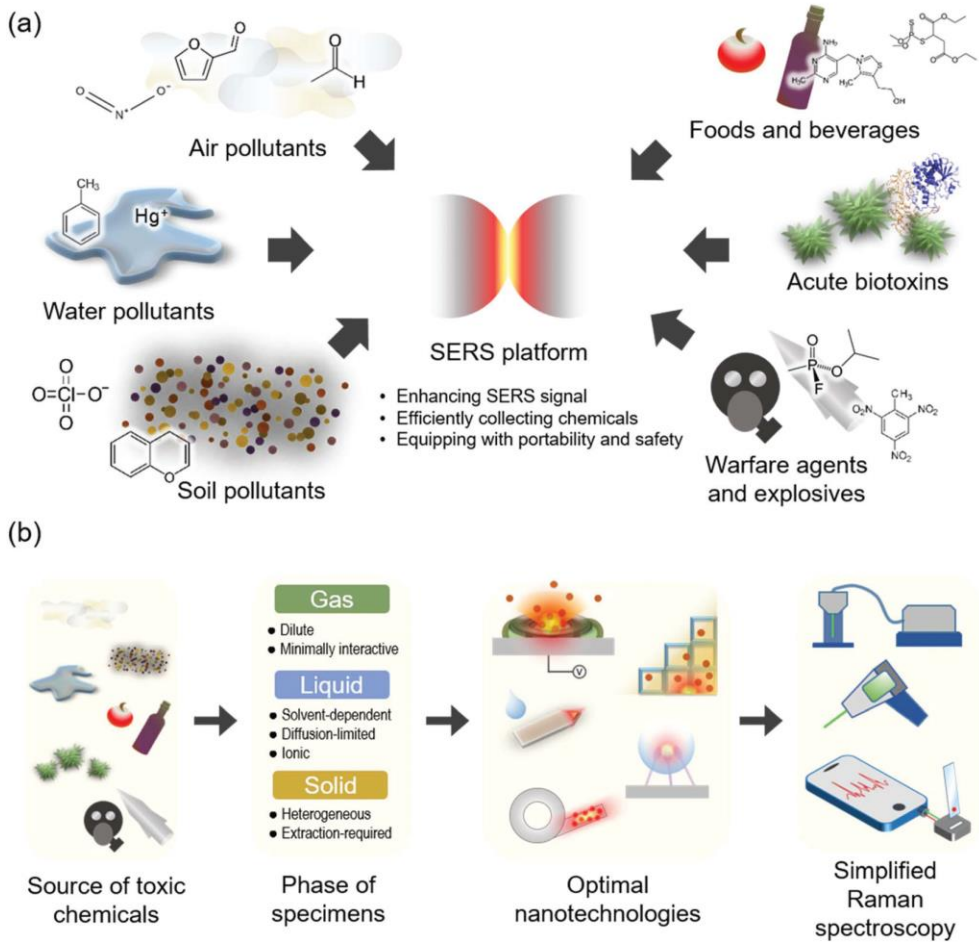

Figure 1.7. Schematic illustration of SERS-based environmental biochemical hazard detection strategies.[15]

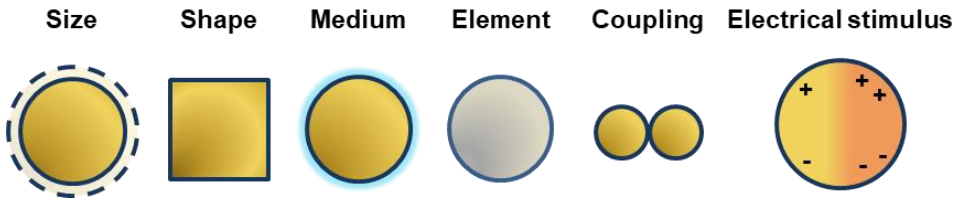

Figure 1.8. The six most common ways to control plasmon resonance and the following scattering property.

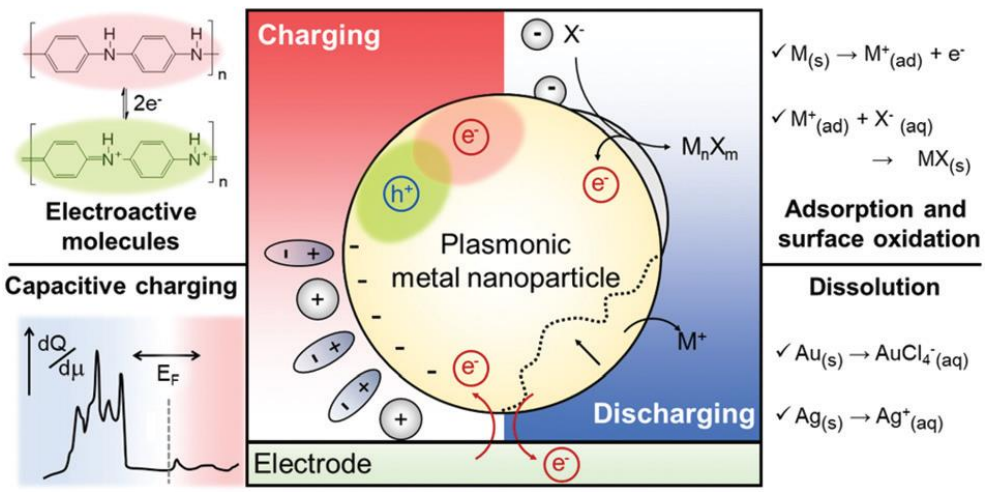

Figure 1.9. Mechanisms of electrochromic responses in plasmonic metal nanoparticles. Functional molecules on the nanoparticle surface can induce color change. The representative molecule is PANI (upper left). Electrochemical events occurring near the nanoparticle surfaces change the capacitance of the systems as well as dielectric functions of the constituent metal and surrounding medium. Adsorption and formation of metal halides or oxides are involved in this electrochromic process (upper right). Capacitive charging, according to the applied bias, changes the free electron density on the nanoparticle surface and thus, the LSPR is altered. At high cathodic voltages, the shape of DOS is of significance to the LSPR modulation (lower left). The nanoparticle can be dissolved above a particular anodic voltage and the corresponding morphology change can cause electrochromic effects (lower right)Schematic illustration of synthetic strategies for multicomponent plasmonic nanostructures.[14]

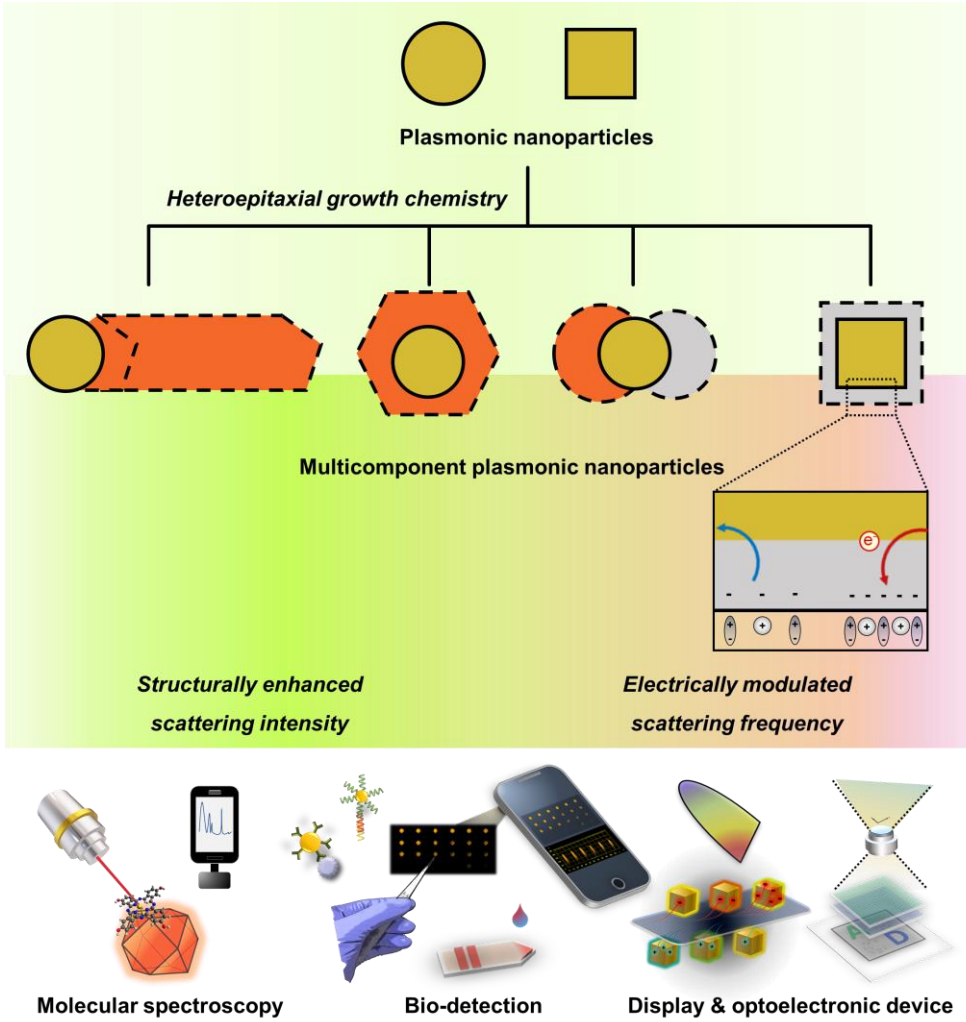

Figure 1.10. Schematic illustration of chemical and electrical strategies to modulate scattering response of plasmonic multi-component nanostructures and optimal examples of which showing benefits from the multicomponent system.

Chapter 2

Polyhedral Cu Nanoshell Formation Chemistry for Bio-Detections

2.1. Introduction

Nanoparticles (NPs) such as AuNPs have wide applications in chemical and biological detection, labeling, and imaging due to their compatible size, large surface area, availability of various conjugation methods, richness in core–shell chemistry, as well as structure dependent localized surface plasmon resonance and plasmonic coupling properties.[5,21-23] In particular, colloidal NP-based rapid on-site bio-detection ranging from bacteriological weapons to infectious diseases is in great need for human health and safety,[24,25] but the intrinsic optical properties of individual NP probes are, however, insufficient to detect targets at trace levels. Further, the simplicity, assay speed, and portability are critical elements, especially in developing fast but reliable naked eye-based bioassays.[26-28] To address these issues, Ag shell enhancement, known as silver staining,[29,30] has been extensively studied so far to intensify scattering signals from enlarged Ag shell structures formed on AuNP probes used as detection labels.[31-36] However, the lack of probe specificity and controllability of Ag shell enhancement limited its practical applications.[37]

In this chapter I demonstrated versatility and effectuality of the metal-polymer complex-mediated heteroepitaxial Cu growth chemistry on versatile Au nanoparticles to form Au-Cu multicomponent nanostructures (**Figure 2.1**). Enhanced Mie scattering intensity from the enlarged body volume of Au-Cu multicomponent nanostructures are used for naked-eye

bio-detection of DNA microarray and Virus immunoassay results. In specific, here we developed a highly controllable polyethyleneimine (PEI)-mediated Cu polyhedral nanoshell (CuPN) formation chemistry, specifically formed on AuNP probes, and used this CuPN formation method for straightforward, intensive, and quantifiable optical signal enhancement in bio-detections (**Figure 2.2**). The signals were readily detectable with naked eyes or an ordinary smartphone camera. In the case of DNA assay (anthrax sequence), we detected 8×10^{-15} M DNA on a microarrayed DNA chip with a dynamic range from 8×10^{-15} M to 800×10^{-12} M in this manner. For virus detection (norovirus target in this case), clinical stool samples, confirmed from polymerase chain reaction, were used, and as low as 2,700 virus copies were detected with greater than two orders of dynamic range. The high sensitivity and quantification capability of this CuPN assay were superior to any other previously reported bio-detection assays detectable with naked eyes. The Cu nanoshell formation chemistry provides a new paradigm in controlling Cu shell structures and their use in bio-detections.

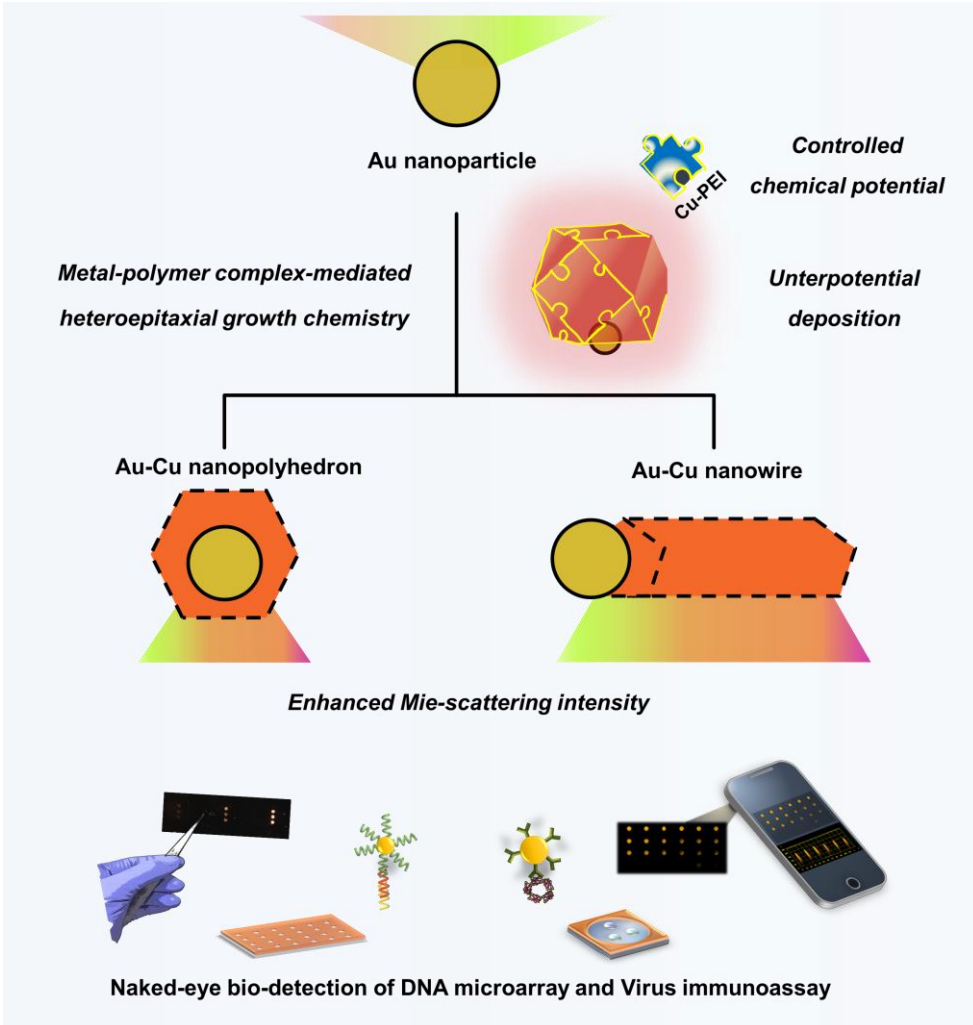

Figure 2.1. Schematic illustration of metal-polymer complex-mediated heteroepitaxial growth chemistry for Mie scattering intensity enhancement toward naked-eye bio-detection of DNA microarray and Virus immunoassay results.

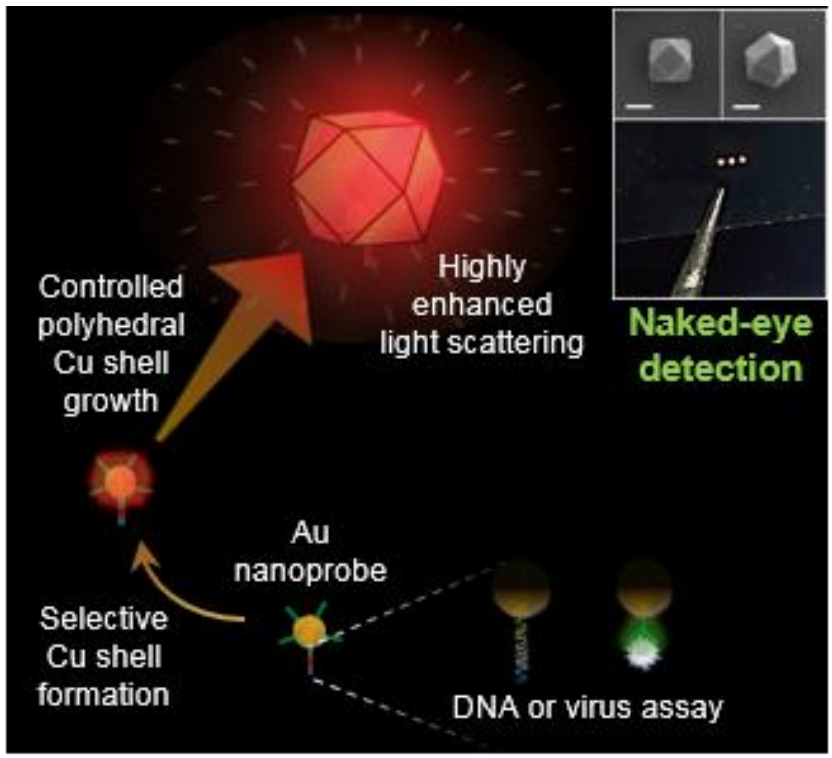

Figure 2.2. Simplified schematic strategy of the Cu overgrowth chemistry for the light-scattering signal enhancement on AuNPs for the naked-eye bio-detections.

2.2. Experimental Methods

Basis of the Experimental Design

The CuPN formation procedure benefits from the PEI-controlled Cu nanostructure overgrowth with negligible nonspecific binding or self-nucleation. The precursor solution contains Cu^{2+} ions and PEI, and this amine-rich polymer forms strong metal–ligand chelate complexes with free Cu^{2+} ions to stabilize the chemical potential of the reactants and lowers free ion concentrations.[38] In this manner, free nucleation and reduction are highly restricted in solution over a wide range of reducing power, and unwanted growth can be prevented. The optimal reduction potential of sodium l-ascorbate can be tailored such that it is sufficiently strong to form Cu shells on AuNP surfaces but still minimizing the direct reductions from copper–PEI complexes. As schematized in **Figure 2.3**, only when the AuNP label is provided as a catalytic surface does Cu begin to overgrow via underpotential deposition on AuNPs (**Figure 2.4**). The activation energy for the reduction of the stable Cu complex is only overcome in the presence of the NPs, while such moderate control on the reduction chemistry has not been successfully realized with noble metals.[39,40] It should be also noted that the amine functionality of the PEI works not only as a complexing agent in solution but also as a capping agent on the surface of CuPNs (**Figure 2.5**). Varying affinities of amine functional group to different facets of Cu crystal

result in polyhedral structures.[41] In particular, the preferential binding of amines to the Cu(100) surface would deactivate the facet more than those with higher-order Miller indices, and promote ⟨111⟩ directional growth to yield a particular proportion of polyhedron facets under a local minimum. Further, most Cu nanostructures are non-plasmonic Cu oxide structures or poorly controlled particles with low structural precision and low synthetic yield.[42] This PEI-mediated overgrowth method reported here enables controlled synthesis of Cu nanostructures in aqueous solution. The actual enhancement reaction completes within 10 min, and dramatically enhanced light trapping and scattering from enlarged metallic bodies in a highly controlled manner enables us to see clear reddish-orange-colored signals that stably remain for months.

In situ DF measurement of CuPN growth

One-dimensional flow cell was set up by assembling a bottom aldehyde-modified glass and a top slide glass with two holes (inlet and outlet holes) with a sandwiched thermo-spacer by heating at 120 °C on a digital hot plate. The flow cell was loaded onto the DF microscope (Axiovert 200M, Carl Zeiss, Germany) to observe in situ Cu shell formation while adding the CuPN enhancement solution. Amine-functionalized PEG (M.W. 2,000)-modified single-crystalline 50-nm AuNPs (8 pM) were injected into the flow cell and covalently linked on the aldehyde glass. After

10 min incubation, the unbound AuNPs were washed out with DI water (18.2 MΩ). The initial positions of bound AuNPs have been identified under the DF microscope with 12 V voltage applied to tungsten-halogen lamp. Next, we prepared growth solution (5 mL of 0.1 M $CuCl_2$, 5 mL of 1% PEI, and 25 mL of 0.5 M sodium L-ascorbate) in a 50-mL conical tube and directly inject 100 μL into flow cell. The real-time Cu growth over AuNP were monitored under light illumination from 4 V voltage applied to tungsten-halogen lamp.

AuNP probe preparation for anthrax DNA assay

A 5'-thiolated oligonucleotide (5'-SH-A_{10}-PEG_{18}-AAT GCT TTA TTC CAT TCC TGA TTT ATA TTT AAC TGT GCT T-3') complementary to the target sequence was used as a probe. The probe oligonucleotide was mixed with well-dispersed 13-nm citrated AuNPs which have been synthesized through conventional seed-mediated growth. The salt concentration was gradually increased to 0.15 M by adding 2.0 M sodium chloride under a hot bath. The mixture was centrifuged at 17,000 rpm for 40 min, the supernatant was removed, and this process was repeated three times. The probe particles were redispersed in 1× PBS buffer solution with 0.1% sodium dodecyl sulphate (SDS) and diluted to 500 pM before use.

Anthrax DNA assay procedure

The overall procedure of CuPN-based oligonucleotide microarray assay signal enhancement is schematically depicted as **Figure 2.6**. Here, an 80-bp DNA fragment from anthrax lethal factor was chosen as an oligonucleotide sequence. First, three equivalent spots containing the capturing oligonucleotide with an amine-modified 5' end was printed on the aldehyde-modified glass substrate (LSAL-S, Luminano, Seoul, Korea). The capturing oligonucleotide (5 μM) (5'-CTT GAA TTT TTG TAT CTA TTT TAC TCT TTG GCA CTA CTT T-PEG_{18}-C_6 Amine-3') with 0.15 M NaCl, 0.01% SDS, and 5% glycerol in carbonate buffer (pH 10) was loaded on the aldehyde-modified glass substrate using a microarray system. An array with three identical spots of the capturing oligonucleotide with a diameter of approximately 500 μm was placed in a humid chamber overnight. The capturing sequence was immobilized on the substrate by covalent chemical linking through an imine intermediate. The slide was then washed with 1 × PBS containing 0.1% SDS and associated with a silicon hybridization chamber (JTR12R-0.5 Silicone Isolators, Grace Bio-Labs, Oregon, USA). Then, the target oligonucleotide was applied to hybridize the capturing oligonucleotide, followed by the probe oligonucleotide on 10-nm AuNPs. The target oligonucleotide (20 μL), i.e., an anthrax lethal factor DNA fragment (5'-AAA GTA GTG CCA AAG AGT AAA ATA GAT ACA AAA ATT CAA GAA GCA CAG TTA AAT ATA AAT CAG GAA TGG AAT

AAA GCA TT-3'), was used for each array. As a negative control, a non-complementary oligonucleotide (5'-GAC ACT TTA TAT CAT AGG TAA ACG GAT CTT CGC TCG AAT AAT TCG TCT CTA TTC TTG CTT TTT TCG AAG TGG TGG ATG CT-5') was used. The slide was washed with 1 × PBS buffer and 0.1% SDS before 18 μL of AuNP probe solution was loaded for 60 min at 30°C. The slide was then washed by dipping it into the buffer solution containing 1 × PBS and 0.1% SDS three times, with 1 × PBS and 0.01% SDS once, and lastly with 1 × PBS before drying with gently blowing N_2 gas. Finally, the AuNPs immobilized on the microarray slide were immersed in the CuPN enhancement solution. Though it was not used here for standard condition, a small quantity of Mg^{2+} up to 1 mM can further stabilize the DNA hybridization as an optional additive.[43]

AuNP probe preparation for the norovirus assay

First, 100 μL of 1 mg/mL amine- and thiol-modified PEG (M.W. 5k) in deionized water (DIW) was mixed with 100 μL of 1% (w/v) SDS dissolved in DIW. Next, 1 mL of 60 pM citrated-AuNP (50 nm) solution was added, followed by incubation for 3 h. After centrifugation at 6,000 rpm for 10 min, PEG-modified AuNPs were redispersed in 500 μL of 50 mM MES [2-(N-morpholino)ethanesulfonic acid] buffer (pH 4.8). AuNP was mixed with 100 μL of 1 mg/mL of EDC and sulfo-NHS (N-hydroxysuccinimide) for 5 min followed by centrifugation at 6,500 rpm for

15 min. Activated AuNPs were redispersed in 250 μL of 10 mM PBS buffer (pH 7.2). Anti-norovirus antibody (4 μL, 500 μg/mL; Abcam #ab92976, Cambridge, UK) was directly added to the activated AuNP solution and incubated for 4 h. Centrifugation at 6,500 rpm for 10 min was repeated twice and antibody-modified AuNPs were finally redispersed in 250 μL of 0.05% PBST (Tween-20).

Norovirus assay procedure

A silicon isolator that can contain ~10 μL of solution was attached to the aldehyde glass. The norovirus-positive fecal sample was mixed with 10 mM Tris buffer (pH 9.0) (1:1 ratio). The mixture (1 μL) was spotted on the center of each aldehyde chamber and dried for 2 h in ambient conditions. Then, 25 μL of 1% BSA (in 10 mM PBS buffer) was added to each well. After incubation for 30 min, 8 μL of 200 pM Au nanoprobe was added to each well and maintained for 1 h. The glass was put in a Petri dish with wet tissue to prevent evaporation. Finally, the Au nanoprobe was removed and the glass was rinsed with DIW. The glass was washed with 0.05% PBST between steps.

PEI-mediated CuPN enhancement

Typically, 5 mL of 0.1 M $CuCl_2$, 5 mL of 1% PEI, and 25 mL of 0.5

M sodium L-ascorbate were mixed in a 50-mL conical tube. The as-prepared assay glass was dipped into the precursor-containing conical tube for 10 min and washed with DIW (18.2 MΩ) copiously. In this process, it was confirmed that the shape or volume of the container did not significantly affect it, though, the above conditions were used insisted on for reproducibility.

The chemical potential of Cu in solution is stabilized by Cu-PEI complex formation and the thermodynamic driving force of the reduction of free Cu ions is governed by the **Equation 2.1** and **Equation 2.2** as below:

$$E = \left(\varepsilon^{0}_{Cu^{2+}/Cu} - \varepsilon^{0}_{AA_o/AA_R}\right) - \frac{RT}{nF}\log\frac{[H^+]^2[AA_O]}{[Cu^{2+}][AA_R]} \quad \textbf{(2.1)}$$

$$K_f = \frac{[Cu - PEI]}{[Cu^{2+}][PEI]} \quad \textbf{(2.2)}$$

where AA_O and AA_R represents dehydroascorbic acid and ascorbic acid. Instead of CuPN, a small amount of hexadecylamine (HDA) additive (2 mM) turns the final structure into Cu nanowires (CuNWs). All other conditions for heteroepitaxial CuNW growth are identical to the CuPN formation condition, except that the CuNW growth solution needs to be heated up to 60 C to fully dissolve the hydrophobic HDA.

Photographic image acquisition

The enhanced results were photographed using a smartphone (Galaxy Note Edge, Samsung Electronics) CMOS camera under ambient conditions. Each sample was placed on a black background with a constant fluorescent lamp 15 cm above vertically. The photographic images (16.0 M pixels) with 400 ISO were obtained by the built-in application, and they were cropped and analyzed using Image-J software. The pixels inside of each spot were quantified relative to the background in the chamber area and normalized.

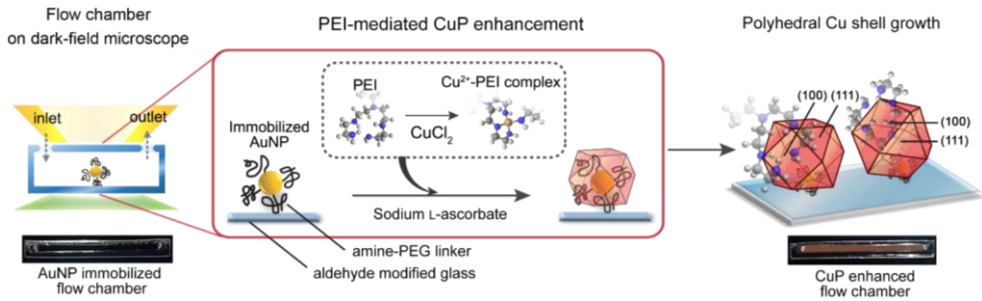

Figure 2.3. Schematic representation of the chemistry and procedures for Cu polyhedral nanoshell (CuPN) formation on Au nanoparticles (AuNPs). Polyethyleneimine (PEI)-mediated precursor chemical potential control forms the CuPN specifically on AuNPs on a glass slide. The growth has been demonstrated in a flow chamber under DF microscope by injecting the CuPN enhancement solution into the inlet of the chamber. The visible-light images before (lower left) and after (lower right) CuPN formation on AuNPs in a flow chamber on a glass chip.

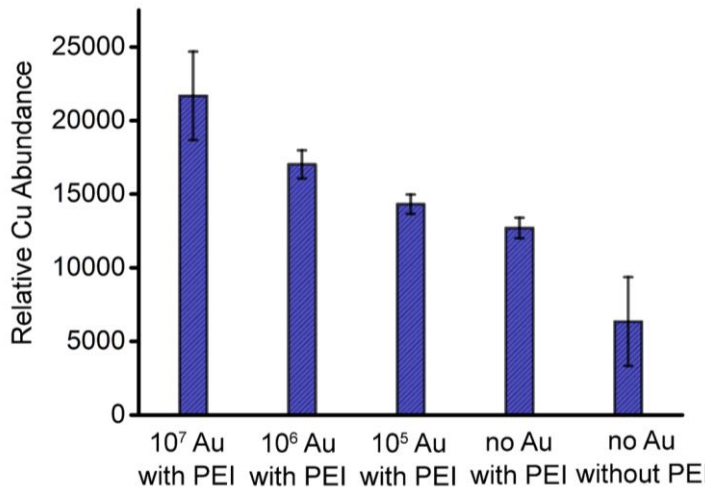

Figure 2.4. The Cu abundance on substrates with different numbers of immobilized 50 nm AuNPs was analyzed using time-of-flight secondary ion mass spectroscopy (ToF-SIMS). The AuNP-immobilized substrates were immersed for 10 min under the enhancement solution without reducing agent. The ToF-SIMS was conducted using a single Bi1 30 keV LMIG source operating in pulsed and continuous modes for analysis. Cu ions were detected using positive mode ion detection at 100 μs of cycle time.

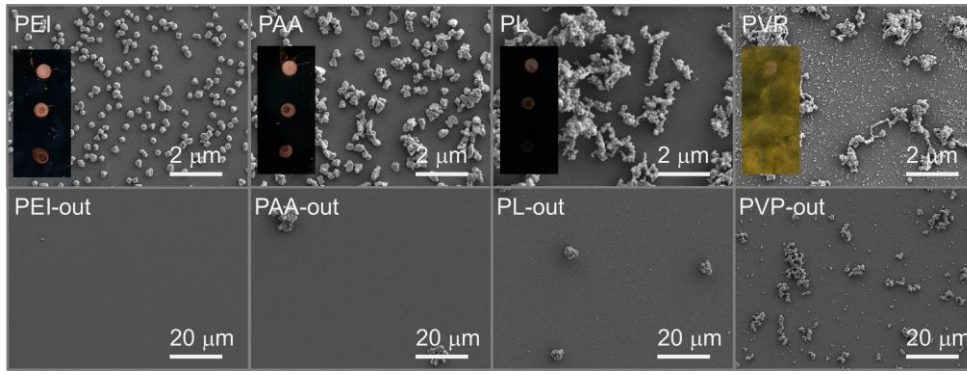

Figure 2.5. Polymer-mediated Cu nanoshell overgrowth with by various polymers. From the standard Cu enhancement solution, PEI was replaced with polyacrylic acid (PAA), poly-L-lysine (PL) or polyvinylpyrrolidone (PVP) with the same monomeric concentration. Each substrate was spotted three times with different numbers of the immobilized AuNPs (10^7, 10^6, 10^5 from top to bottom in the inset images) and was immersed in solution for 10 min. SEM images in the top row were from 10^7 AuNP-immobilized spots and the images in the bottom row were from non-spotted areas.

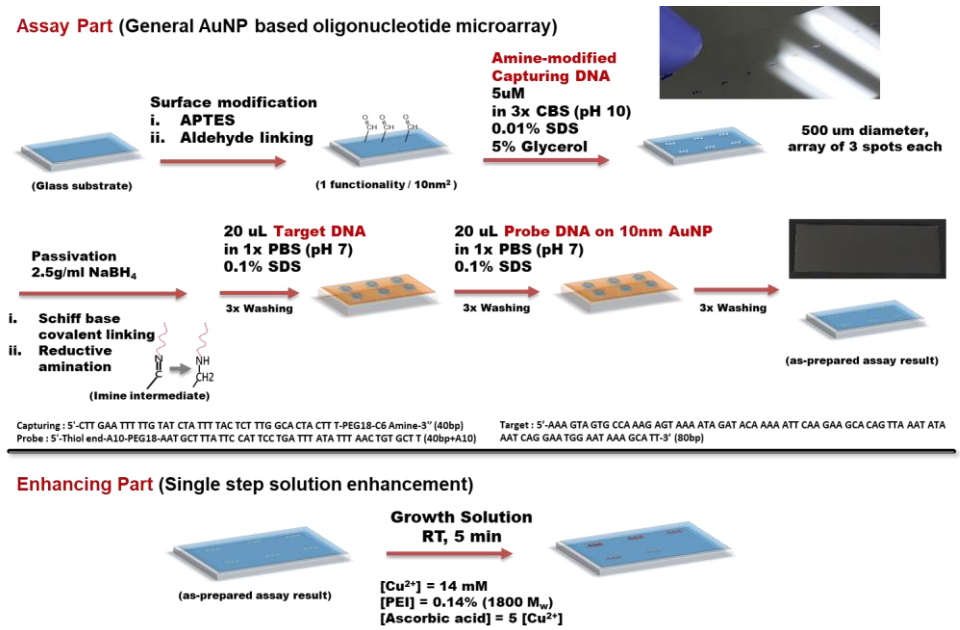

Figure 2.6. Summarized illustration of overall procedure of the naked-eye DNA assay with CuPN-enhancement on microarray chip.

2.3. Results and Discussion

First, we investigated physical and optical characteristics of PEI-mediated Cu shell overgrowths on immobilized AuNPs in situ monitoring under a dark-field (DF) microscope with a glass flow chamber. 1-D flow cell was set up by sealing with a thermo-spacer between an aldehyde-modified glass and a cover glass with two holes (inlet and outlet holes) to observe the Cu shell formation in situ. The 50 nm AuNPs modified with amine-functionalized polyethylene glycol (PEG) linkers were initially added into the flow cell and covalently linked on the aldehyde glass through imine intermediates. After 10 min incubation, unbound AuNPs in the cell were washed out with deionized (DI) water (18.2 MΩ). The initial positions of AuNPs have been identified under the DF microscope, and then we injected the CuPN enhancement solution as described above.

Plasmonic metal NPs exhibit strong size-dependent scattering property, thus, DF microscopy is an appropriate analytical tool for monitoring the real-time growth and its kinetics of the metallic nanoparticles and their scattering properties (**Figure 2.7**).[44] The voltage on a tungsten–halogen lamp was initially set at 12 V for observing AuNPs on glass substrates, and was lowered down to 4 V for the observation of CuPN growths in order to prevent saturation on charge coupled device camera (the exposure was 100 ms for all the cases). After injecting the CuPN enhancement solution, Cu nanoshells started to form on AuNP surfaces, evidenced by a dramatic

increase in red light scattering. The average scattering signal amplification under DF observation showed ≈93-fold increment as the CuPNs were formed on AuNPs. The scattering intensity of each spot increased monotonically over time up to ≈300 s. Additionally, the Cu product showed uniform red color and intensity; accordingly, we could confirm the homogeneous CuPN growth process. Of note, bright spots at the final stage were well matched with the sites on the initial AuNPs, indicating highly specific one-to-one CuPN growth on AuNPs.

The strong and quantitative visual signals with negligible background noise of this enhancement method can be attributed to the highly specific overgrowth of CuPNs and uniformly controlled individual Cu nanostructures. As the scattering intensity increased over time in the DF analysis, the Cu shells were gradually developed into >100 nm-sized polyhedral as shown in the scanning electron microscopy (SEM) images (**Figure 2.8**). The final Cu shell structures were mainly single-crystalline cuboctahedra (66%) and a few of anisotropic rods (18%) with five-fold twins, as commonly found in anisotropic FCC-structured nanomaterials.[41] Varying capping agents ranging from PEG to DNA and antibody did not noticeably affect final CuPN structures (**Figure 2.9**). On the other hand, a small amount of additive HDA (2 mM) allows Cu to grow into nanowires (**Figure 2.10 and Figure 2.11**). The different resulting structure can be explained by higher surface affinity of HDA than that of the competitive PEI. Linearly shaped hydrophobic HDA binds to the (100) faces on the side of

nanowires, driving nanowires to grow along the <111> direction.

The enlarged polyhedral Cu nanostructures generate stronger light-matter interactions and much larger Mie scattering-dominant extinction cross-sections than AuNPs as 3-D finite-element method-based electromagnetic field simulation results show (**Figure 2.12**; see details in **Figures 2.13 and Figure 2.14**). Through the X-ray diffraction pattern analysis (**Figure 2.15**), we confirmed Cu oxide was not observed for months after formation of Cu nanoshells. Polyhedral structural features such as corners and edges are largely responsible for the field enhancement. The particle locations and signal origins were perfectly correlated on SEM and DF images (**Figure 2.16**). Single-crystalline Cu cuboctahedral structures are relatively uniform in size (542 ± 78 nm). In comparison, commercially available hydroquinone-induced Ag nanoshells show large variations in size (228 ± 98 nm) owing to their poorly defined structures (**Figures 2.17**, upper). The homogeneity of individual CuPN structures results in their narrow scattering signal bandwidth and strong intensity (**Figure 2.17**, lower). Compared to the poorly controlled Ag growth, CuNWs showed better structural and scattering signal enhancement as well for various Au seed sizes (**Figure 2.18**) and surface densities (**Figure 2.19**). The resulting Cu nanostructures showed stronger light scattering intensities in optical microscopic images with lower background signals (**Figure 2.20)** and these results are in good agreement with their nanostructures found on SEM images (**Figure 2.21**). Moreover, no randomly grown Cu structures were

found on untreated glass substrates (**Figure 2.22**), and the growth solution maintained the stability of ionic Cu as represented by its blue color while Ag enhancement solution showed severe self-nucleation (**Figure 2.23**). This further shows the outstanding specificity and the usefulness of this chemistry, which can be reliably applied to biosensing applications.

For DNA detection, an anthrax lethal factor DNA sequence with 40 base pairs was chosen as a target.[45] The medium lethal dose (LD 50) of anthrax is likely within 2,500–55,000 spores,[46] and their DNA fragments are in the fM range.[47-49] Therefore, the straightforward on-site detection of an infectious lethal threat at these low concentrations without requiring a complex analysis on an inexpensive platform is highly important and beneficial. The assay procedures are described in detail in the Experimental Section. In a typical experiment for the DNA assay, we used a sandwich-type hybridization, starting with amine-modified target capture oligonucleotides that were microarrayed on the aldehyde glass slide (**Figure 2.24**). Next, target DNA was added to a hybridization chamber and incubated for 120 min. AuNPs with DNA, half-complementary to target DNA sequence, were then added to be immobilized by forming sandwich complexes and further incubated for 60 min (**Figure 2.25**). The hybridization chamber slide was then dipped into the sodium dodecyl sulfate (SDS) solution containing 1 × phosphate-buffered saline (PBS) buffer and dried by gently blowing N_2 gas. The glass slide was dipped into the CuPN enhancement solution for 10 min at room temperature. The slide

was finally washed by DI water and then analyzed. The invisible spots on the assay slides were developed into orange-colored visible spots containing >100 nm-sized Cu polyhedral within a few minutes, distinguishable down to 8×10^{-15} M with the naked eye, without instrumentation (**Figure 2.26**). The quantitatively analyzed signal intensity showed a wide dynamic range and apparently linear relationship, with intensity on a log-scale (**Figure 2.27**). Also, the CuPN DNA assay presents negligible nonspecific background noise, and thus higher signal intensities than the results from Ag enhancement (**Figure 2.28**, upper). At low concentrations (approximately fM target concentrations), the CuPN-enhanced signals present the lowest limit of detection ever reported for the direct visualization of oligonucleotide assay results without target amplification which was essentially required so far.[32] Moreover, CuNW enhancement results showed extraordinary efficiency especially for the low target concentrations because of their strong scattering signals from the anisotropic structure that they were individually countable even with an optical microscope (**Figure 2.29**). The detection limit of the CuPN assay for anthrax DNA target is 8×10^{-15} M, which is at least approximately two-fold better than that of the conventional Ag enhancement-based assay. It should be noted that Ag enhancement generated large background signals that are detrimental to quantifiable, reproducible detection results. A non-complementary sample as a negative control did not yield visible spots for either Cu or Ag, but still much stronger background noise was presented in the Ag case.

Next, we applied the CuPN enhancement strategy to rapid naked-eye-based detection of human noroviruses in stool samples with high quantification capability. Norovirus is the primary causal pathogen of gastroenteritis in humans. It is easily transmitted via feces-contaminated food or water, exposure to contaminated surfaces or objects, and person-to-person contact. There are, however, no vaccines to treat norovirus infection, and it is difficult to culture the human strain of norovirus in a cell culture dish.[50] Accordingly, fast, simple, and sensitive norovirus detection is needed to prevent outbreaks of infection. Reverse transcription polymerase chain reaction (RT-PCR) is the gold standard owing to its high sensitivity, but requires specialized equipment with an expert and complex procedures, beginning with RNA extraction.[51] Recently, sensitive colorimetric immunoassays have been developed with catalytically grown plasmonic nanostructures for detection of cancer biomarkers, and solution color change was used as a signal.[52-54] It was shown that formation of thin metallic shells on AuNPs can induce a wavelength shift in the Rayleigh scattering spectra, and this spectral shift was used as a detection signal.[55-57] In our study, we used a sample spotting-based direct assay platform in order to effectively detect small amount of norovirus and subsequently applied the CuPN enhancement (**Figure 2.30**). Experimentally, we spotted 1 μL of norovirus-positive stool samples in each of the chamber wells and immobilized the norovirus on the aldehyde-modified glass substrate. Then 50 nm antibody-modified AuNP probes and the CuPN enhancement solution were

subsequently applied to the chamber wells. The major product was also the Cu polyhedron shell formed on the antibody-capped Au nanoprobes. The CuPN assay results successfully visualized low quantities of invisible AuNP probes, which allows detecting low levels of noroviruses in clinical stool samples and environmental samples in naked eyes and without target amplification or enzymatic signal amplification (**Figure 2.31**). The intensity showed a linear relationship along approximately two orders of magnitude of target quantity (**Figure 2.32**). The limit of detection (LOD) was approximately 2,700 noroviruses; for a larger number of nontarget viruses (2.1×10^5 copies of bacteriophage MS2), a negligible signal was observed. The LOD is superior to that of the norovirus assay result from enzymatic amplification (**Figure 2.33**) or conventional lateral flow assay kits.[25]

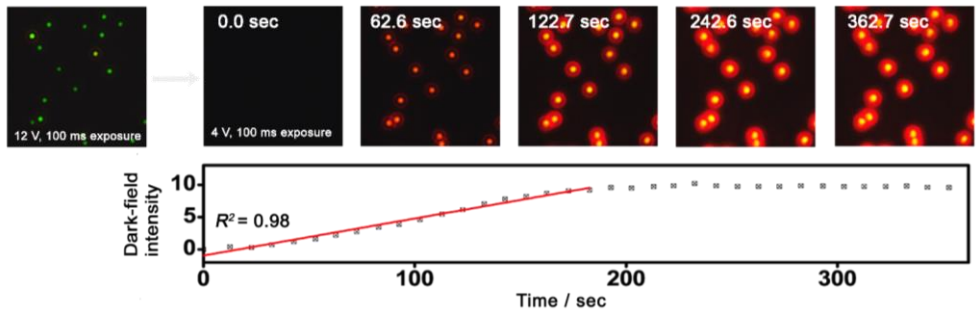

Figure 2.7. Verification of kinetics and one-to-one overgrowth of CuPNs on AuNPs on a glass chip by in situ DF microscopy. The positions of AuNPs were initially identified under 12 V light and lowered to 4 V at the beginning of the Cu enhancement to prevent scattering signal saturation. The lower graph shows the DF intensity change as the CuPN enhancement proceeds.

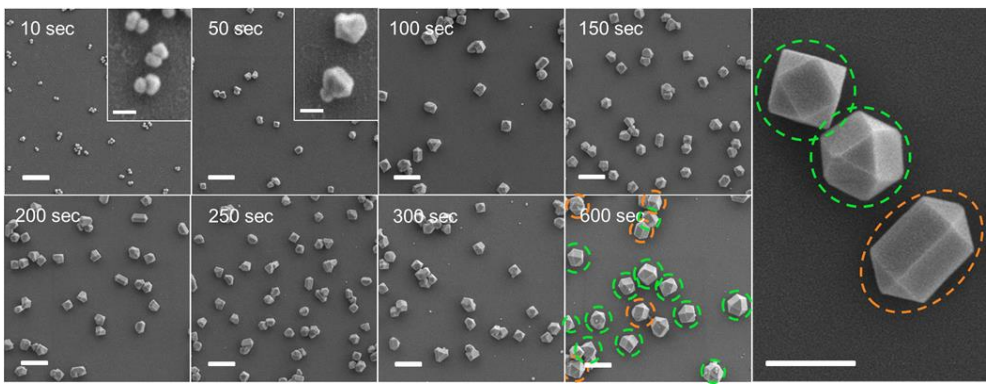

Figure 2.8. Structural analysis of the Cu nanostructures based on SEM for various growth times. Cuboctahedrons with different orientations (green circle) and fivefold rods (orange circle) are distinguished. Scale bars: 500 nm (scale bars for the inset: 100 nm).

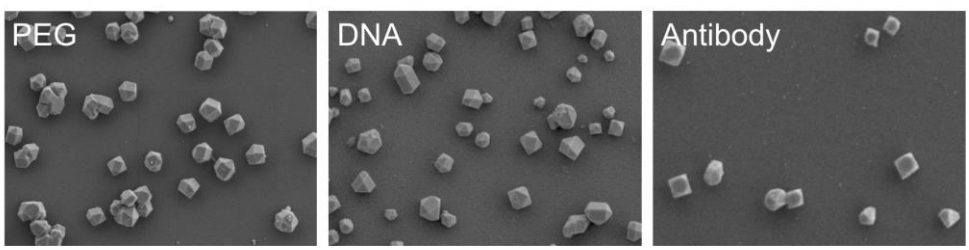

Figure 2.9. SEM images of the CuPN structures grown on AuNPs modified with three different capping agents (PEG, DNA, and antibody).

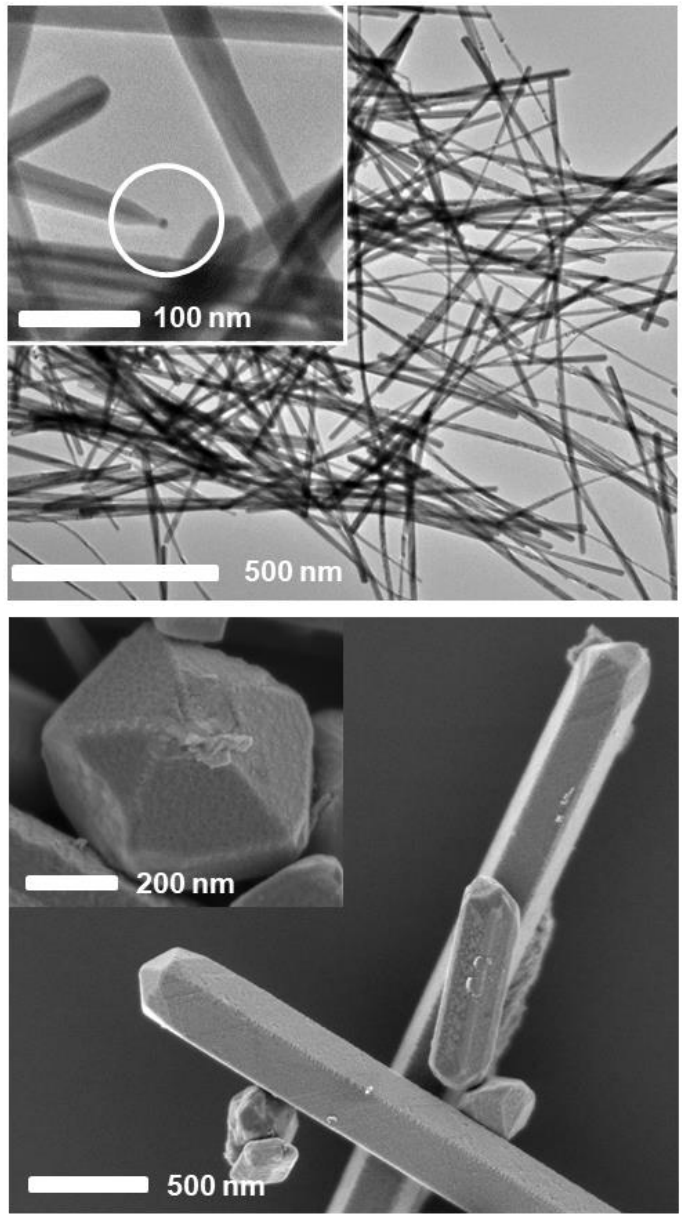

Figure 2.10. TEM (upper) and SEM (lower) images of Cu nanowires grown from Au seeds. Insets indicate Au seeds as starting points for heteroepitaxial growth.

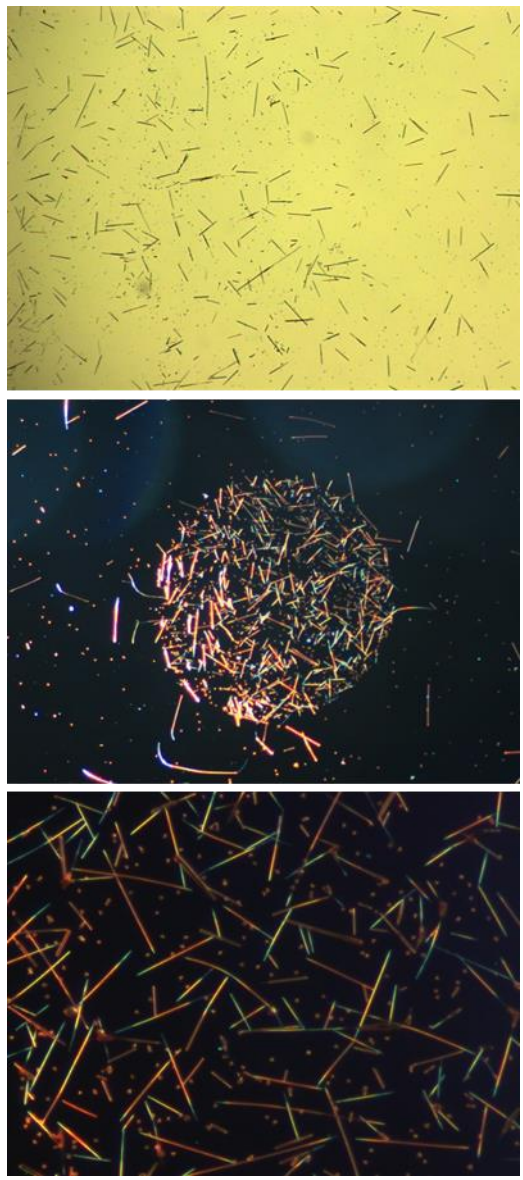

Figure 2.11. Optical microscopic images of CuNWs obtained by differential interference contrast (DIC) mode (upper, 10x) and dark-field (DF) mode (10x for middle and 40x for lower).

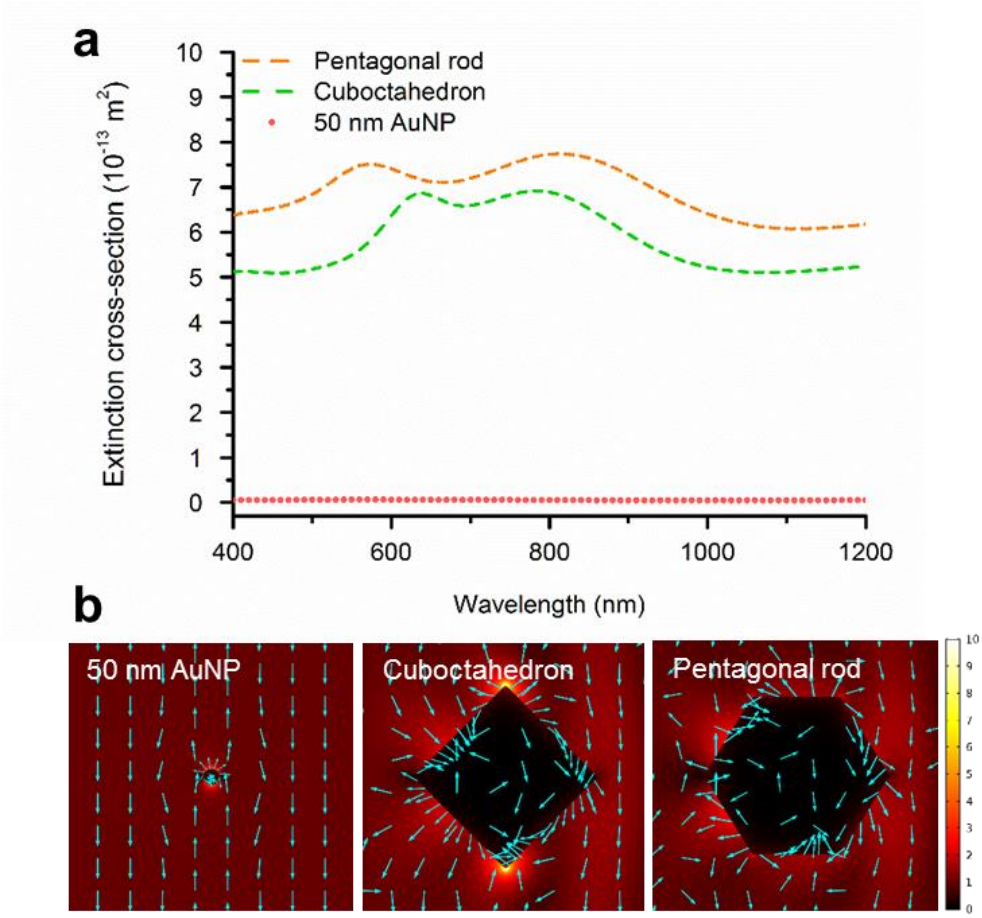

Figure 2.12. Electromagnetic field simulation results on polyhedral Cu nanoshell and AuNP structures. (a) Far-field extinctions of spherical 50 nm AuNP, Cu cuboctahedron with 400 nm in diameter and Cu pentagonal rod with its volume equal to the cuboctahedron. (b) Plasmonic near-field responses of the three different nanostructures. The arrows indicate electric field directions, and the contour represents the electric field strength, |E|.

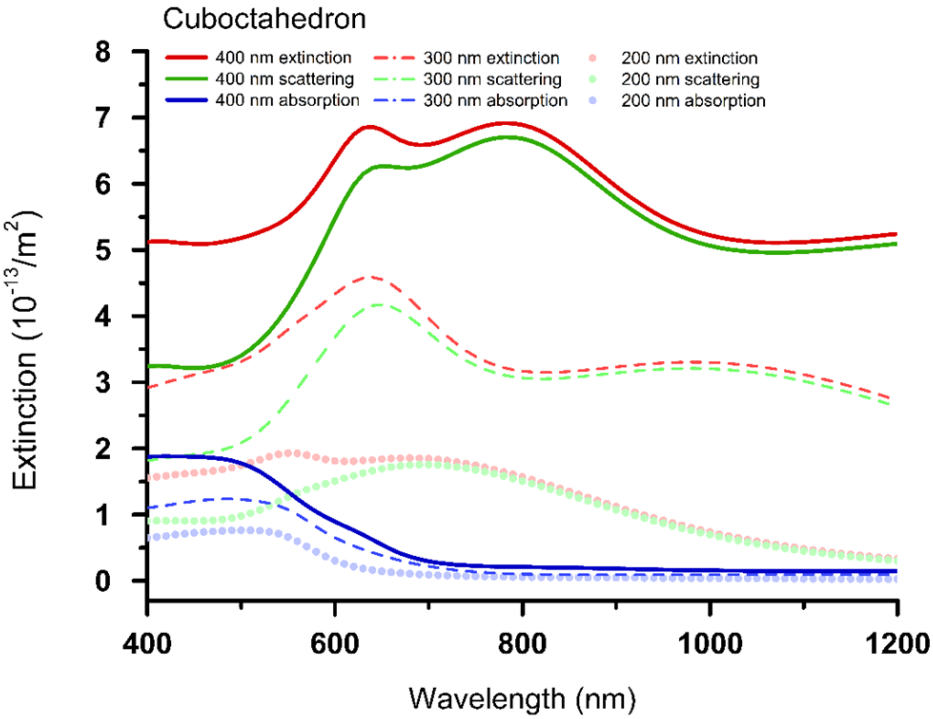

Figure 2.13. Calculated extinction cross-section of the three different sizes of Cu cuboctahedron (200 nm, 300 nm, and 400 nm in diameter). The electromagnetic far-field extinctions were calculated with 3D FEM. Scattering and absorption contributions were calculated separately.

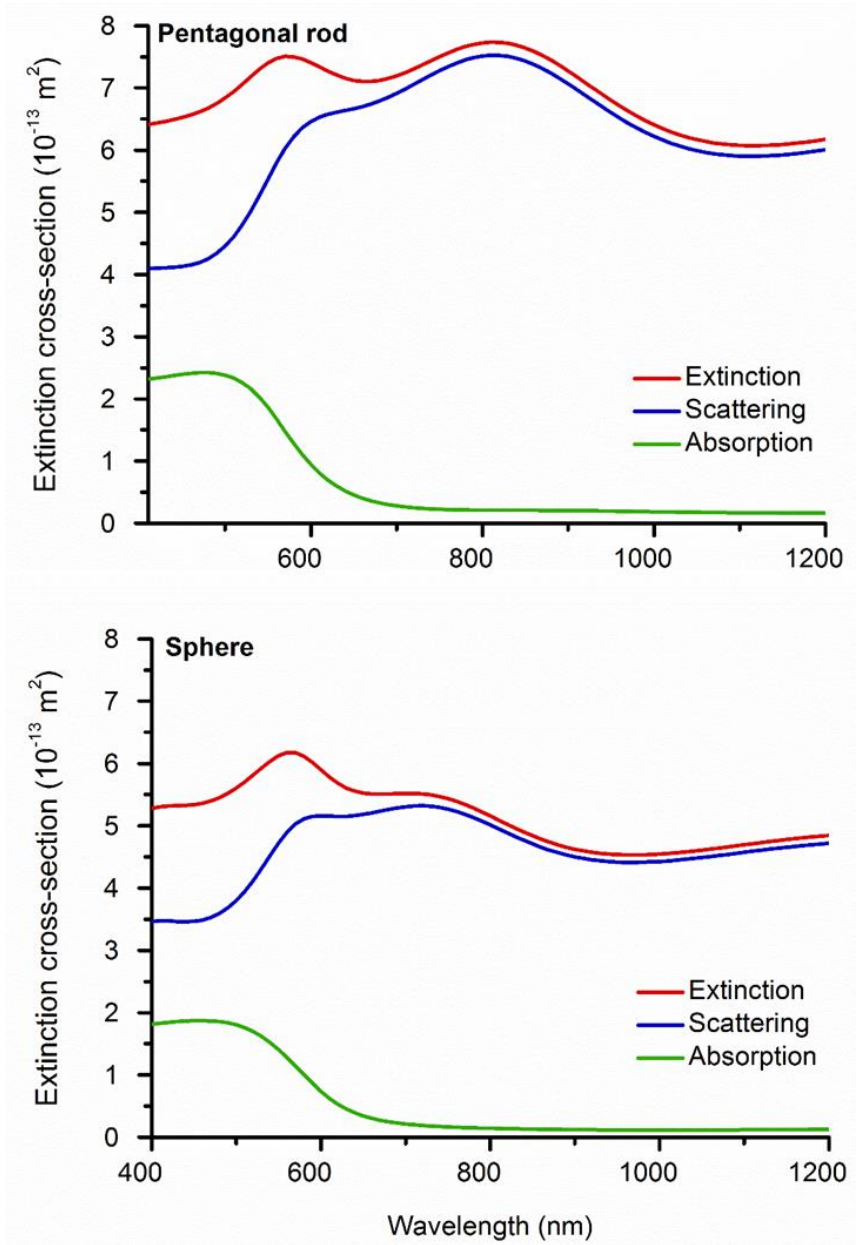

Figure 2.14. Calculated extinction cross-section of the pentagonal rod and sphere with the same particle volume to that of the cuboctahedron with 400 nm in diameter. Pentagonal rod is a minor polyhedral product and still shows stronger scattering than isotropic sphere. The electromagnetic far-field extinctions were calculated with 3D FEM. Scattering and absorption contributions were calculated separately.

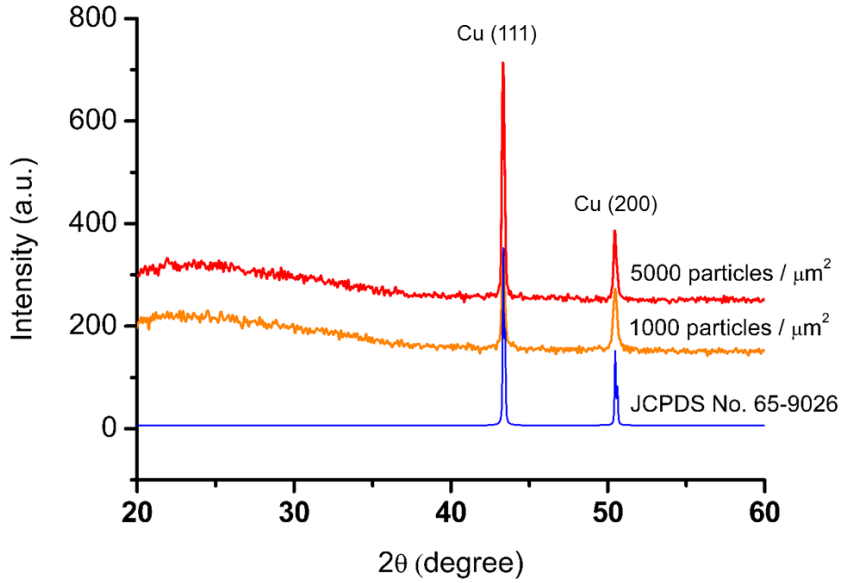

Figure 2.15. X-ray diffraction (XRD) pattern of the CuPNs with different surfaces. The amine-functionalized 13-nm AuNPs were immobilized on the substrate with two different concentrations. The particles were prepared by the same procedure as the AuNP probe preparation steps for the norovirus assay. The XRD pattern was obtained after the CuPN growth on the AuNPs. The diffraction pattern shows the CuPNs with well-crystallized face-centered cubic (fcc) structures. The CuPN formation method in this report abnormally produces large single-crystalline CuNPs with clear polyhedral structures in aqueous solution under room temperature and ambient condition within a few minutes. From the **Fig. 2.2a**, one-to-one overgrowth of CuPNs on AuNPs can be verified from the head-body structures at 10 sec. Polyhedral structures were developed from 50 sec, and the edges were sharpened. Most of the final structures were single-crystalline cuboctahedrons (66%) with multiply twinned pentagonal rods as a minor product (18%). Few other structures could be defined as triangular orthobicupola which has a superficial resemblance to the cuboctahedron and can be resulted from stacking faults with hexagonal close-packing (hcp) arrangement. Majority of the particles were well crystallized into fcc crystal structure, and the diffraction pattern of the Cu product was stable for several weeks.

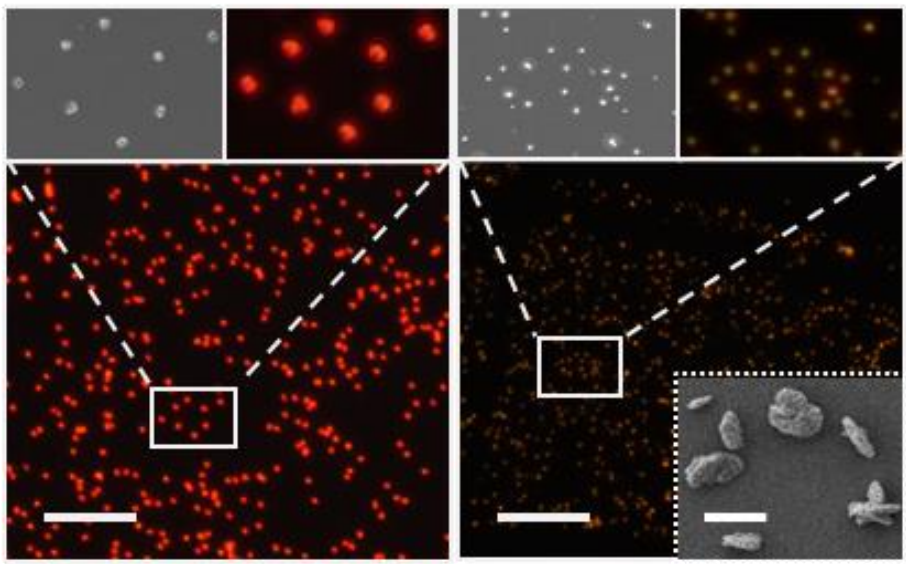

Figure 2.16. Correlation of SEM with DF microscopy. Left (right) panel shows Cu (Ag) enhancement results. The lower images show the low-magnification distributions of Cu (left) and Ag (right) shell structures in DF observation. The upper images are the SEM and corresponding DF images for each case. Scale bars: 10 μm (scale bar for the inset: 500 nm).

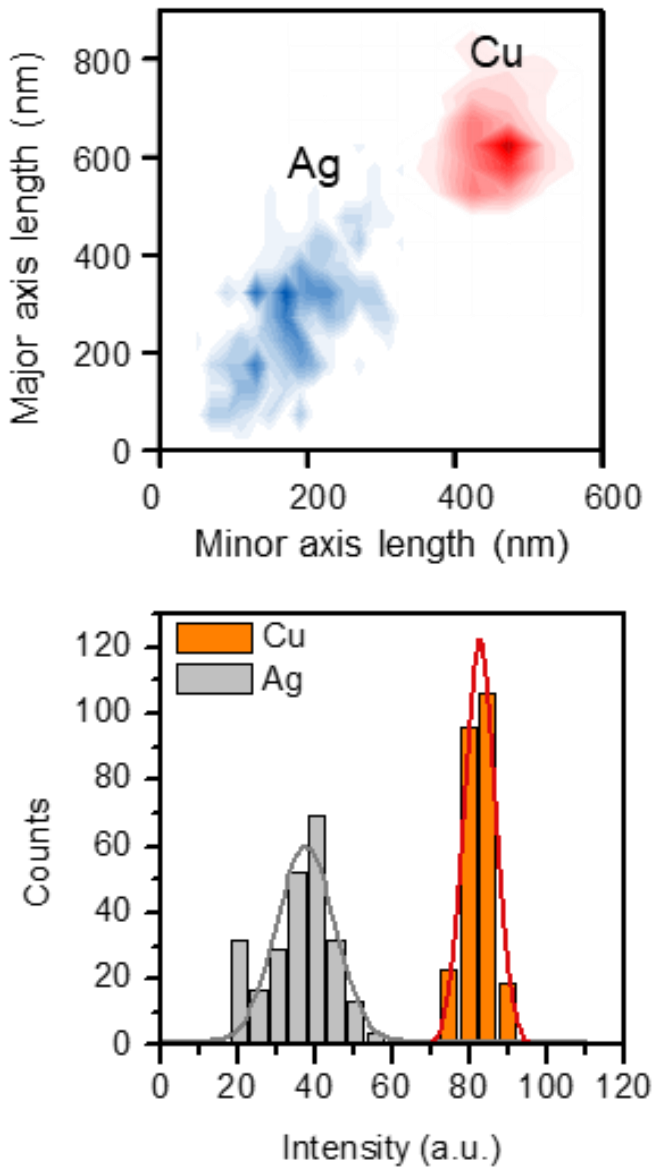

Figure 2.17. Upper: 2-D contour maps of the major and minor axis lengths of the nanostructures (n = 206) after Cu (red) and Ag (blue) enhancements, respectively. Lower: DF scattering intensity profiles of Cu (orange) and Ag (grey) enhancements.

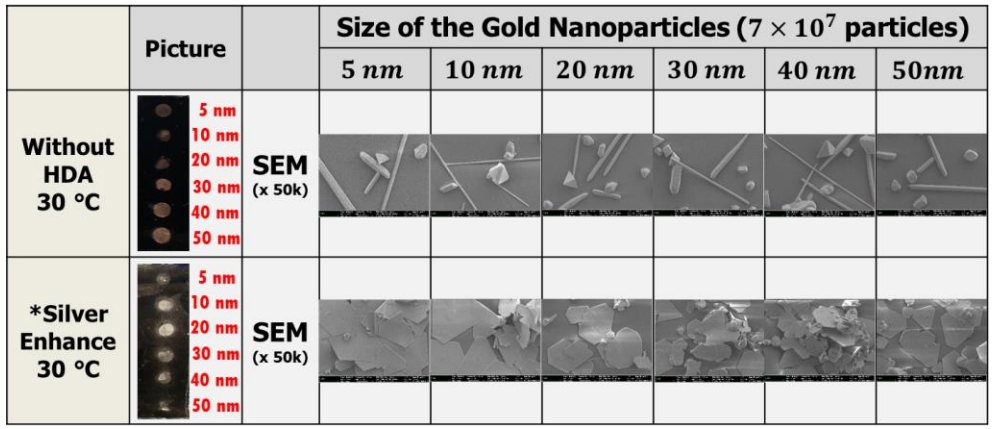

Figure 2.18. Comparison of CuNW growth results to Ag enhancement products at various Au seed nanoparticle sizes.

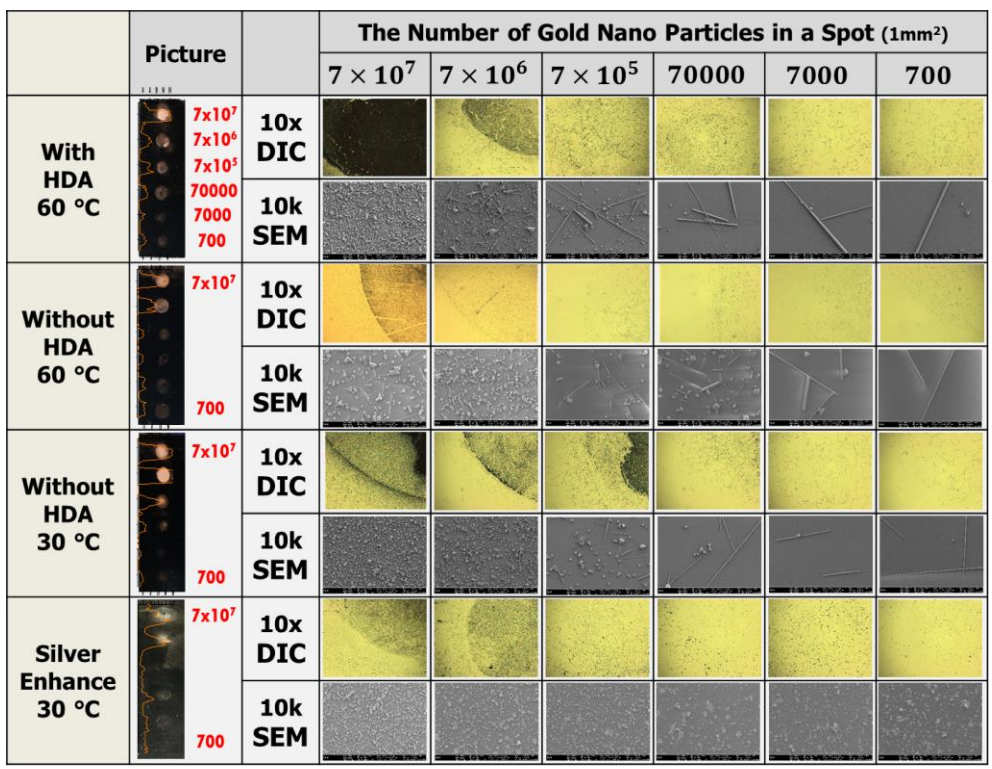

Figure 2.19. Comparison of CuPN and CuNW growth results to Ag enhancement products at various surface densities of Au seed nanoparticles.

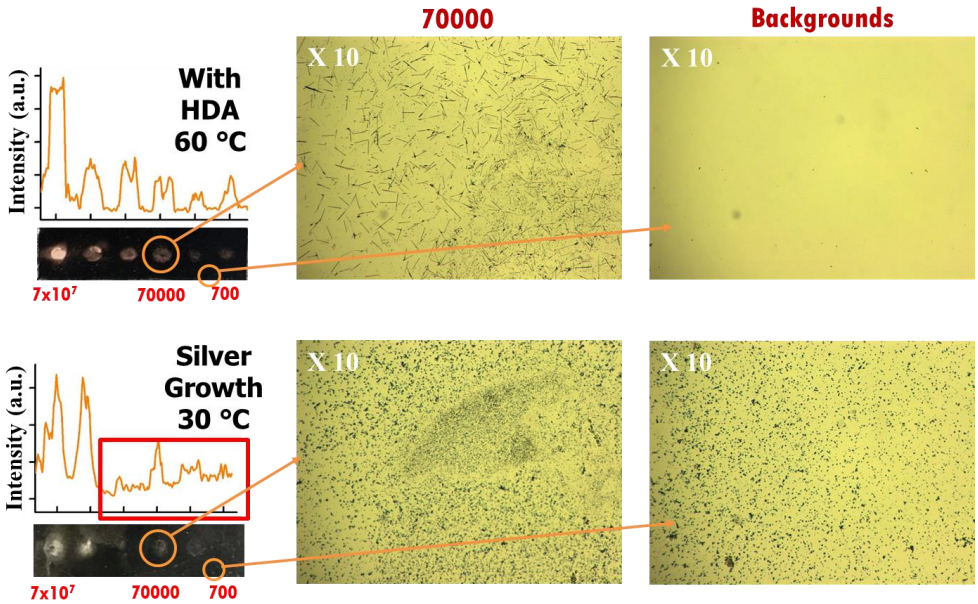

Figure 2.21. Optical DIC images of CuNW growth results and Ag enhancement products with and without Au seeds.

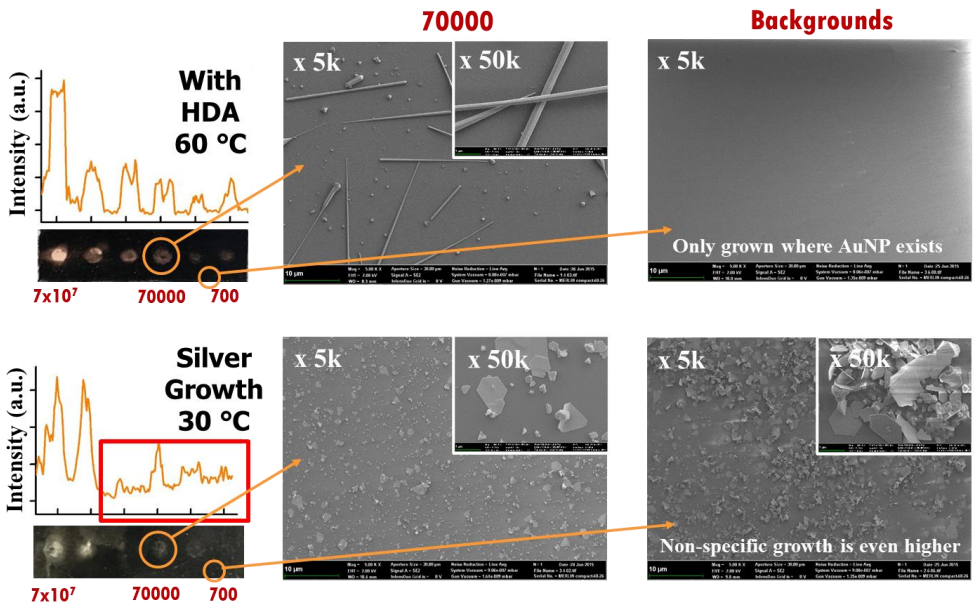

Figure 2.22. SEM images of Cu nanowire structures and Ag enhancement products with and without Au seeds.

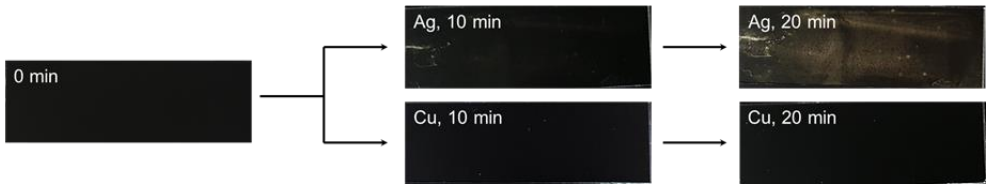

Figure 2.22. Comparing background signal enhancement by Cu nanoshell formation to a commercially available Ag enhancement. Ag and CuPN enhancement results on bare aldehyde glass chips after 0-, 10-, and 20-min staining times.

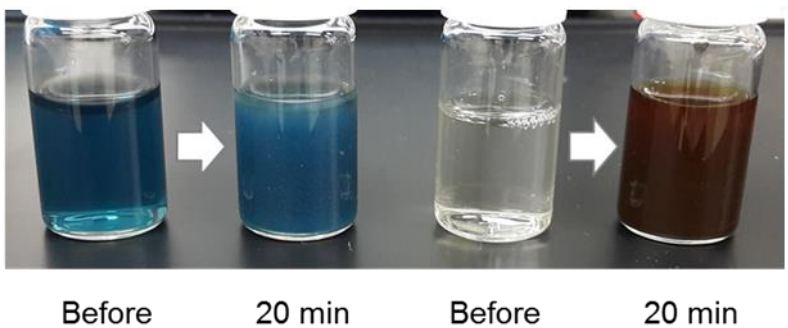

Figure 2.23. Picture of the stability and suppressed self-nucleation of Cu enhancement solution comparing with a commercial Ag enhancement solution.

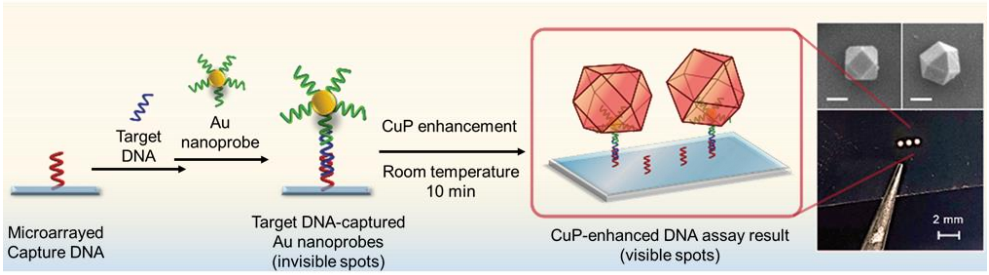

Figure 2.24. Schematic representation of CuPN growth on AuNPs in a sandwich DNA assay platform for naked-eye detection. SEM images on the upper-right and the corresponding illustration show the same cuboctahedra structure in two different orientations. Scale bars: 200 nm. The picture on the bottom-right shows a CuPN-enhanced DNA assay result on a glass substrate.

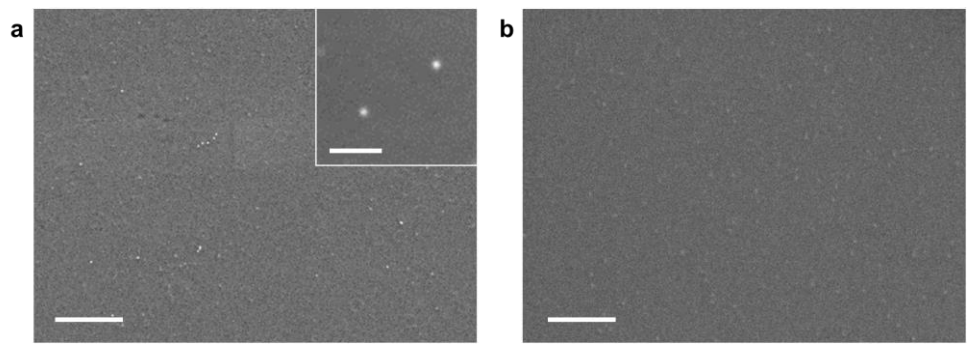

Figure 2.25. SEM images of the as-prepared anthrax lethal factor DNA assay result. (a) SEM image of the assay substrate with complementary target DNA-immobilized 13-nm AuNP probes. The target DNA (2.7×10^3 copies) were loaded on a 0.8 μm^2 spot of printed capture DNA for the sandwich hybridization assay. (b) SEM image of the DNA assay results with non-complementary target DNA. Scale bars: 500 nm (scale bar for the inset: 100 nm).

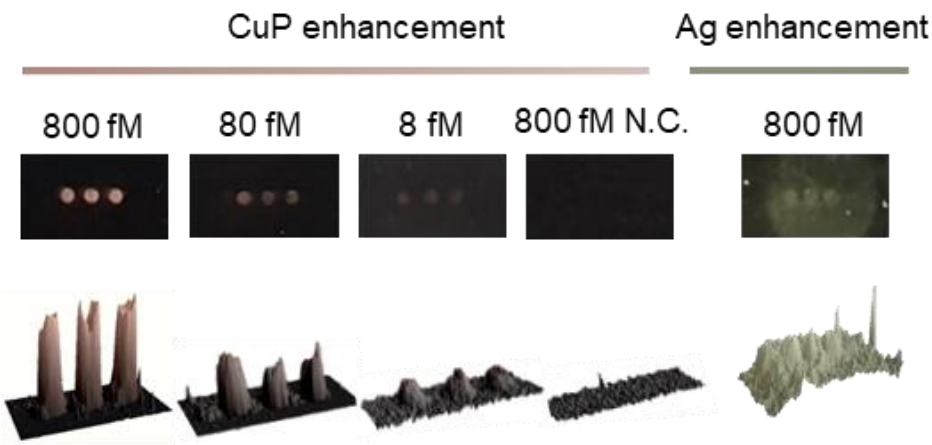

Figure 2.26. Smartphone camera pictures and the 3-D histogram plots of the Cu and Ag enhanced assay results, visible down to ~8 *f*M for CuPN assay spots while Ag spots became unclear from 800 *f*M due to the high background signals.

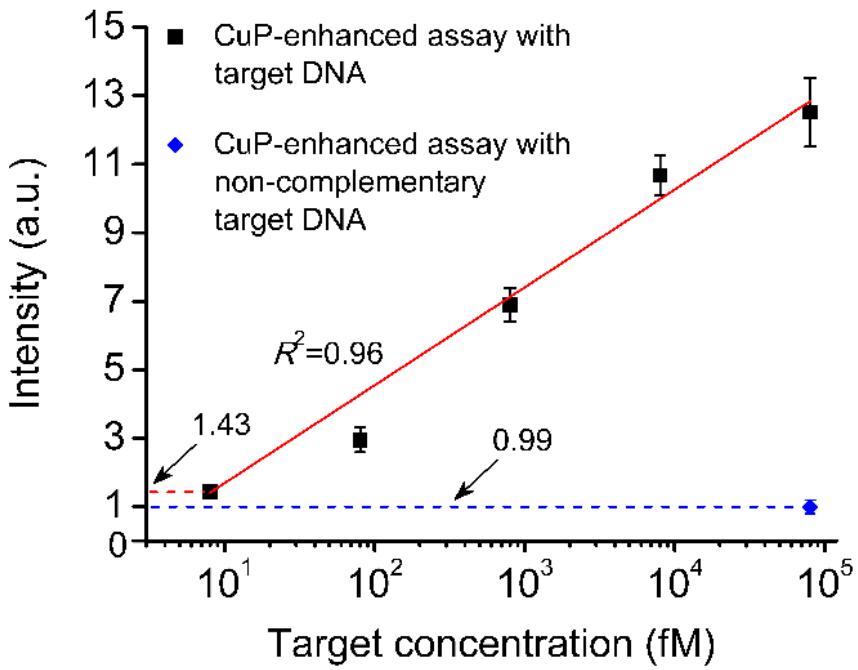

Figure 2.27. The CuPN enhancement-based naked-eye DNA detection assay. (a) Schematic representation of CuPN growth on AuNPs in a sandwich DNA assay platform. SEM images on the upper-right and the corresponding illustration show the same cuboctahedra structure in two different orientations. Scale bars: 200 nm. The picture on the bottom-right shows a CuPN-enhanced DNA assay result on a glass substrate. (b) Smartphone camera pictures and the 3-D histogram plots of the Cu and Ag enhanced assay results, visible down to ~8 *f*M for CuPN assay spots while Ag spots became unclear from 800 *f*M due to the high background signals. (c) Quantitative intensity analysis of the enhanced CuPN spots as a function of the DNA target concentration.

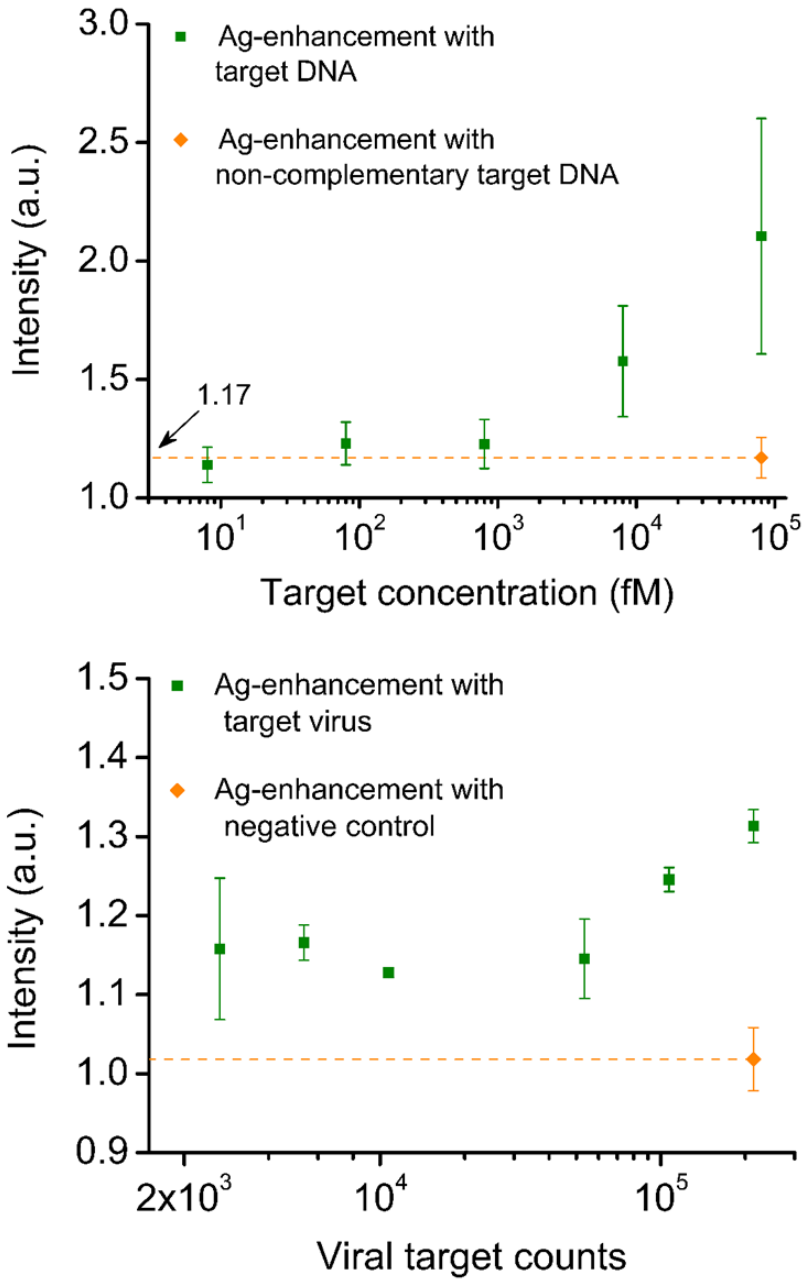

Figure 2.28. Ag-enhanced DNA and norovirus assay results. Upper: Quantitative spot signal analysis of the Ag-enhanced DNA assay results. Lower: Quantitative spot signal analysis of the Ag-enhanced norovirus assay results. Those Ag enhanced signals are faint, and the backgrounds are much higher than the CuPN assay results.

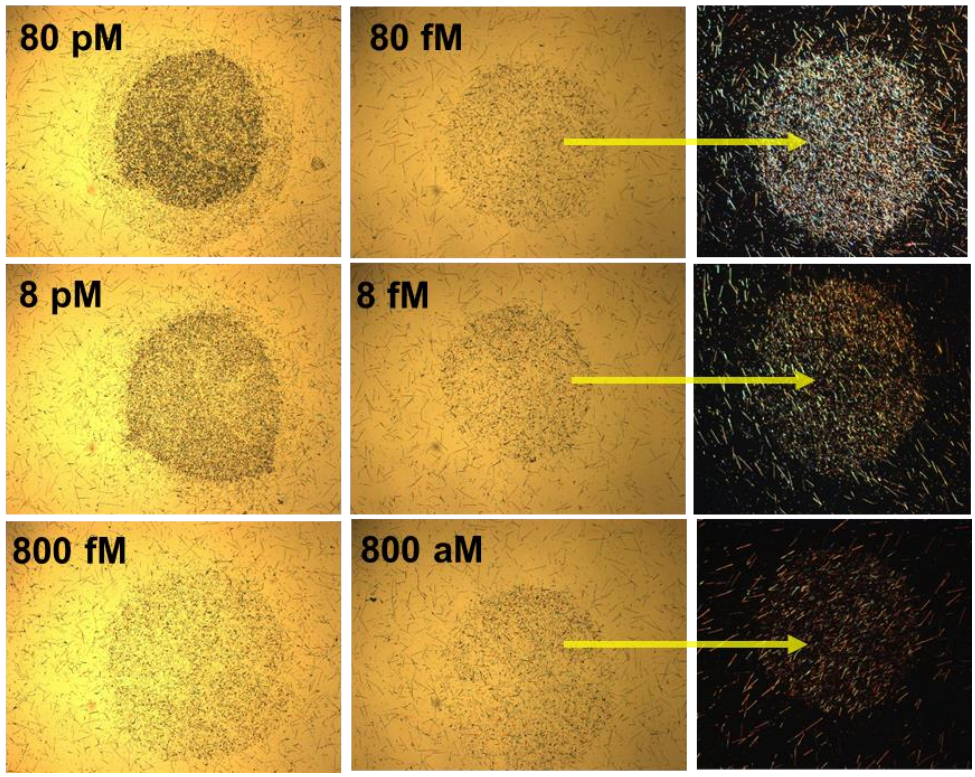

Figure 2.29. The Cu nanowire-enhanced DNA microarray spot images obtained by DIC (left and middle) and DF (right) optical microscopy for wide range (80 pM to 800 aM) of oligonucleotide target concentrations.

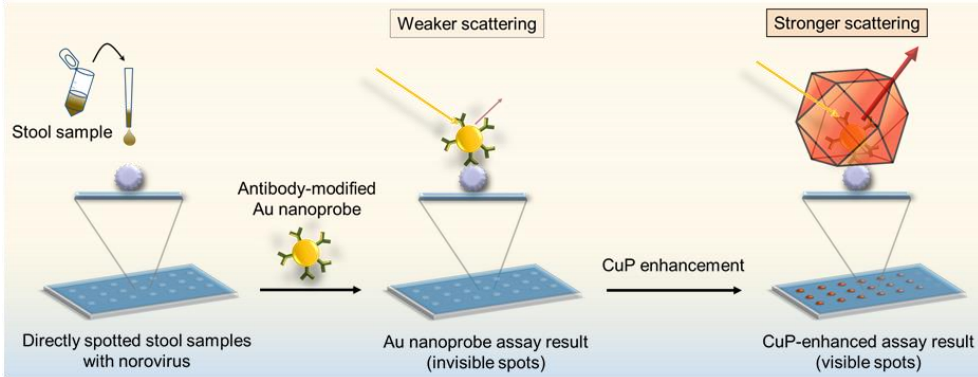

Figure 2.30. The CuPN-based human norovirus naked-eye detection assay. Schematic illustration shows the CuPN enhancement on a direct assay of norovirus. The CuPN enhancement has simply applied on an as-prepared assay result to visualize the signal by highly specific CuPN growth on AuNPs.

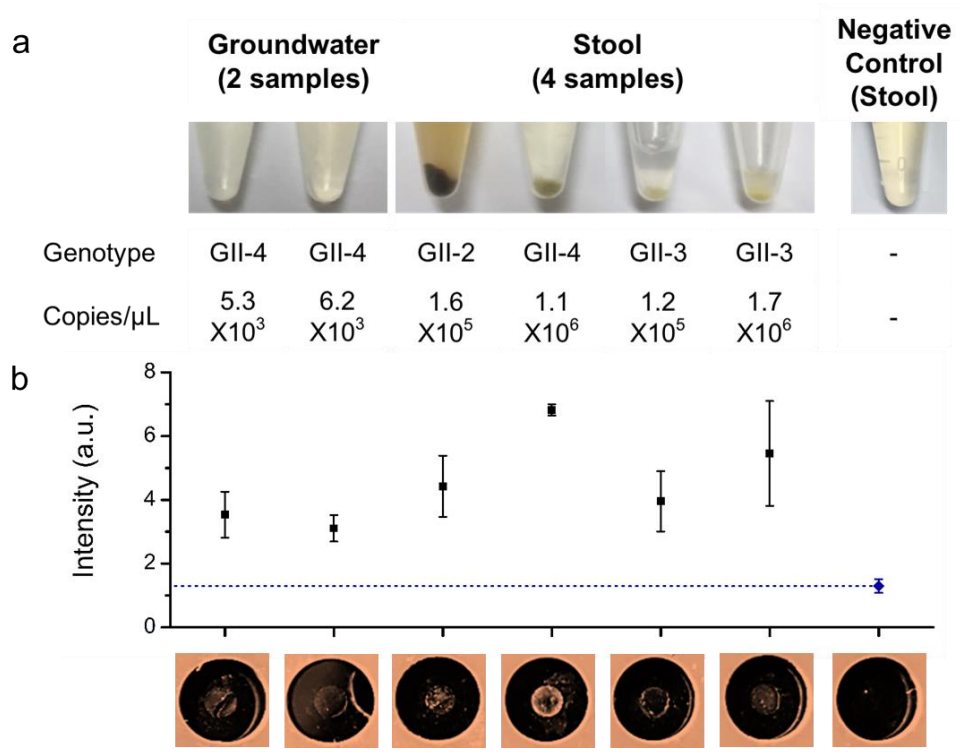

Figure 2.31. Experimental result showing CuPN-enhanced assay of noroviruses in environmental samples and clinical stool samples.

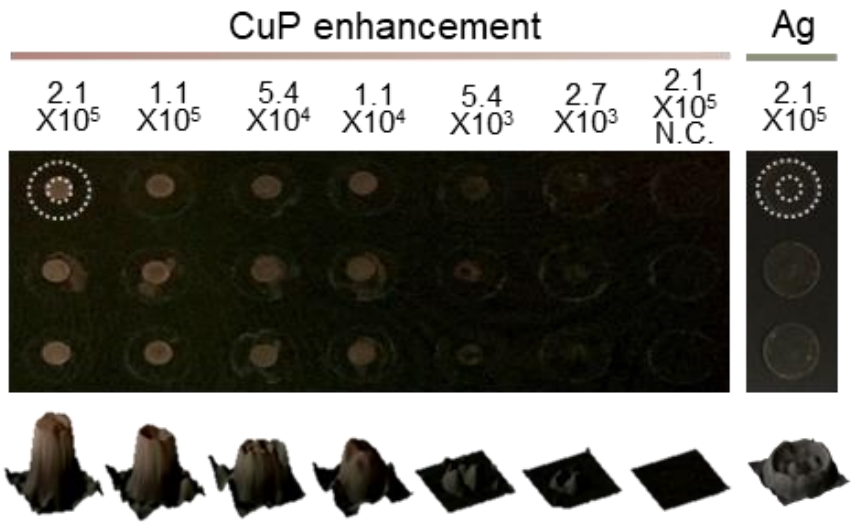

Figure 2.32. Smartphone camera pictures and 3-D plots of the CuPN enhancement results of the human norovirus assay. Outer circles correspond to the assay chamber area where the enhancement solution has applied, and inner circles correspond to the spotted area of the stool samples.

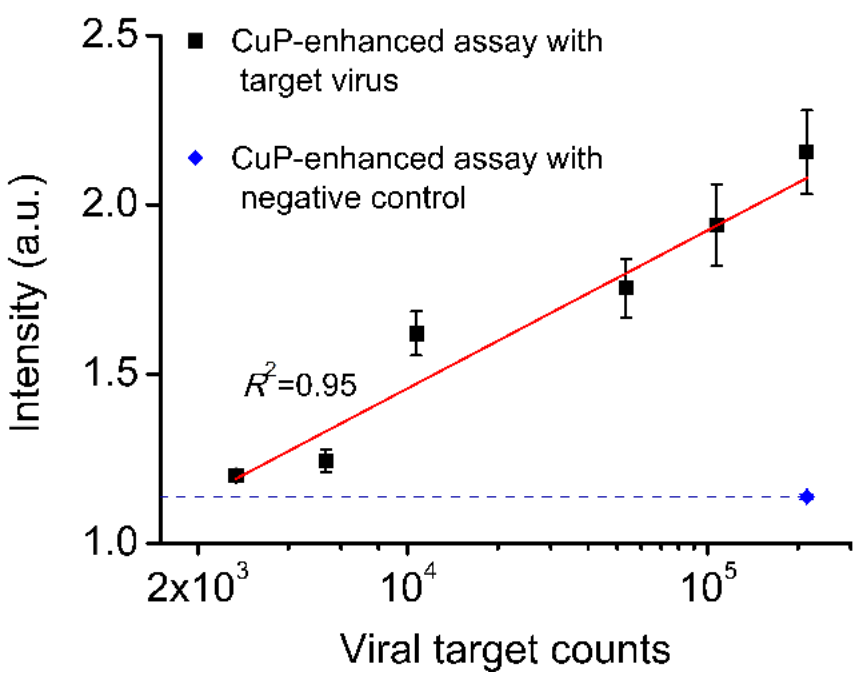

Figure 2.33. Quantitative analysis results on the CuPN-based norovirus assay (black) and commercially available norovirus ELISA (green).

2.4. Conclusion

In conclusion, we developed a highly selective and efficient PEI-mediated CuPN formation chemistry on AuNPs and signal enhancement method for the direct naked-eye visualization of AuNP probes to readily detect and quantify bio-targets of interest with high sensitivity and selectivity without a need for instrumentation and complicated experimental steps (**Figure 2.6**). This research demonstrated versatility and effectuality of the CuPN growth chemistry on universal AuNP for visible scattering signal enhancement. The highly selective one-to-one CuPN enhancements from individual AuNPs were demonstrated by in situ flow chamber-based DF microscopy and further characterized by electron microscopy. It should be noted that there is no need to further passivate aldehyde glass surfaces for obtaining strong scattering signals from the probes due to ultrahigh specificity of the PEI-mediated CuPN formation chemistry on AuNPs. Applying this method to a naked-eye-based DNA assay indicated a low detection limit of 8×10^{-15} M with a dynamic range from 8×10^{-15} M to 80×10^{-12} M without a need for complicated steps and instrumentation. Remarkably, the signals were highly reproducible and quantifiable. Further applying this method to the norovirus immunoassay showed a detection limit of 2.7×10^{3}, which is the highest reported sensitivity for nonenzymatic norovirus detection assays, with a dynamic range from 2.7×10^{3} to 2.7×10^{5} while detecting the signals with naked eyes (or more accurately quantifying

the signals with a smartphone digital camera). Our method is based on inexpensive Cu chemistry to generate polyhedral Cu shells specifically on AuNPs, it allows for highly reliable naked-eye detection, and provides high sensitivities and excellent dynamic ranges for both DNA and virus targets. Considering detection limit, dynamic range, ease-of-use, cost, time, and sample volume, our CuPN approach has clear advantages over other methods as shown in **Table 2.1**. With this method, background noise signals can be readily excluded without tedious optimization processes. This punchy light-scattering signal enhancement could save the need of intricate target amplification steps such as PCR or bio-barcode amplifications, while the simplicity is the bottom line for the applications such as rapid diagnostic tests of infectious diseases and health screenings. The polymer-mediated CuPN enhancement method developed in this work proved to be beneficial to naked-eye-based sensitive, quantitative detections of DNA, proteins, and viruses. The CuPN bioassay results open revenues for highly reliable point-of-care onsite clinical diagnostics or bioassays in research with minimal needs for complicated assay steps, laborious effort, and expensive cost of analytical methods.

Table 2.1. Representative visually detectable bioassay methods relying on metal nanoshell formation on AuNPs.

Target	Signal transduction (Naked-eye detection)	Platform	Shell material	Dynamic range	Detection limit	Sample volume [μL]	Signal-generation time [min]	Ref. No.
Anthrax DNA	Scattering intensity amplification (Yes)	Microarray[a)]	Ag	5×10^{-14}–10^{-11} [M]	5×10^{-14} [M]	20	15	[32]
DNA	Scattering intensity amplification (Yes)	Colloidal solution	Ag	10^{-14}–10^{-9} [M]	10^{-14} [M]	10	10	[58]
Norovirus	Grayscale intensity amplification (Yes)	Nitrocellulose membrane	Au	1.58×10^{5}–7.9×10^{7} [copies/mL]	9.5×10^{4} [copies/mL]	110	60	[25]
PSA[b)]	Absorption intensity amplification (Not shown)	Immunosorbent assay	Au	10^{-14}–10^{-10} [g/mL]	3.1×10^{-15} [g/mL]	100	20	[53]
PSA	Scattering intensity amplification (Yes)	Microarray	Au	3×10^{-16}–3×10^{-13} [M]	3×10^{-16} [M][c)]	50	10	[40]
PSA	LSPR spectral shift (Not shown)	Colloidal solution	Ag	10^{-18}–10^{-13} [g/mL]	10^{-18} [g/mL]	1000	180	[55]
CEA[d)]	LSPR spectral shift (Yes)	Colloidal solution	Au	0–10^{-7} [g/mL]	5.66×10^{-9} [g/mL]	-	0.5	[54]
NADH[e)]	LSPR spectral shift (No)	DF microscopy[f)]	Cu[g)]	10^{-9}–10^{-7} [M]	10^{-9} [M]	100	120	[56]
Anthrax DNA	Scattering intensity amplification (Yes)	Microarray	Cu[h)]	8×10^{-15}–8×10^{-11} [M]	8×10^{-15} [M]	20	10	Present work
Norovirus	Scattering intensity amplification (Yes)	Dot-blotting	Cu	2.7×10^{3}–2.7×10^{5} [copies]	2.7×10^{3} [copies]	1	10	Present work

[a)]Scannometric readout; [b)]PSA: prostate specific antigen; [c)]Scannometric readout and multiple depositions; [d)]CEA: carcinoembryonic antigen; [e)]NADH: nicotinamide adenine dinucleotide; [f)]With a dark-field microscope with spectrometer; [g)]Target-mediated Cu reduction; [h)]400 nm Cu polyhedra

Chapter 3

Unconventional Electrochromic Behaviors of Plasmonic Au and Au-Ag Core-Shell Nanocubes

3.1. Introduction

Localized surface plasmon resonance (LSPR) of plasmonic nanomaterials, which is tunable based on light-matter interactions, is useful for developing various photonic and optoelectronic devices.[59] In order to tune and maximize the plasmonic characteristics of metal nanostructures, researchers have mostly focused on controlling the geometries, compositions, and dielectric environments of plasmonic nanostructures. On the other hand, the electrochromic effect, which is based on the color change of a substance under the applied electrical potential or current, has also been validated as a means of manipulating the properties of plasmonic nanomaterials. A unique electrochemical plasmon resonance shift was first reported in 1991 with Ag nanoparticles.[60] Along with other chemical reactions and changes in the refractive index of the surrounding medium, it was suggested that this phenomenon is attributable to the change in the electronic properties of Ag nanoparticles. Years later, Mulvaney and co-workers further investigated Ag nanoparticles with *in situ* spectro-electrochemistry and showed a change in the surface charge density of individual colloids and the plasmon absorption band shift by a few nanometers within a limited voltage range.[61] Such a subtle optical response from the nanoparticle surface inspired researchers to develop a new analytic tool: surface plasmon spectroscopy.[62-69] This tool enabled imaging and tracking of small changes in the surface morphologies or chemical reactions

occurring on the plasmonic metal surface at nanoscale resolution. Thus, individual noble-metal nanoparticles become a colored nanoelectrode, which provides a clue for designing highly sensitive sensors or outperforming catalysts.

Plasmonic electrochromism has also attracted much interest in the development of functional optoelectronic devices, including adaptive displays or energy-efficient smart windows.[70] Yet, most of the dramatic performances from the electrochromic plasmonic materials are limited to semiconducting nanocrystals with their LSPRs positioned outside of the visible region, unlike metals.[7,70] In addition, several groups have demonstrated controlled electrochromic responses on the basis of the electrochemically active functional molecules on a plasmonic surface, but their dynamic performance has heavily relied on the functionalities of the additional electroactive layers, rather than the plasmonic material itself.[18,64,71-73] The LSPR shifts of plasmonic nanoparticles have been solely attributed to the non-Faradaic free electron density change, according to the classical understandings based on the Drude model and Mie theory.[1] Many single-particle spectroscopic studies have scrutinized minuscule plasmonic scattering spectral shifts via the capacitive charging of gold nanoparticles,[67,74-77] and their electrical manipulation was not efficient because of the intrinsically high number of free carriers of the metals and some of the features arising from damping and dielectric environments could not be explained solely by the classical models.[74,76,78]

Some of the recent results on Plasmonics are now taking quantum mechanical understandings into consideration to explain the nonuniform electron distributions and electron dynamics in the capacitively charged metal nanoparticles.[79,80] Still, the consensus is that electrochromism of the charged plasmonic metal nanoparticles is explained by the geometrical capacitance under the classical point of view that the charging effect is not dependent on the type of charged material but on the geometrical shape of the electrode. However, materials with a two-dimensional (2-D) electron gas such as graphene showed a significant contribution of the quantum capacitance serially to the total capacitance, in addition to the geometrical capacitance, because of the dramatic variation in the number of allowed electronic states by potential elevation. The quantum capacitance is the intrinsic property of a substance that is proportionally related to the electronic structure and density of states (DOS) of the material (**Table 3.1**). Heavily charged metals also have substantial change in DOS, so it might be necessary to consider that the capacitance and physical properties, such as the permittivity of metal, which largely affects plasmonic property, are indeed not constant unlike classical predictions. Therefore, to achieve higher coloration efficiency in the visible range, better durability, faster response, higher structural degree of freedom, and clear color variability, the electrical stimulus-driven intrinsic property changes in individual plasmonic metal nanocrystals, based on the underlying quantum mechanical features and their dependence on electrical stimulus, should be fully explored.

Herein, we report unconventional electrochromic behaviors of capacitively charged plasmonic metal nanocubes. It was possible to verify the hypothesis on the anomalous phenomenon in a way of preparing nanocubes with different surface elements and comparing their electrically tuned scattering properties (**Figure 3.1**). Our findings on rapidly and highly charged gold nanocubes (AuNCs) reveal more active electrochromic behavior beyond the conventional capacitive charging effect (**Figure 3.2**), and electrochemical analysis indicates the noticeably varying capacitance of AuNCs. Particularly, AuNCs show a faster scattering frequency shift in the highly negative potential range, while maintaining their structural stability, and this opens the possibility of largely tunable electrochromic LSPR shifts, which is a major limitation in electrochromism. This led us to further explore Ag−Au core−shell nanocubes (Au@AgNCs), and the surface material dependency of plasmon resonance under electrical potential was investigated to verify a need for the scope beyond the classical understandings of capacitive charging for discovering relevancy of the change to the DOS of the metals. Individual nanoparticles were placed on one of the two transparent conducting oxide electrodes facing each other, placed in an electrolyte, and observed under dark-field microscopy (**Figure 3.3**). We simultaneously acquired their plasmonic scattering spectra under an externally applied electric potential. Remarkably, their ensemble scattering spectra showed moderate shifts in resonance frequencies at low voltages and dramatic plasmonic scattering changes above the threshold

voltages, because of external and internal electrochemical effects. We found that this unexpected change beyond the classical understanding can be attributed to the material-specific quantum mechanical electronic structures of the plasmonic materials.

Table 3.1. Comparative features of geometrical capacitance and quantum capacitance

Geometrical capacitance	**Quantum capacitance**
$C_g \equiv \frac{dQ}{dV} = \varepsilon_m \frac{A}{d}$	$C_q = Se^2 \frac{dn}{d\mu}$ $\frac{dn}{d\mu}$; *density of state*
Classical point of view	Quantum mechanical property
Independent to the electrode material	Depends on the DOS of charged material
Geometrical shape matters	Significant in low dimensional materials (nano-electrode, nanosheets, and nanoparticles)
Includes electrochemical double layer capacitance	Serially related to geometrical capacitance

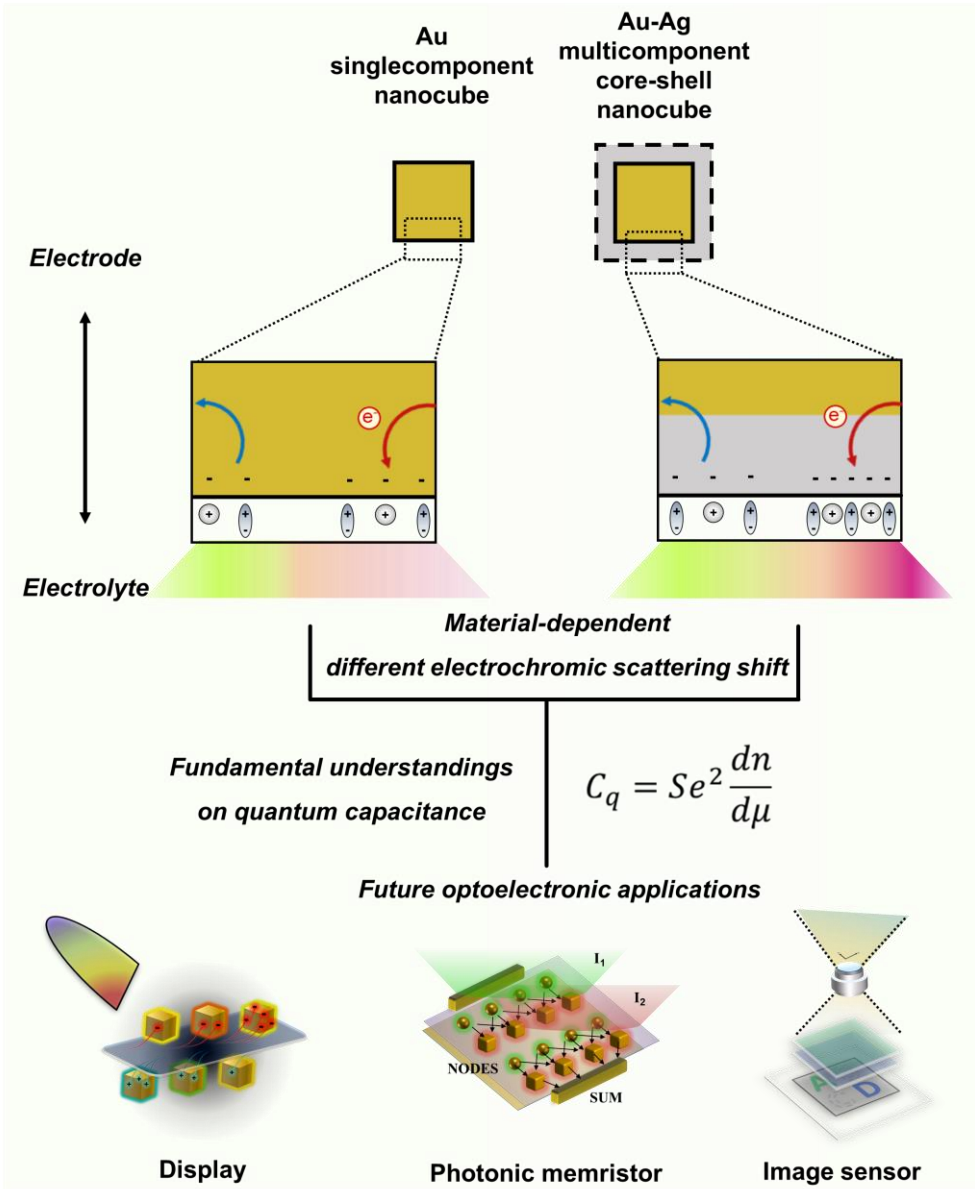

Figure 3.1. Schematic illustration of material-dependent different electrochromic scattering shift of Au and Au-Ag nanocubes originating from quantum capacitance and applicable future optoelectronic applications.

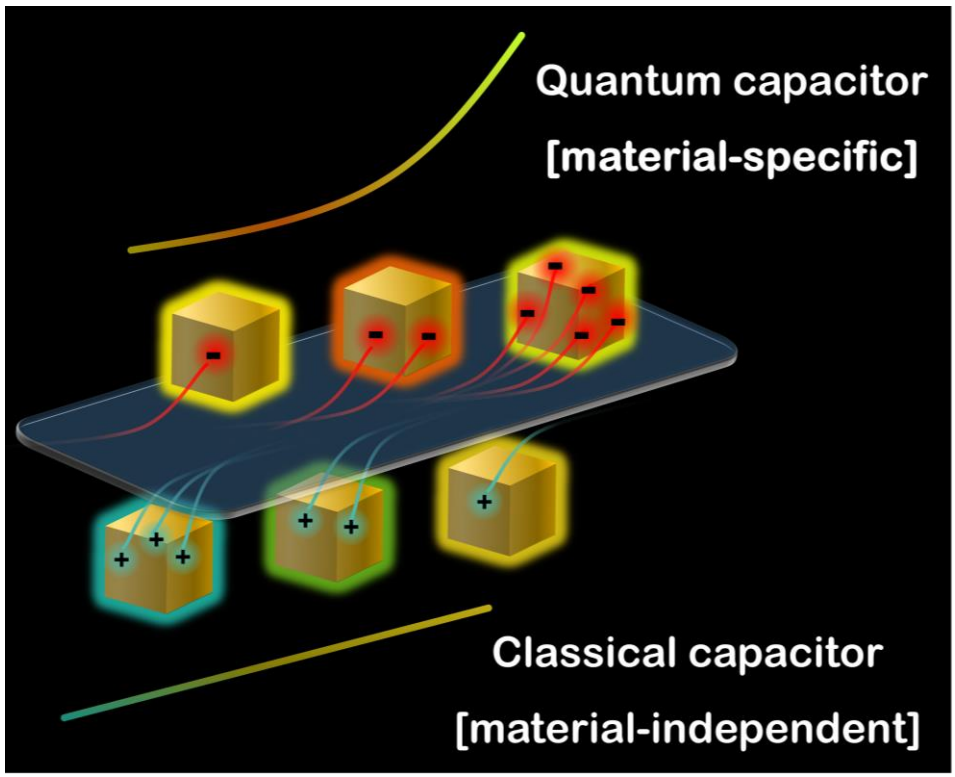

Figure 3.2. Simplified graphic representing the findings on the significance of material-dependent quantum capacitance in plasmonic electrochromism.

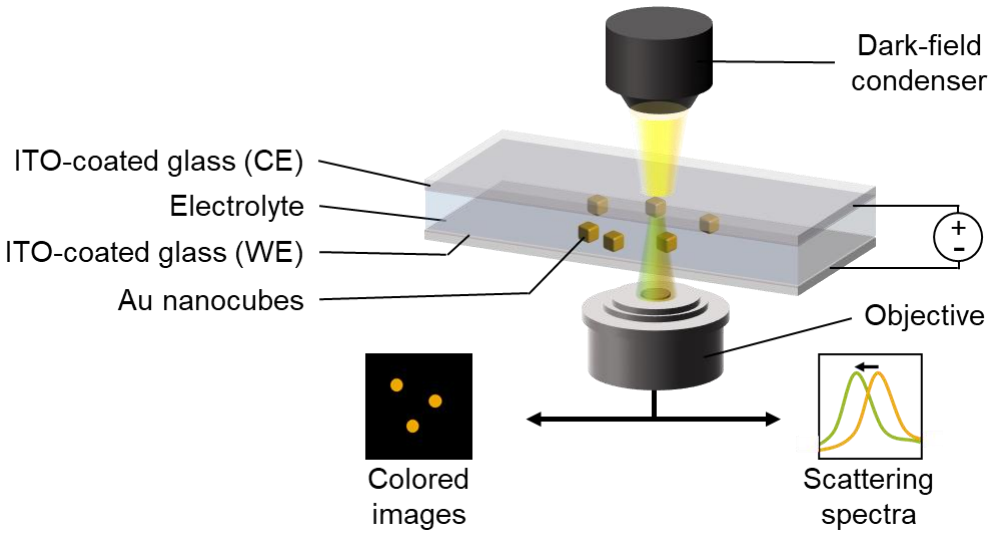

Figure 3.3. Schematic representation of the electrochromic device stack in the setup of a dark-field-correlated scattering spectroscopy.

3.2. Experimental Methods

Basis of the Experimental Design

In a typical study, we used single-crystalline AuNCs with an average size of 52.83 ± 0.65 nm, prepared by following to a previously reported procedure (**Figure 3.4**).[81] The prepared AuNCs displayed a scattering-dominant LSPR extinction maximum at 560 nm, which is consistent with the single-particle scattering spectrum. Au@AgNCs were also prepared to investigate the role of surface material in plasmonic electrochromism. A uniform Ag shell 7.21 ± 0.22 nm thick was coated on each AuNC, forming ~67 nm Au@AgNCs. Next, we then fabricated the electrochromic device stack. As shown in **Figure 3.3**, we built an electrochromic device stack with a two-electrode system composed of two indium tin oxide (ITO) thin films on glass substrates facing each other. One microliter of a 20 pM colloidal AuNC suspension was drop-coated on one side of the electrode. The electrode was then thoroughly washed with ethanol and isopropyl alcohol and confirmed to have the surfactant efficiently removed (**Figure 3.5**). The dispersion of individual nanocubes was verified by scanning electron microscopy (SEM) (**Figure 3.6**) and as well by dark-field imaging (**Figure 3.7**). A solution of acetonitrile containing 0.1 M tetrabutylammonium hexafluorophosphate ($TBAPF_6$) was

used as an electrolyte, because this electrolyte offers one of the widest potential windows with an extended stability. The electrolyte solution was sealed between the electrodes for in situ dark-field imaging and scattering spectroscopy. The back side of the substrate was grounded, and the electrical potential was applied to the stable open circuit voltage, which differs by ~ 0.45 V from the standard hydrogen electrode (SHE) (**Figure 3.8**).

Colloidal synthesis of plasmonic Au nanocubes

We first prepared homogeneous cetyltrimethylammonium chloride (CTAC)-capped single-crystalline Au nanocubes with LSPR extinction maximum at 560 nm by following a previously reported procedure. In brief, CTAC-capped 10 nm colloidal Au nanospheres were synthesized by seed-mediated growth using 2 mL of 200 mM CTAC, 1.5 mL of 100 mM ascorbic acid, and 2 mL of 0.5 mM $HAuCl_4$ on 1–2 nm seeds (obtained by $NaBH_4$ reduction) dispersed in a CTAB solution.[82] Then, nanocubes were grown on 22.7 pM of as-prepared 10-nm Au nanospheres by mixing them with 6 mL of 100 mM CTAC, 30 μL of 20 mM sodium bromide, and 390 μL of 10 mM ascorbic acid solutions followed by the injection of 6 mL of a 0.5 mM $HAuCl_4$ solution in one go. Similarly, Au nanocubes with rounder edges were also obtained by simply changing the sodium bromide concentration from 20 mM to 6 mM and used for verifying shape effects. The colloidal nanocube products were centrifuged and redispersed in de-

ionized water twice before using in further experiments.

Colloidal synthesis of Ag shell-coated Au nanocubes

Ag shell-coated Au nanocubes (Au@Ag nanocubes) were prepared by partially adopting the procedure from the previous report.[81] The reaction was performed in a 1.5 mL-scale while all reagents were well dissolved in DIW. First, 400 μL of a previously synthesized Au nanocube solution (10 pM) was mixed with 400 μL of a 10 mM CTAC solution and 200 μL of a 50 mM L-ascorbic acid solution. The solution was heated in a 60ºC water bath for 10 min. To initiate the reaction, 40 μL of a 0.5 mM $AgNO_3$ solution was added to the mixture and uniformly mixed by vortex. After incubating the reaction solution for 3 h in the 60ºC water bath, the synthesized nanoparticles were gathered through centrifugation twice (6,000 rpm, 10 min) and redispersed in DIW for further experiments.

Fabrication of electrochromic device stack

As shown in **Figure 3.3**, we fabricated an electrochromic device stack with a two-electrode system composed of two 100 μm-thick indium tin oxide (ITO) thin films (15 Ω/sq) on 1.0 mm-thick glass substrates facing each other. The ITO films were sequentially cleaned by sonicating in acetone for 10 min and then washing with ethanol and isopropyl alcohol,

and finally dried by blowing N_2 gas before use. One micro-liter of an 8 pM colloidal Au nanoparticle suspension was drop-coated on one side of the electrode. The nanoparticle-coated ITO electrodes were washed with ethanol and isopropyl alcohol, and finally dried by blowing N_2 gas. The dispersion of individual nanocubes was verified by scanning electron microscopy (SEM; **Figure 3.6**) and by dark-field imaging (**Figure 3.7**). A solution of acetonitrile or DMSO containing 0.1 M tetrabutylammonium hexafluorophosphate ($TBAPF_6$) was used as the electrolyte. The electrolyte solution was sealed between the two electrodes by disposable silicone isolators 1.3 cm in diameter. The back of the glass substrate was grounded, and the electrical potential was applied to the stable open-circuit voltage. The stability of the fabricated device was ensured up to ±4 V by SEM analysis. All electron microscopy studies for identifying morphologies were performed at the National Center for Inter-University Research Facilities (NCIRC) in Seoul National University.

In situ dark-field electro-spectroscopy and electrochemical spectroscopy

The dark-field images and scattering spectra were collected in situ with liner-sweep voltammetry in the potential ranges of 0 V to 5 V and 0 V to −5 V, respectively, at a scan rate of 50 mV/s. The as-prepared electrochromic device stack was placed on the grounded microscopic stage and connected to a portable CORRTEST CS350 electrochemical

workstation (China). In situ dark-field microscopy and scattering spectroscopy were performed on a Carl Zeiss Axiovert 200M dark-field microscope equipped with a Plan-NEOFLUAR X40/0.6 NA objective, an Axiocam 506 CCD camera (Germany), a Dongwoo Optron MonoRa320i monochromator (South Korea), and an ANDOR iDus 420 CCD detector (UK). The spectra were collected at time intervals of 1.0 second. For electrochemical impedance spectroscopic analysis, a BioLogic VMP3 electrochemical workstation (France) was used. The applied voltage was varied stepwise by 50 mV/sec and the frequency was varied from 1 Hz to 1 MHz with sinusoidal alternating current. The capacitance of the metallic nanoparticles was estimated by fitting the measured Nyquist Impedance into the standardized equivalent circuit model. There was no significant sign of parasitic current and the OCV was stabilized until reaching approximately 247 mV versus the Ag/AgCl reference electrode until the deviation fell within 5 mV.

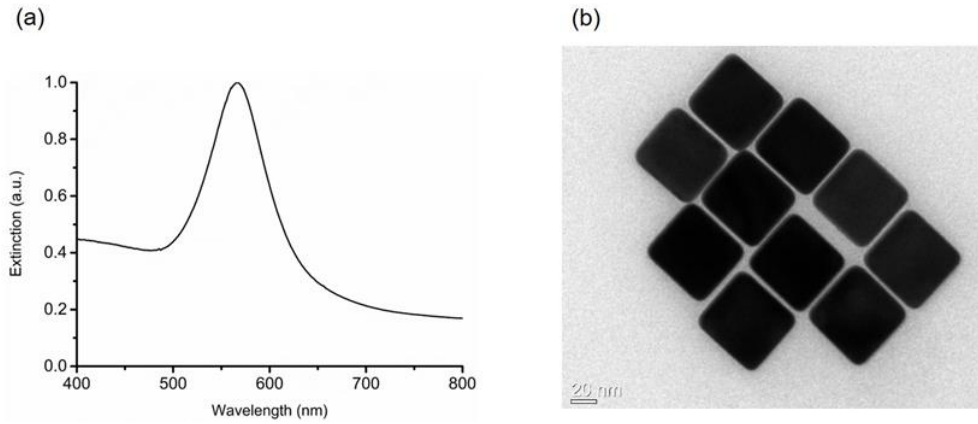

Figure 3.4. (a) Normalized extinction spectrum of colloidal Au nanocubes prepared by a wet-chemical reduction method as described in the experimental methods. (b) TEM image of the as-prepared Au nanocubes.

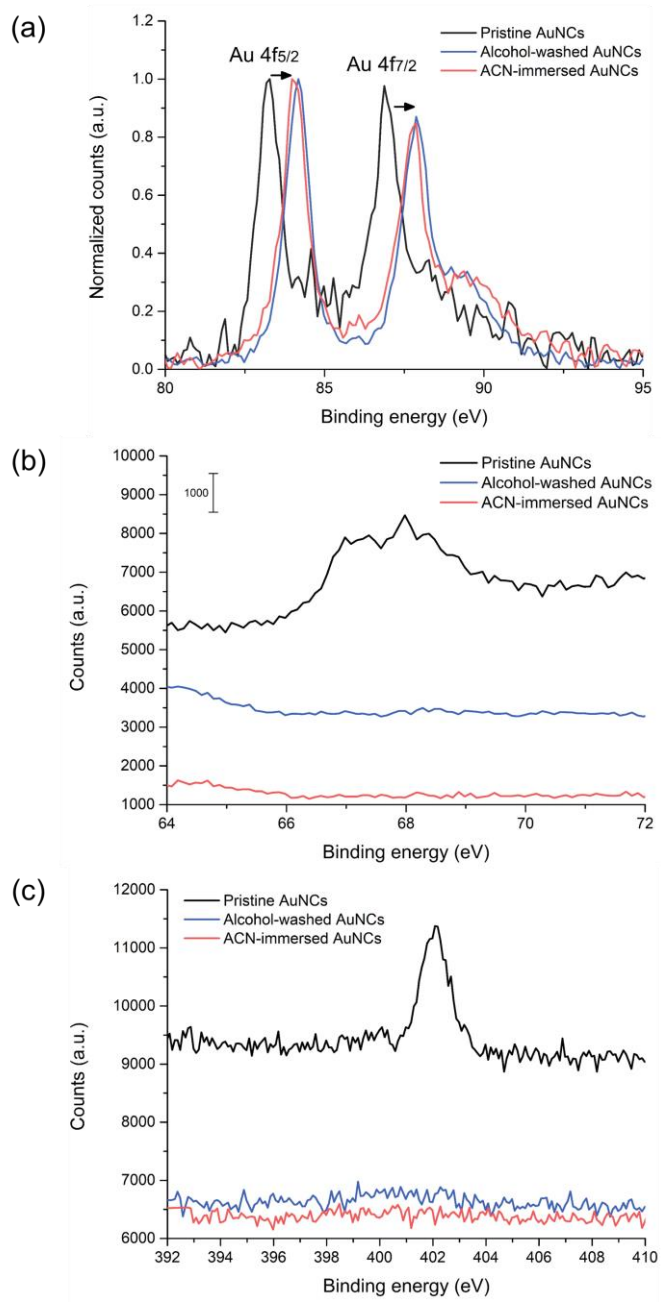

Figure 3.5. X-ray photoelectron spectroscopy (XPS) study for washing effect on Au (a), Br (b), and N (c) species on the Au nanocube surface. The results imply that the pristine Au nanocubes are mostly capped with CTAB as predicted in a previous study.[82] Most of the surfactants were removed at the washing step (ethanol and isopropyl alcohol) and no significant difference was found on the immersion step (acetonitrile). Au 4*f* binding energies (4*f* 5/2 and 4*f* 7/2) blue-shifted as electron-donative halide ions left from the Au surface during the washing step.

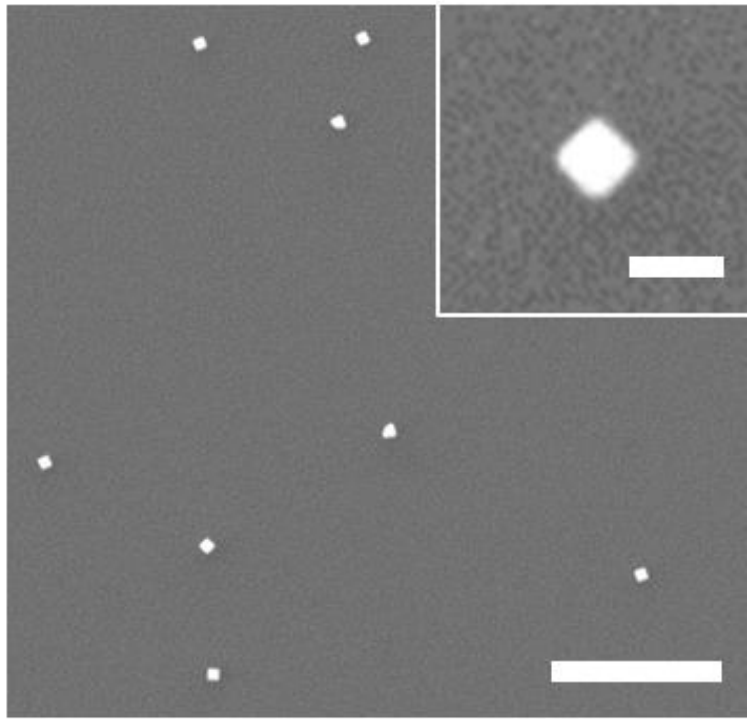

Figure 3.6. SEM images of the AuNCs loaded on the ITO-coated glass substrate. Scale bars are 5 μm for the main image and 100 nm for the inset.

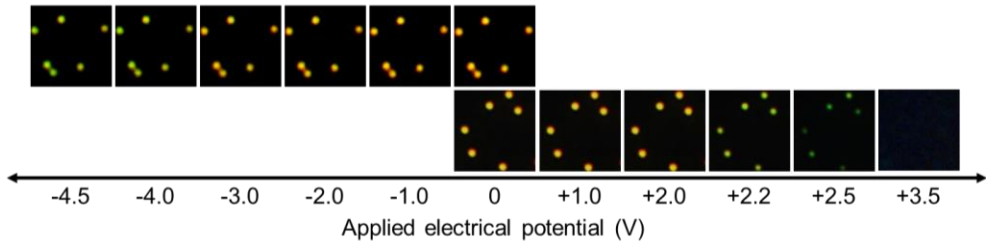

Figure 3.7. Dark-field microscopic images of the AuNCs under externally applied electrical potentials ranging from 0 V to −4.5 V (cathodic) and 0 V to 3.5 V (anodic), respectively.

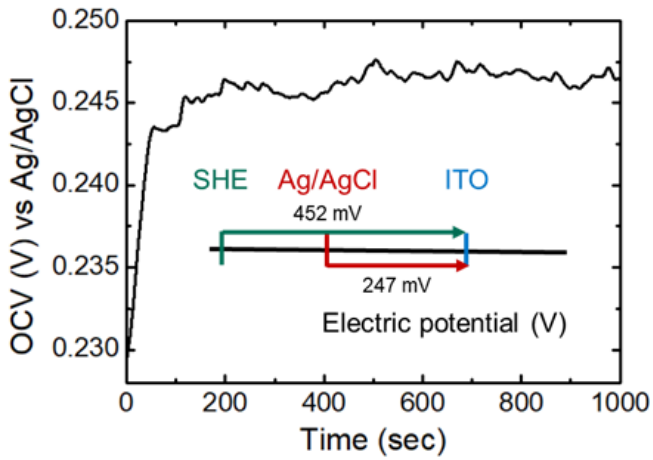

Figure 3.8. Open circuit voltage (OCV) of the electrochromic device stack measured versus the Ag/AgCl reference electrode. The OCV was stabilized until the deviation fell within ±5 mV.

3.3. Results and Discussion

First, we evaluated the voltage dependence and threshold voltage of the electrochromic AuNCs. The dark-field images and scattering spectra were collected in situ simultaneously with linear-sweep voltammetry performed in the potential range of 0 V to 3.5 V and 0 V to −4.5 V, respectively, at a scan rate of 50 mV/s (**Figure 3.9**). The as-prepared electrochromic device stack was placed on the grounded microscopic stage and connected to an electrochemical workstation. We secured the different trends in morphology and color change of the AuNCs for negative and positive applied potentials under the linear-sweep voltammetry and chronoamperometry (see also captions of **Figures 3.9 and 3.10** for details). Structural deformation of AuNCs was observed in the positive potential window while there was no noticeable shape change in the negative potential window (**Figure 3.10**). It confirms that the contour (**Figure 3.11**) and maximum wavelength plot (**Figure 3.12**) of the obtained scattering spectra show atypical external electrical potential dependency. Three distinct dynamic ranges of applied voltage are labeled with Roman numerals as I, II, and III in **Figure 3.12**. The three distinct dynamic potential ranges indicate that each shift is governed by different operational principles. The most typical electrochromic behavior is based on the capacitive charging effect (I). As shown by the maximum wavelength shift in **Figure 3.12**, the plasmonic scattering spectral peak slowly but steadily red-shifts with an increase in the

applied electric potential from approximately −2 V to 1.5 V. This marginal monotonic increase can be attributed to the change in the free carrier concentration and the subsequent shift in the plasmon resonance frequency, according to the classical model.[74] The external voltage applied to the ITO substrates capacitively charges and discharges the AuNCs. The electrochromic behavior of the system in range I is not significant, because the change in the carrier concentration of noble metals is not largely influenced, because of the sufficiently available free electrons in the metal. When the applied electrical potential exceeds a certain threshold, the plasmonic scattering spectra shift abruptly and show different slopes.

In a highly positive-voltage regime above 1.5 V (designated by "II" in **Figure 3.12**) for AuNCs in an acetonitrile solution of 0.1 M $TBAPF_6$, the maximum scattering wavelength blue-shifted rapidly over 15 nm, the scattering intensity decreased drastically, and the signal was almost turned off. This tendency matches well with the microscopic images in **Figure 3.9**. The dimming and blue-shift under highly positive voltages can be largely attributed to the oxidation of AuNCs, presumably analogous to the recently reported photo-assisted electro-dissolution of Au nanoparticles.[83]

At highly negative potentials beyond the threshold (designated by "III" in **Figure 3.12**), the maximum wavelength underwent a noticeably faster blue-shift, compared to that in the simple capacitive charging region (designated by "I" in **Figure 3.12**). Upon taking the linear regressions of the maximum scattering wavelength from 0 V to −2.0 V and from −2.0 V to

−4.0 V (ranges I and III in **Figure 3.12**), respectively, the rate of shift is found to increase dramatically from 0.3 nm/V (i.e., 1.1 meV/V) to 2.1 nm/V (i.e., 7.7 meV/V) and to peak at −2.95 V with the rate of 8.2 nm/V (i.e, 30 meV/V). The result implies, in principle, that the free electron concentration in a AuNC is increased by ~0.21% when the applied voltage reaches −2.0 V and by 1.7% when it reaches −4.0 V, compared to that of the initial state.

We also verified the reversibility of such an unexpected strong blue-shift within a highly negative potential region by applying square potential waves. The maximum scattering wavelength of the Au nanocubes responded over 10 cycles under the alternating applied potential from 0 to −3.7 V in 0.05 (**Figure 3.13** and **Figure 3.14**) and 0.25 Hz (**Figure 3.15** and **Figure 3.16**). The time derivative of the maximum wavelength showed that the response speed topped ~1−2 nm/s for 0.05 Hz (**Figure 3.14**) and 10−20 nm/s for 0.25 Hz (**Figure 3.16**). The electrochromic response accrues for ~4 s in the case of 0.05 Hz and ~0.5 s in the case of 0.25 Hz, while the chronoamperometric response abates within ~50 ms for both cases. We concluded that this phenomenon is not based on any persisting chemical reaction while an electrical rate-determining step, such as electrical double layer formation, plays a role in our electrochemical system.

Remarkably, the strong blue-shift in the highly negative region was not accompanied by a scattering intensity decrement unlike at the highly positive-voltage case when the scattering was turned off. This suggests that

the electron loss by faradic current or morphology change is not a major factor of the spectral shift. We attribute this newly found electrochromic behavior to the largely drifted Fermi level that results in an increased rate of free electron generation by potential increment, implying the change in the metallic property. Interestingly, the full width at half-maximum (fwhm) of the spectra from the nanocubes in acetonitrile with 0.1 M $TBAPF_6$ shares the similar threshold potential to that of the scattering maximum. The trend in fwhm change indicates the varying surface plasmon damping, and this must be explained beyond the classical regime. Meanwhile, the similar trends in the spectral shift and traits, such as threshold potential, were observed with the dimethyl sulfoxide as a solvent instead of the acetonitrile, with a similar dipole moment but different chemical reactivities (**Figure 3.17**). This also suggests that the chemical property of surface molecules is not the major factor for the electrochromic response of the AuNCs; instead, the change in the intrinsic charging characteristic of the metallic nanoparticles is the key factor for the significant change in plasmon resonance energy.

By analyzing electrochemical impedance spectroscopy (EIS), we found more information on the variation of the electrical properties of these cubes that could not be explained by the classical capacitive charging (see **Table 3.1**). First, the electrochromic device stack was simplified into a generally accepted equivalent circuit model for regression, as shown in **Figure 3.18**. The contact between ITO and AuNC is ohmic ($R_{interlayer}$), and

the interface between AuNC and electrolytes is capacitive (C_{AuNC}). $R_{interlayer}$ is a junction overpotential and induces a small voltage drop. The electrical double layer is a major cause of the capacitive characteristics in this system, and C_{AuNC} represents the electrical double layer at the interface between AuNC surface and electrolytes. These two circuit components ($R_{interlayer}$ and C_{AuNC}) are serially connected, and any other routes such as Faradaic reactions are represented by R_{AuNC}. Note that the R_{AuNC} parameter is parallelly connected to the C_{AuNC} parameter. As shown in **Figure 3.19**, however, R_{AuNC} is very high ($\sim 10^5\ \Omega$) in our case, and eventually, R_{AuNC} becomes almost a nonfactor, compared to C_{AuNC}. The circuit can be basically considered as a series circuit between $R_{interlayer}$ and C_{AuNC}. As a result, charge flows through the ohmic contact between the AuNC and the ITO and then capacitively accumulates in the AuNC.

Consequently, charge flows through the $R_{interlayer}$ parameter and then capacitively accumulates on the surface of AuNC. Then, impedance of the system was measured under the alternating current within the cathodic potential range. We verified that R_{AuNC} is significantly larger than $R_{interlayer}$, and the charge conducts through the resistive ITO/AuNC interface and is accumulated on the AuNC by the electrical double layer capacitance, while the electrolyte remains stable. It has been also confirmed that the capacitance of the AuNCs is almost constant in a low voltage range and peaks after −3 V (**Figure 3.19**). The resulting trend in LSPR shift during charging was expected by the Lorentz−Drude model, as in **Figure 3.20**,

which reflects the increasing blue-shift rate of the measured scattering spectra. When potential was swept to −4 V, a particle was estimated to be charged negatively by 37 fC, which is an ~3.1% increase of the free electron density on the surface of AuNCs. This is in close agreement with the spectroscopically estimated value of 1.7%.

Meanwhile, the linear-sweep voltammetry of various electrolytes and solvents confirmed that ionic electrolyte was the decisive factor in electrochemical current, and acetonitrile was stable in our potential window (**Figure 3.21**). The electrochemical currents showed no critical relevance to the electrochromic response for a different electrolyte ($NaClO_4$) or solvents (sulfolane and dimethylsulfoxide (DMSO)). Furthermore, for the acetonitrile solution with 0.1 M of $TBAPF_6$, no significant faradaic current variation was found near the onset potential while the Faradaic current has a peak after −4 V (see details in **Figure 3.22**). In addition, any parasitic current or unexpected chemical reduction that leaks charged electrons may come down to a red-shifting factor, which is not the major case here.[84]

To verify whether the capacitive electrochromism has a dependency on the type of a surface metal, unlike classical predictions, we changed the surface of AuNCs by uniformly forming Ag shells on AuNCs, as described earlier (**Figure 3.23**) via heteroepitaxial growth. We found different electrochromic patterns including blue-shift thresholds from the scattering spectra of AuNCs and Au@AgNCs (**Figure 3.24**). The DFT (PBE-GGA) calculations suggest the DOSs of Au and Ag possess remarkably different

profiles when the electronic potential is elevated by a few eV from the Fermi energy (**Figure 3.25**). We further estimated the additional charge (Δq) by increasing the Fermi level (ΔE_f) based on **Equation 3.1** while $g(E)$ represents DOS and f(E) is the Fermi−Dirac distribution function:

$$\Delta q = \int_{E_{f0}}^{E_{f0}+\Delta E_f} g(E) f(E)\, dE \qquad \textbf{(3.1)}$$

Here, $g(E)$ is proportionally related to the quantum capacitance, and resonance frequency is proportionally related to the square root of the total number of free carriers ($n + \Delta q$). **Figure 3.26** shows how the Lorentz−Drude model predicts the abnormal blue-shift of LSPR frequencies of AuNCs and Au@AgNCs along the increased Fermi level. It is noticeable that the magnitude of the shift rate is increasing, and the tendency change in LSPR of AuNCs appears sooner than that of Au@AgNCs, as predicted in their DOS profiles. Such findings are contradictory to the theory that geometrical capacitance has no dependency on the type of the electrode metal. This implies that the electrochromic behavior of a capacitively charged plasmonic nanoparticle is dependent on the surface material.

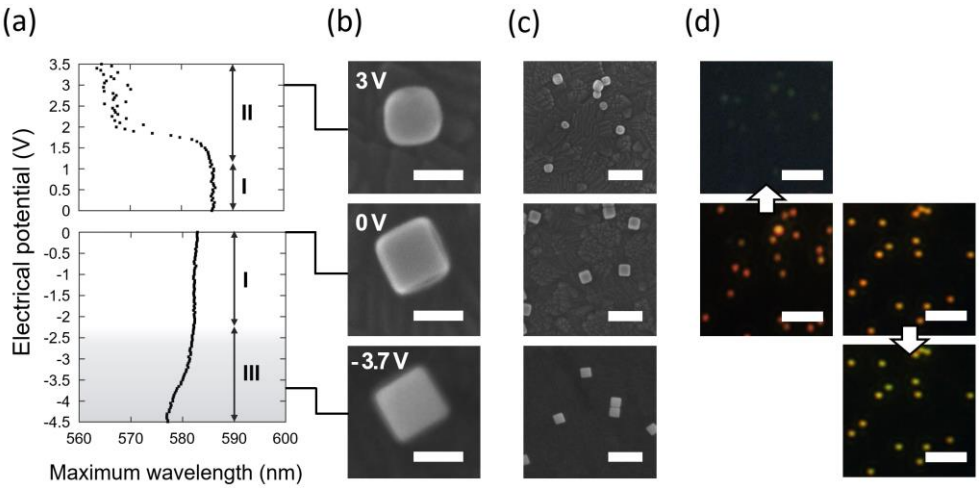

Figure 3.9. Morphology and color changes of Au nanocubes under the different potential ranges showing the three different dynamic ranges (noted in Roman numerals). (a), SEM images in high-magnification (b) and low-magnification (c) and corresponding dark-field images (d) of the Au nanocubes under the differently applied potentials are shown. The electrical potential was applied 50 mV/s in a linear-sweep voltammetry. The scale bars are 50 nm, 200 nm and 5 μm for (b), (c) and (d), respectively.

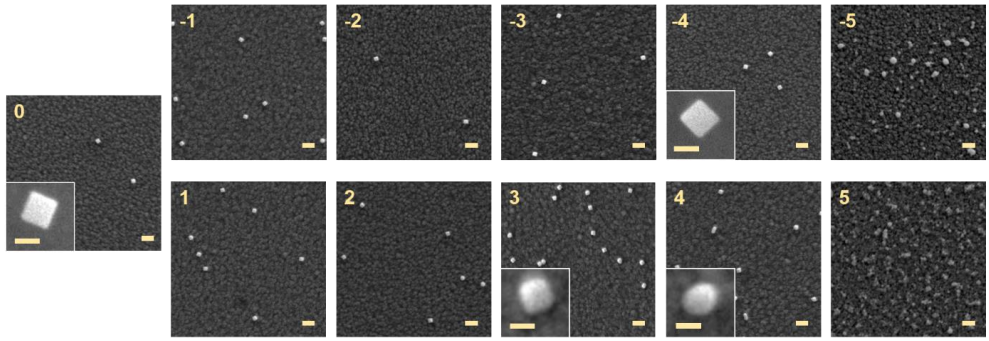

Figure 3.10. SEM images of the Au nanocubes drop-coated on the ITO-covered glass substrate. Each sample was fabricated into an electrochromic device stack, filled with acetonitrile solution with 0.1M $TBAPF_6$, and individually applied under constant voltages as noted for 30 seconds before imaging under the scanning electron microscopy. The scale bars are 200 nm (50 nm for inset images).

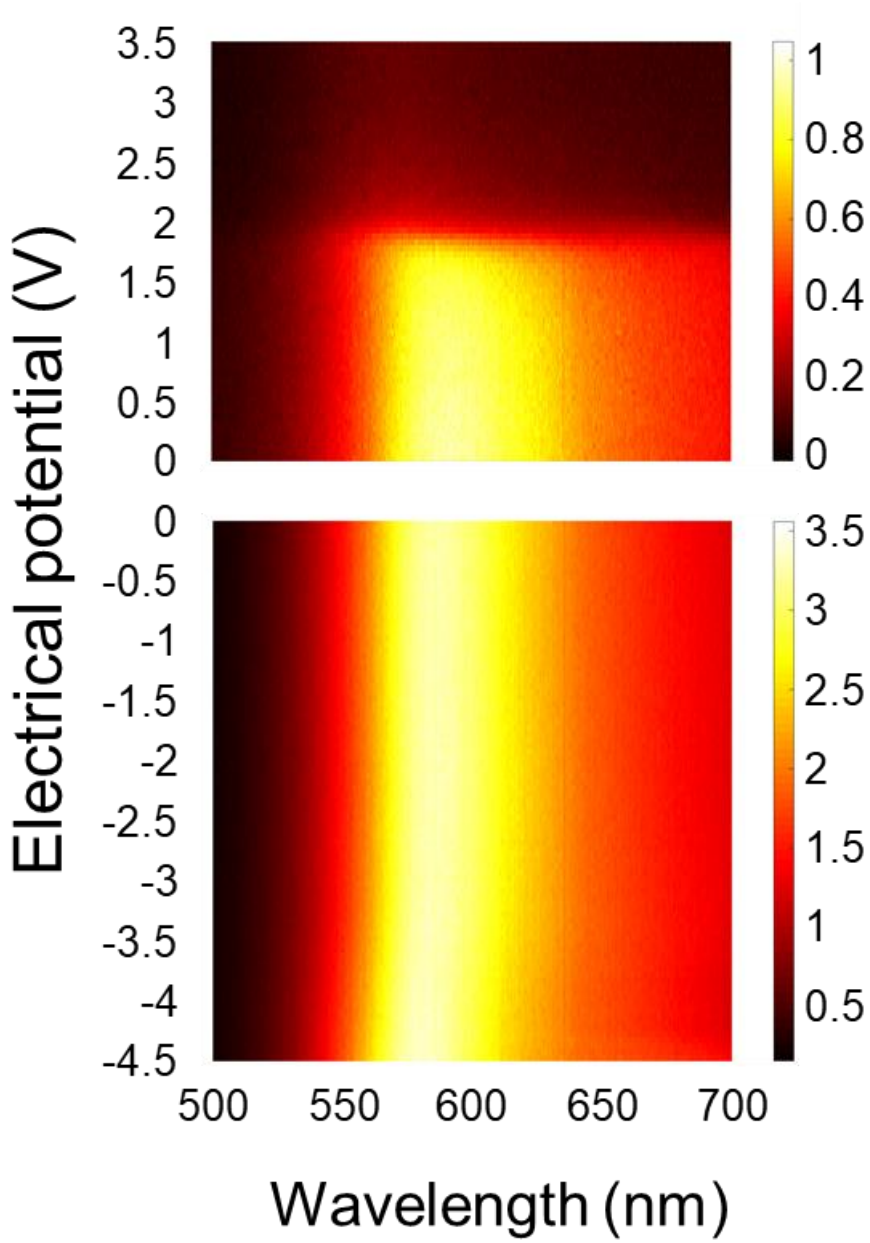

Figure 3.11. Contour plots of the scattering spectra under the anodic (upper) and cathodic (lower) potentials through an acetonitrile solution of 0.1 M $TBAPF_6$.

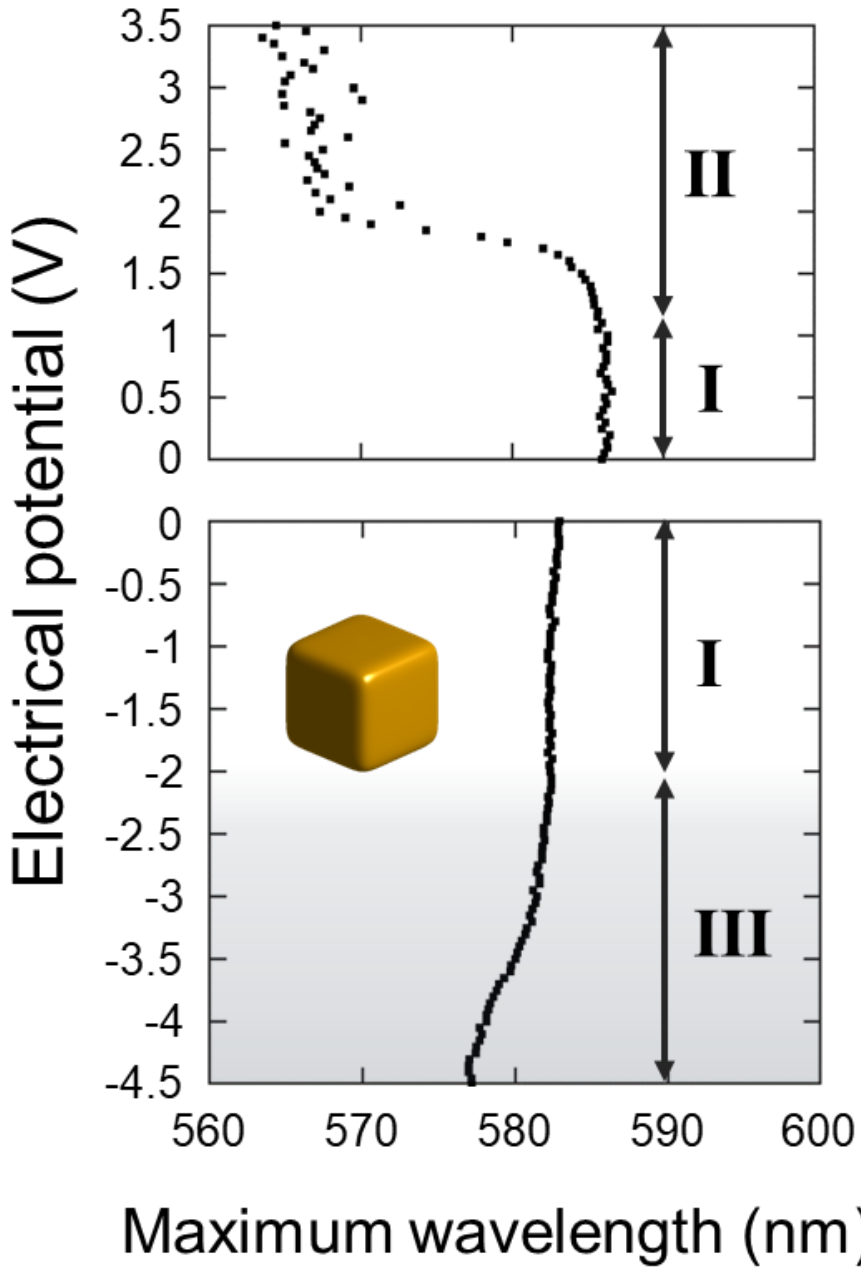

Figure 3.12. Shift in the scattering maximum wavelength along the anodic (upper) and cathodic (lower) potential sweep showing the three different dynamic ranges (noted in Roman numerals).

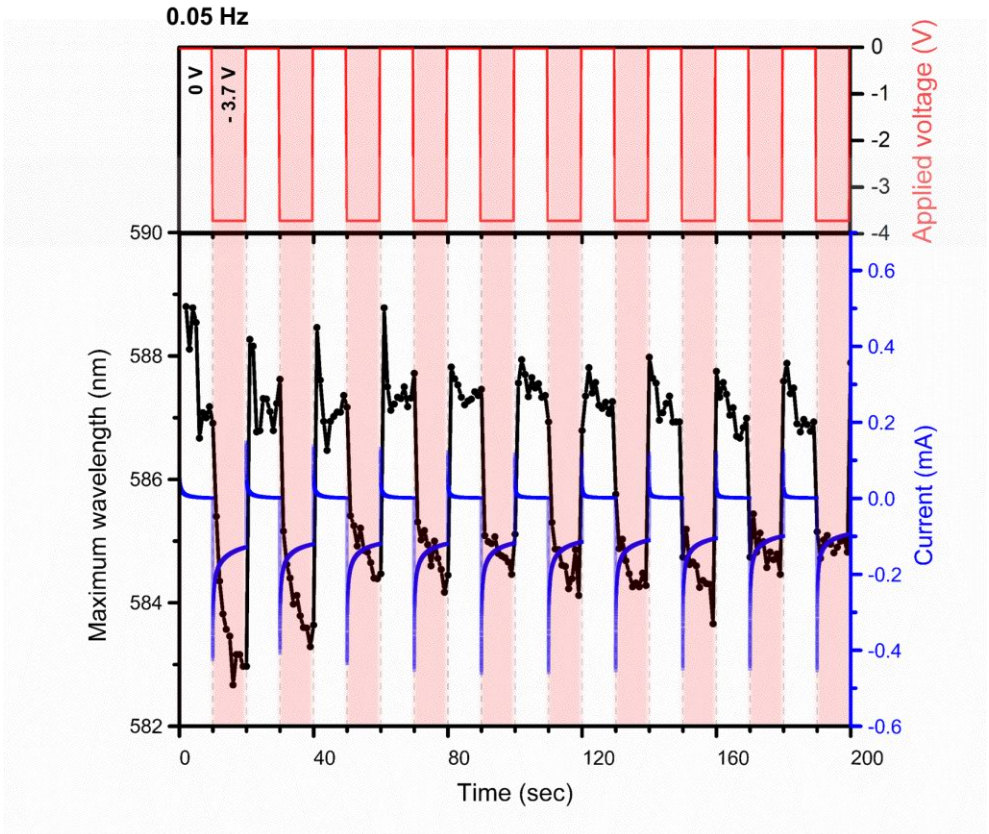

Figure 3.13. The reversible electrochromic response of Au nanocubes. The above shows maximum scattering wavelength shift in response to square potential waves (0 V to -3.7 V versus open circuit voltage) at 0.05 Hz for 10 cycles. Chronoamperometric response is overlaid with blue lines.

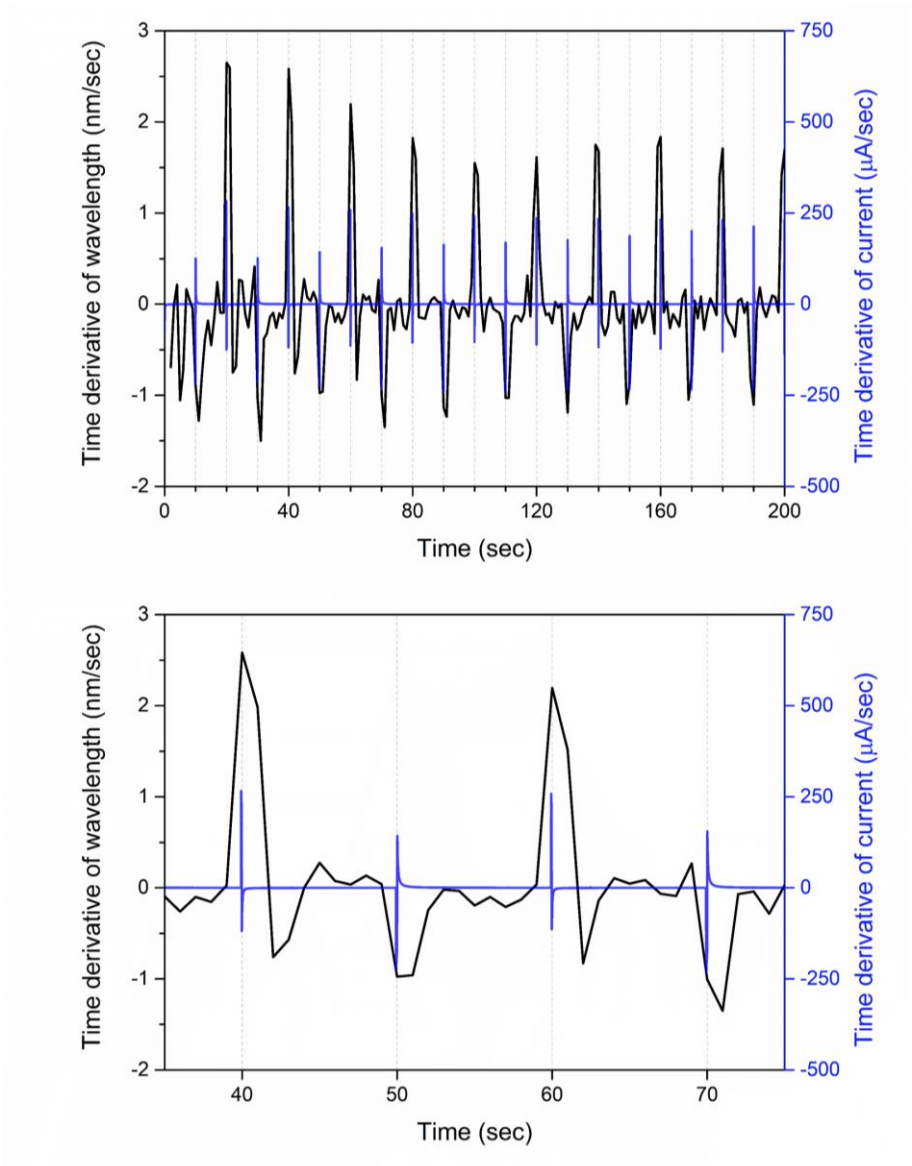

Figure 3.14. The time derivative of the reversibly responding maximum wavelength (0.05 Hz) and that of the current for 10 cycles (upper). The third and fourth cycles are magnified in lower.

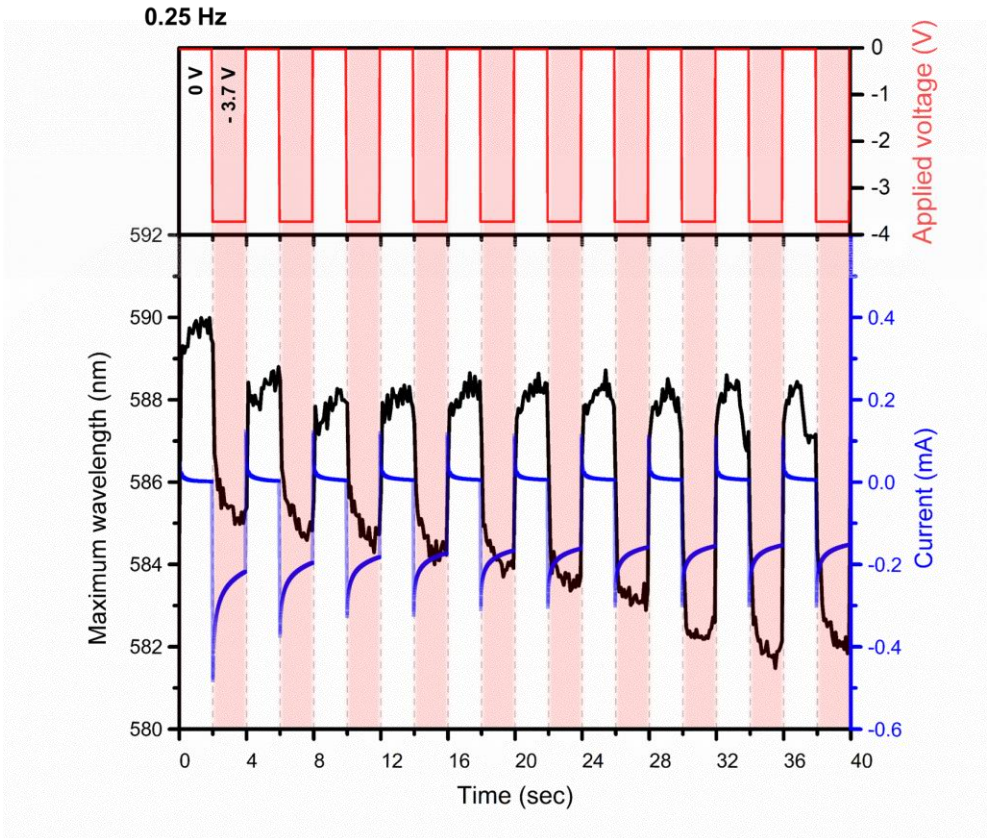

Figure 3.15. The reversible electrochromic response of Au nanocubes. The above shows maximum scattering wavelength shift in response to square potential waves (0 V to -3.7 V versus open circuit voltage) at 0.25 Hz for 10 cycles. Chronoamperometric response is overlaid with blue lines.

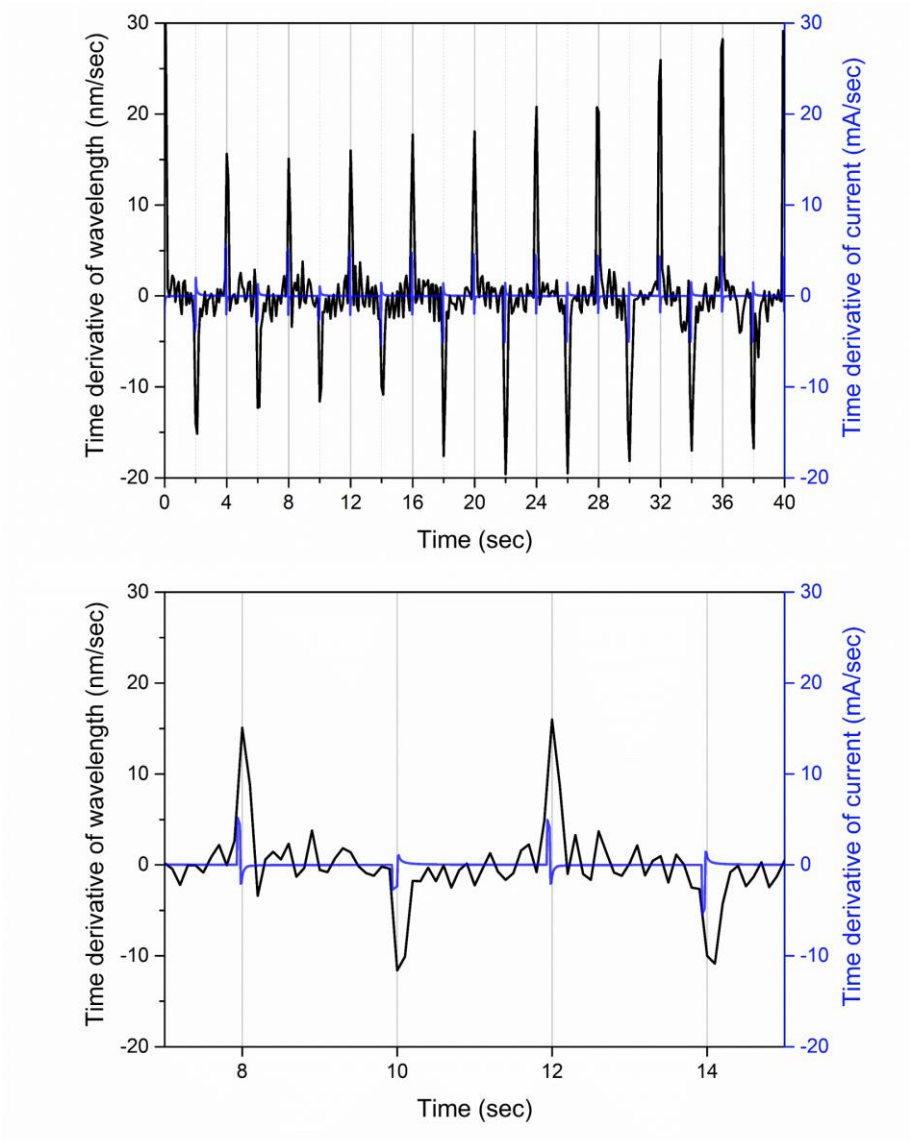

Figure 3.16. The time derivative of the reversibly responding maximum wavelength (0.25 Hz) and that of the current for 10 cycles (upper). The third and fourth cycles are magnified in lower.

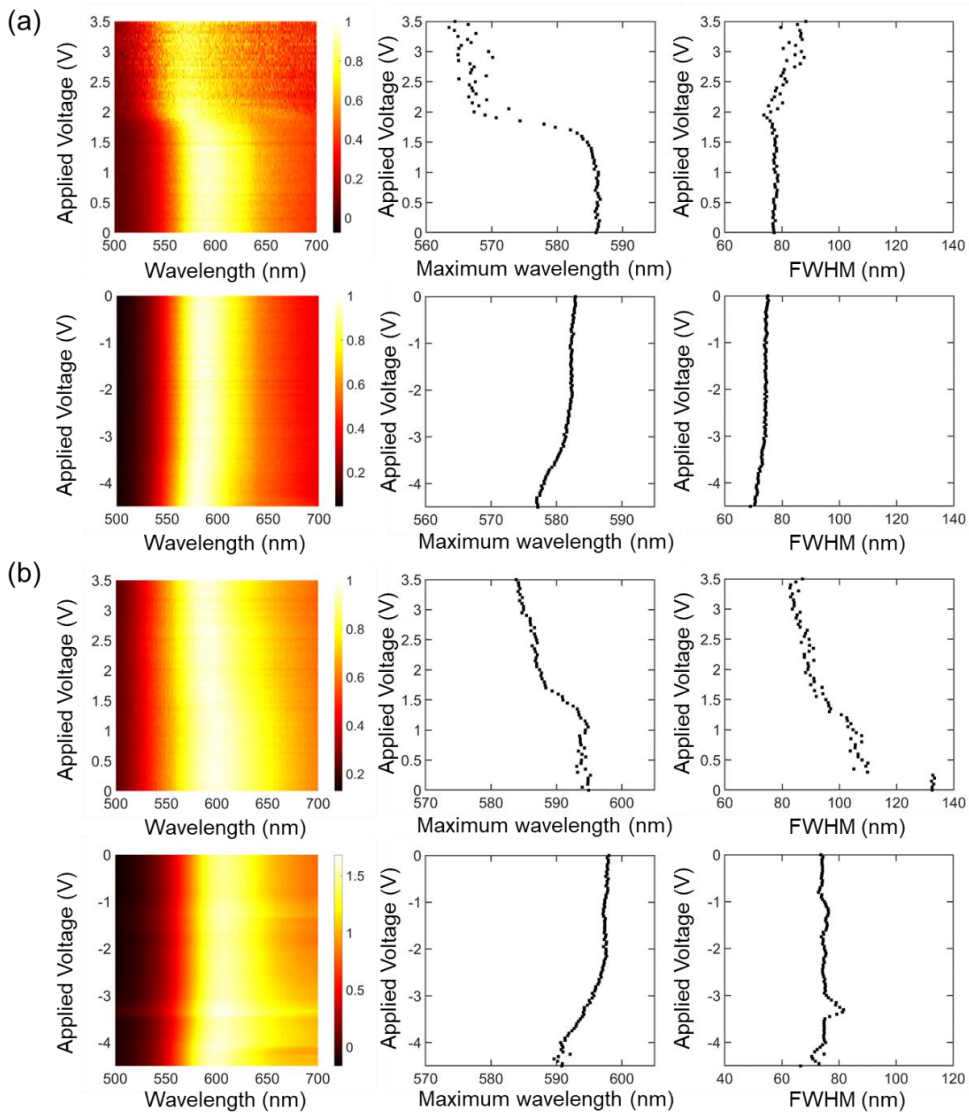

Figure 3.17. Contour plots of the normalized scattering spectra of sharp-edged nanocubes under applied bias (left), the shift in the maximum wavelength (center), and the full width at half maximum (FWHM) (right) in varying solvents. (a) The spectra acquired from the acetonitrile solution (0.1 M $TBAPF_6$) under positive (upper) and negative (lower) applied potentials, respectively. (b) The spectra from the dimethyl sulfoxide (DMSO) solution (0.1 M $TBAPF_6$) under positive (upper) and negative (lower) applied potentials, respectively.

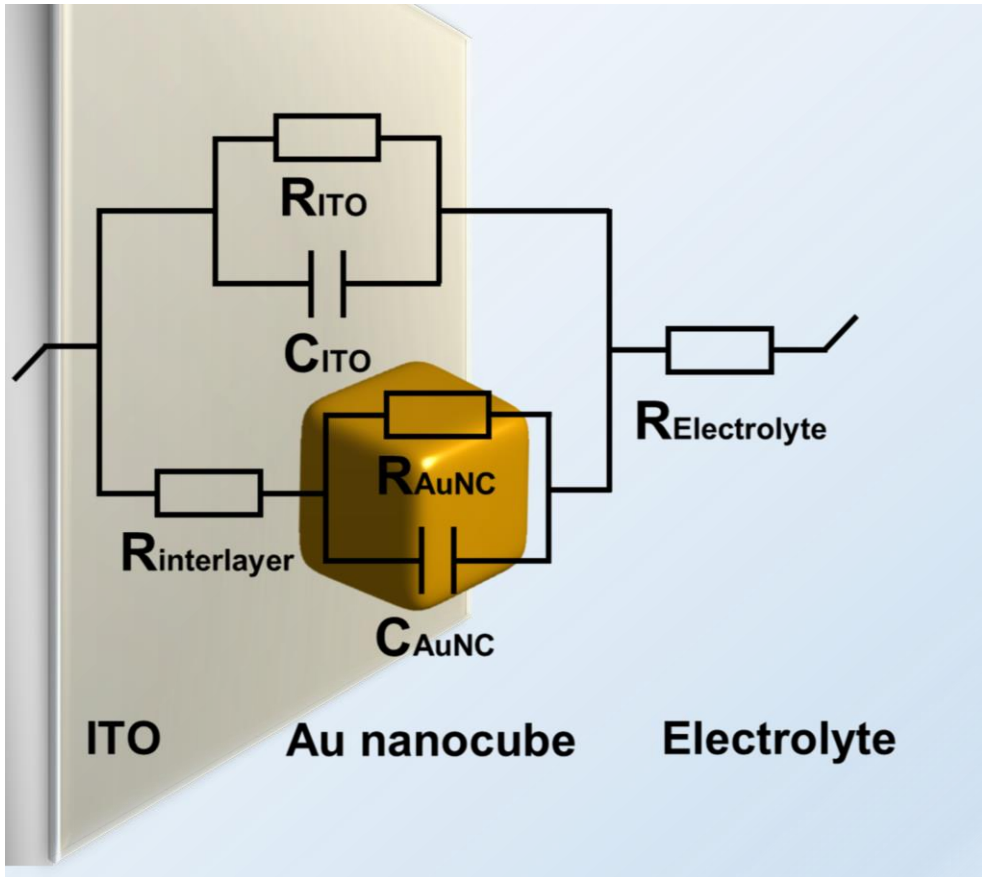

Figure 3.18. A designed equivalent circuit model of the electrochromic device stack. For electrochemical analysis

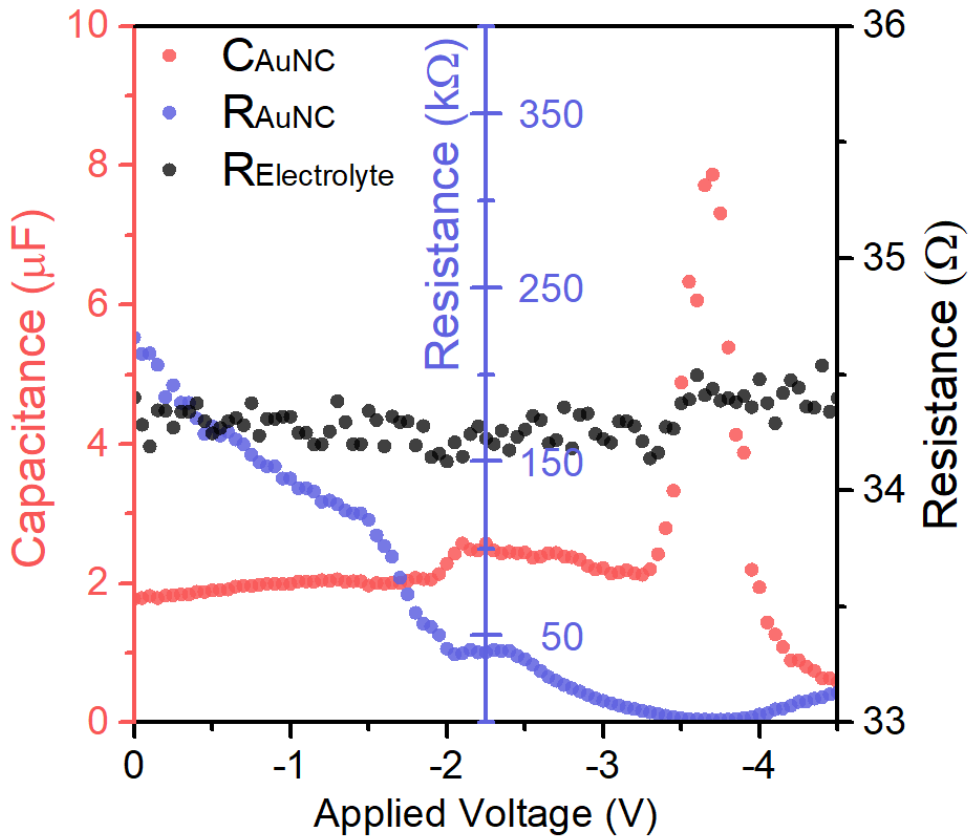

Figure 3.19. Voltage-dependent capacitance and resistance of the AuNCs and a constant resistance of the electrolyte analyzed by EIS (the red, blue, and black dots indicate the circuit parameters attributable to the capacitance of AuNCs, the resistance of AuNCs, and the resistance of electrolytes, respectively).

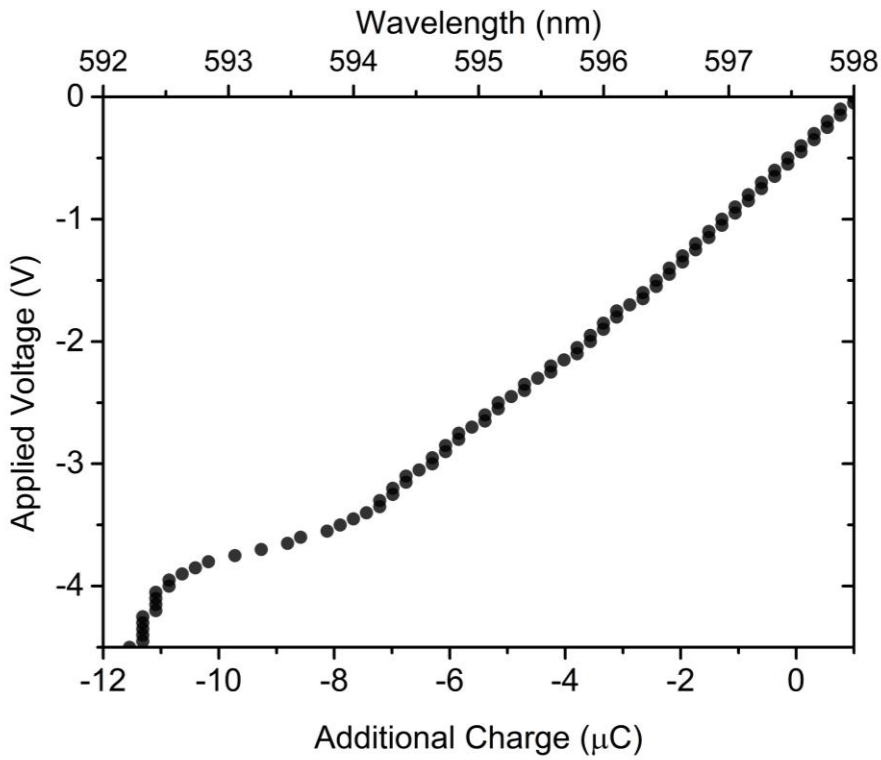

Figure 3.20. Electrochemical analysis of the AuNCs supported on ITO electrode. (a) A designed equivalent circuit model for the electrochromic device stack. (b) Voltage-dependent capacitance and resistance of the AuNCs and a constant resistance of the electrolyte analyzed by EIS (the red, blue, and black dots indicate the circuit parameters attributable to the capacitance of AuNCs, the resistance of AuNCs, and the resistance of electrolytes, respectively). (c) Estimated charge accumulation and corresponding plasmonic resonance wavelength predicted by the Lorentz-Drude model.

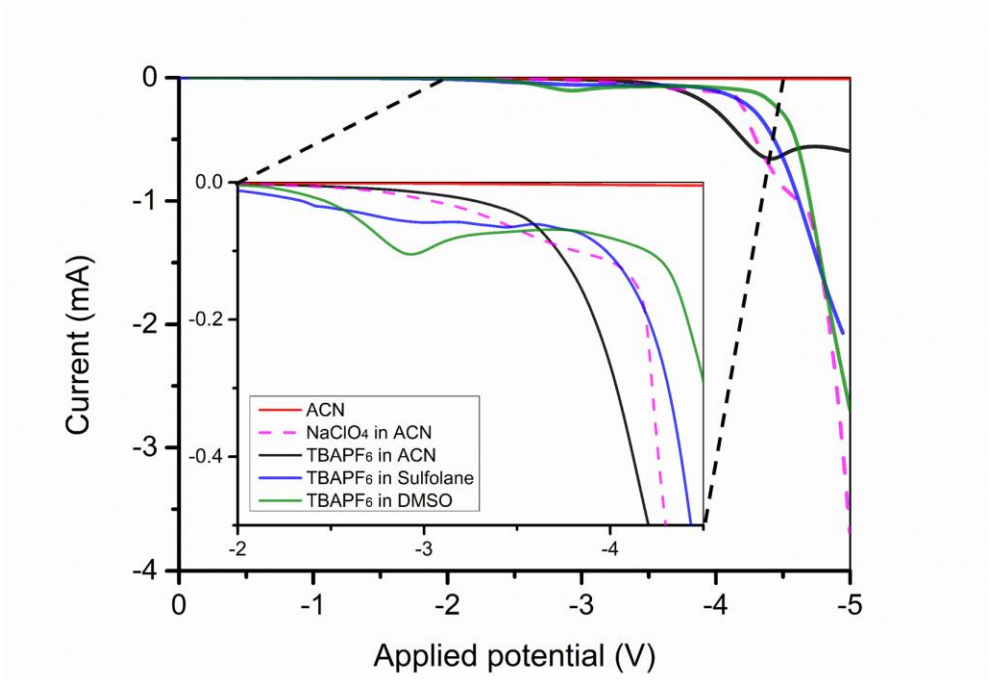

Figure 3.21. I-V curves of the acetonitrile solution without electrolyte (red solid line), acetronitrile solution with 0.1 M of $NaClO_4$ (pink dashed line), acetonitrile solution with 0.1 M of $TBAPF_6$ (black solid line), sulfolane solution with 0.1 M of $TBAPF_6$ (blue solid line), and DMSO solution with 0.1 M of $TBAPF_6$ (green solid line) in response to the linear-sweep voltammetry from 0 to -5 V versus open circuit potential. The non-linear spectral shift of AuNPs in acetonitrile with 0.1 M of $TBAPF_6$ starts from -2 to -3 V, while no significant Faradaic current was observed before -3 V for the black line and the Faradaic current peaks around -4 to -4.5 V.

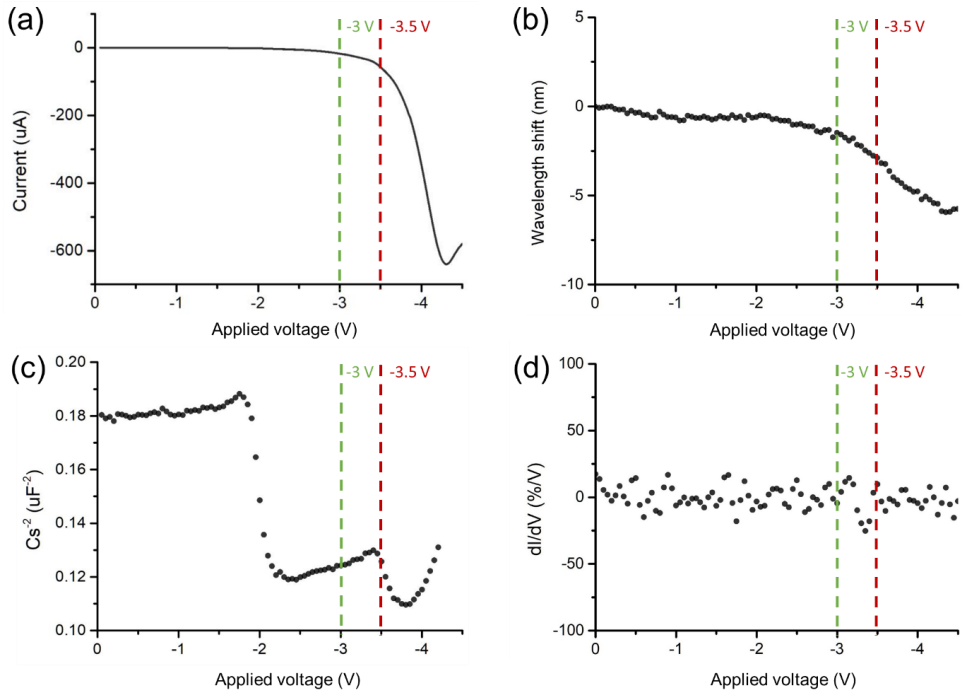

Figure 3.22. Voltage-dependent properties of the electrochromic device stack. (a) Electrochemical current measured under varying applied voltages. (b) Plasmonic resonant wavelength shift under varying applied voltages. The wavelength shift becomes apparent before the current increases dramatically. (c) Mott-Schottky plot of the electrochromic device stack. The square inverse of the electrode capacitance is measured under 1 kHz AC applied with 10 mV amplitude. The abrupt change after the linearly spanning regime implies the drastic change in the system comes after the change in the density of the electrons. (d) The first derivative of the maximum scattering intensity difference from the pristine scattering intensity versus applied voltage implies there is no significant electrochemically driven dielectric environment change.[85]

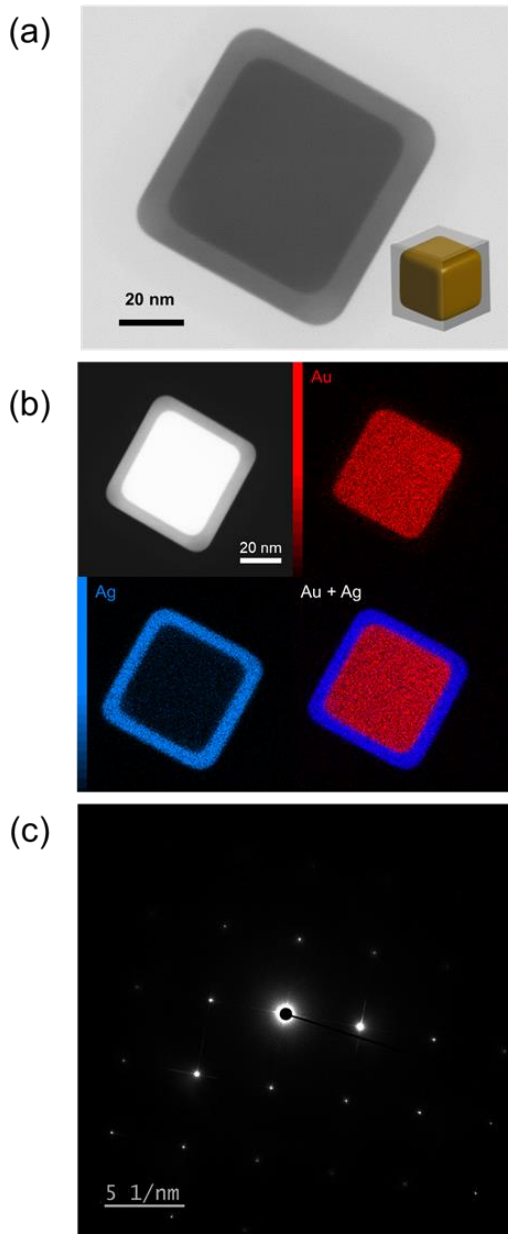

Figure 3.23. Electron microscopy analysis of the Au@Ag nanocubes. (a) Transmission electron microscope images of the Au@Ag nanocubes. (b) High-angle annular dark-field scanning transmission electron microscopy image of an Au@Ag nanocube (top-left) and energy dispersive spectroscopic elemental mapping of Au and Ag. (c) The electron diffraction pattern of the Au@Ag nanocube taken along the [100] zone axis.

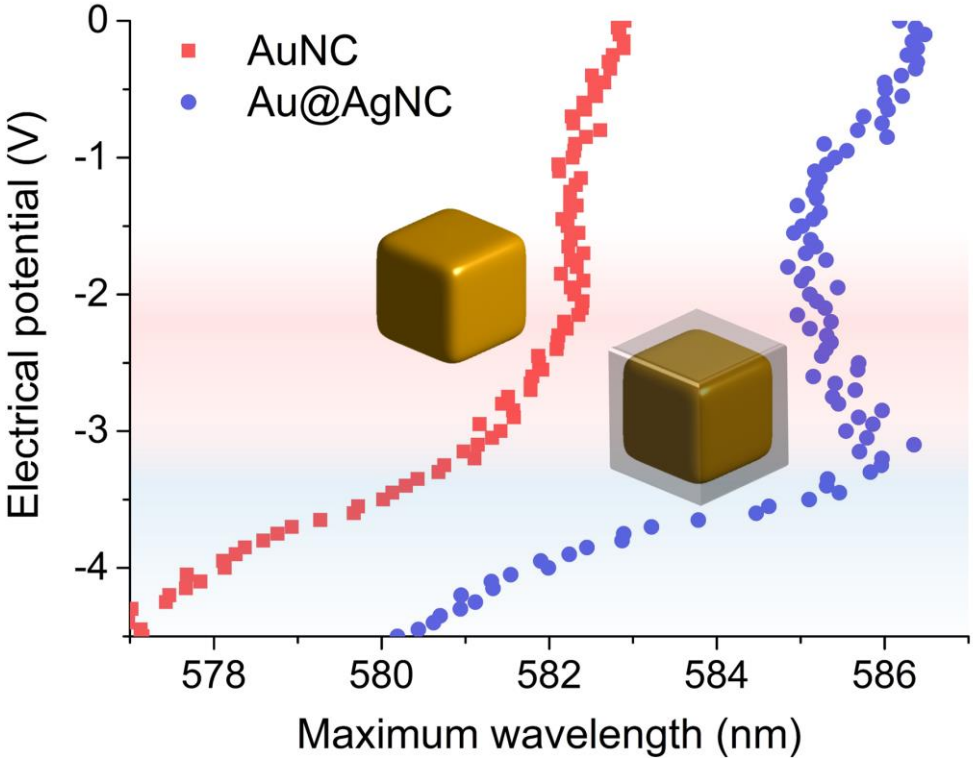

Figure 3.24. Surface element-dependent electrochromic response (plasmonic scattering maximum) of AuNCs and Au@AgNCs under a cathodic potential sweep and relevant electronic structure analysis.

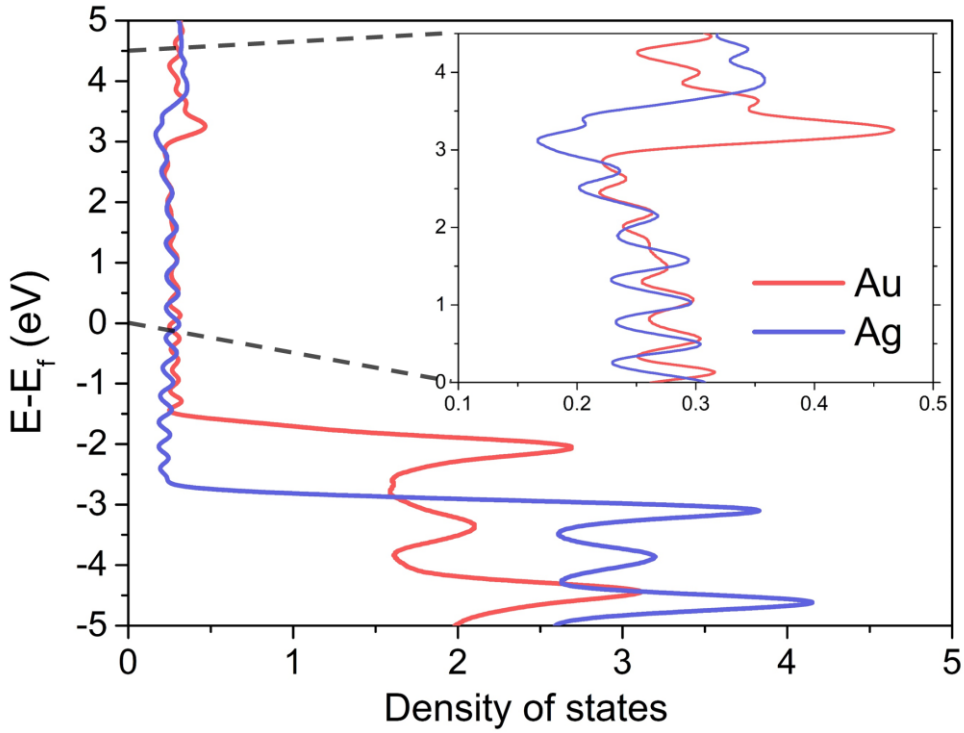

Figure 3.25. Surface element-dependent electrochromic response of AuNCs and Au@AgNCs and relevant electronic structure analysis. (a) The measured plasmonic scattering maximum wavelength of AuNCs and Au@AgNCs under a cathodic potential sweep. (b) The calculated DOSs for Au and Ag. Inset shows the magnified DOS profile at the corresponding potential range. (c) The calculated plasmonic resonance frequency shifts and their derivatives of the AuNCs and Au@AgNCs at the corresponding potential range.

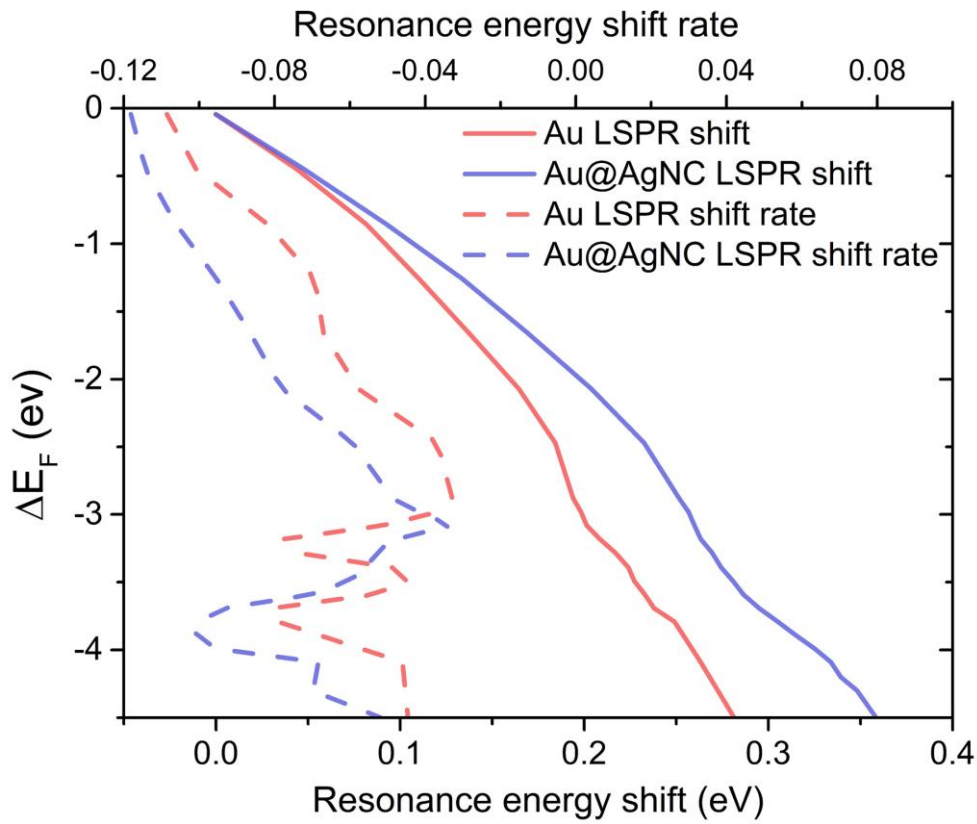

Figure 3.26. Surface element-dependent electrochromic response of AuNCs and Au@AgNCs and relevant electronic structure analysis. (a) The measured plasmonic scattering maximum wavelength of AuNCs and Au@AgNCs under a cathodic potential sweep. (b) The calculated DOSs for Au and Ag. Inset shows the magnified DOS profile at the corresponding potential range. (c) The calculated plasmonic resonance frequency shifts and their derivatives of the AuNCs and Au@AgNCs at the corresponding potential range.

3.4. Conclusion

We conclude the mechanisms of the voltage-dependent plasmonic properties of AuNCs placed on a transparent conductive electrode as follows:

(i) As mentioned above, in the low voltage region (I), capacitive charging and discharging of a metallic nanoparticle body initially leads to small changes in the LSPR. The shift is monotonic and simply analyzable by the classical model and geometric capacitance.

(ii) When the applied voltage reaches a certain level, the interaction of the nanoparticle with the surrounding medium becomes difficult to ignore. This may include ligand replacement, charge transfer to the medium, or chemical reactions. In the high positive voltage range (II), destructive oxidation of the metallic nanostructure occurs.

(iii) Under high negative voltages (III), unprecedented acceleration of the blue shift of the LSPR is observed. The plasmonic peak shift in the negative voltage region can be distinguished into two regions: a slow blue-shift at low voltages and a rapid blue-shift at high voltages. The more dramatic change in the high voltage region is hypothetically attributed to the largely drifted Fermi level and the new

trend in the relative permittivity change on the nanoparticle surface.

While reaching the equilibrium of the new Fermi energy level in the metallic solid and electrical double layer, the chemical potential of the metallic nanoparticle surface can embrace the rearrangement of the electrostatically adsorbed molecules.[19] The applied electric potential causes Fermi surface deformation in the Au lattice, thereby elevating the electronic energy level along the band structure. The Fermi level of the Au nanoparticle is elevated by ~3−4 eV, and it may span the 6*sp* band plateau.[86] The increased DOS lead to higher free electron population in the conduction band with the potential increment. As a result, the rate of the scattering spectral shift increases abruptly as the applied negative potential reaches the threshold potential.

In summary, we present the unconventional electrochromic behaviors of plasmonic metal nanoparticles as follows for the first time (**Figure 3.5**). We distinguished three different dynamic ranges and deduced the possible principles behind the characteristics in these ranges. The major factors considered to explain the different behaviors in the three different ranges include electrical charging, electrochemical interactions, Fermi level shifting, and particle oxidation. By comparing different metallic compositions on the surface of plasmonic nanocubes, the increased rate of spectral shift in the highly negative applied potential range can be clearly differentiated from the conventional charging of a geometrical capacitor.

EIS analysis predicted that the abrupt spectral shift is due to the dramatic increase in capacitance. While quantum capacitance, an intrinsic property of a material, is proportionally related to DOS of the capacitive material, the DOS profile of the surface element showed a positive correlation with the unpredicted spectral shift. It is noteworthy that the trend in the calculated LSPR shift caused by the additional charges at the elevated Fermi energy matched well with the experimental observations. In particular, the Fermi level change not only influences the electrical double layer in capacitive charging but also affects the rate of change of the free electron concentration. The increased quantum capacitance could be the principal reason for the changed spectral shift rate. Meanwhile, the nanocubes showed extraordinary stability up to the inflecting threshold. Furthermore, it was shown that the nanocubes repeatedly responded well over 10 cycles under the square potential waves alternating from 0 to −3.7 V with two different wave frequencies (0.05 and 0.25 Hz).

We also found that the electrochromic behavior of a capacitively charged plasmonic nanoparticle is dependent on the surface material. It was possible to verify the hypothesis on the anomalous phenomenon in a way of preparing nanocubes with different surface elements and comparing of their scattering properties. The findings in this work will facilitate broadening design strategies for electrical tuning of the plasmonic color, which have been mostly relied on the actuation of redox-active molecular layers among the four major mechanisms for the electrochromism of plasmonic metal

nanoparticles.[14] It is important to further investigate the electrochromic behaviors of other metals or alloys to prevent interband transition from the plasmonic process. The material-dependent and drastic electrochromic behavior of the plasmonic nanoparticle stretching out to the empirical potential limit will provide further insights for designing more efficient electrochemical spectroscopy tools, plasmonic catalysts, and optoelectronic devices such as smart windows or low-powered, always-on displays in a visible operation range.

Bibliography

(1) Hartland, G. V. Optical studies of dynamics in noble metal nanostructures. *Chem Rev* **2011,** *111* (6), 3858.

(2) Mie, G. Beiträge zur Optik trüber Medien, speziell kolloidaler Metallösungen. *Annalen der Physik* **1908,** *330* (3), 377.

(3) Fan, X.; Zheng, W.; Singh, D. J. Light scattering and surface plasmons on small spherical particles. *Light: Science & Applications* **2014,** *3* (6), e179.

(4) Narang, P.; Sundararaman, R.; Atwater, H. A. Plasmonic hot carrier dynamics in solid-state and chemical systems for energy conversion. *Nanophotonics* **2016,** *5* (1), 96.

(5) Saha, K.; Agasti, S. S.; Kim, C.; Li, X.; Rotello, V. M. Gold nanoparticles in chemical and biological sensing. *Chem Rev* **2012,** *112* (5), 2739.

(6) Boltasseva, A.; Atwater, H. A. Materials science. Low-loss plasmonic metamaterials. *Science* **2011,** *331* (6015), 290.

(7) Garcia, G.; Buonsanti, R.; Runnerstrom, E. L.; Mendelsberg, R. J.; Llordes, A.; Anders, A.; Richardson, T. J.; Milliron, D. J. Dynamically modulating the surface plasmon resonance of doped semiconductor nanocrystals. *Nano Lett* **2011,** *11* (10), 4415.

(8) Ha, M.; Kim, J. H.; You, M.; Li, Q.; Fan, C.; Nam, J. M. Multicomponent Plasmonic Nanoparticles: From Heterostructured Nanoparticles to Colloidal Composite Nanostructures. *Chem Rev* **2019,** *119* (24), 12208.

(9) Kwon, S. G.; Krylova, G.; Phillips, P. J.; Klie, R. F.; Chattopadhyay, S.; Shibata, T.; Bunel, E. E.; Liu, Y.; Prakapenka, V. B.; Lee, B.et al. Heterogeneous nucleation and shape transformation of multicomponent metallic nanostructures. *Nat Mater* **2015,** *14* (2), 215.

(10) Cortie, M. B.; McDonagh, A. M. Synthesis and optical properties of hybrid and alloy plasmonic nanoparticles. *Chem Rev* **2011,** *111* (6), 3713.

(11) Granasy, L.; Podmaniczky, F.; Toth, G. I.; Tegze, G.; Pusztai, T. Heterogeneous nucleation of/on nanoparticles: a density functional study using the phase-field crystal model. *Chem Soc Rev* **2014,** *43* (7), 2159.

(12) Lin, M.; Kim, G. H.; Kim, J. H.; Oh, J. W.; Nam, J. M. Transformative Heterointerface Evolution and Plasmonic Tuning of Anisotropic Trimetallic Nanoparticles. *J Am Chem Soc* **2017,** *139* (30), 10180.

(13) Park, J.-E.; Kim, K.; Jung, Y.; Kim, J.-H.; Nam, J.-M. Metal Nanoparticles for Virus Detection. *ChemNanoMat* **2016,** *2* (10), 927.

(14) Kim, Y.; Cha, S.; Kim, J. H.; Oh, J. W.; Nam, J. M. Electrochromic

response and control of plasmonic metal nanoparticles. *Nanoscale* **2021,** *13* (21), 9541.

(15) Choi, J.; Kim, J. H.; Oh, J. W.; Nam, J. M. Surface-enhanced Raman scattering-based detection of hazardous chemicals in various phases and matrices with plasmonic nanostructures. *Nanoscale* **2019,** *11* (43), 20379.

(16) Park, J. E.; Jung, Y.; Kim, M.; Nam, J. M. Quantitative Nanoplasmonics. *ACS Cent Sci* **2018,** *4* (10), 1303.

(17) Byers, C. P.; Zhang, H.; Swearer, D. F.; Yorulmaz, M.; Hoener, B. S.; Huang, D.; Hoggard, A.; Chang, W.-S.; Mulvaney, P.; Ringe, E.et al. From tunable core-shell nanoparticles to plasmonic drawbridges: Active control of nanoparticle optical properties. *Science Advances* **2015,** *1* (11), e1500988.

(18) Peng, J.; Jeong, H. H.; Lin, Q.; Cormier, S.; Liang, H. L.; De Volder, M. F. L.; Vignolini, S.; Baumberg, J. J. Scalable electrochromic nanopixels using plasmonics. *Sci Adv* **2019,** *5* (5), eaaw2205.

(19) Scanlon, M. D.; Peljo, P.; Mendez, M. A.; Smirnov, E.; Girault, H. H. Charging and discharging at the nanoscale: Fermi level equilibration of metallic nanoparticles. *Chem Sci* **2015,** *6* (5), 2705.

(20) Warren, S. C.; Walker, D. A.; Grzybowski, B. A. Plasmoelectronics: coupling plasmonic excitation with electron flow. *Langmuir* **2012,** *28* (24), 9093.

(21) Anker, J. N.; Hall, W. P.; Lyandres, O.; Shah, N. C.; Zhao, J.; Van Duyne, R. P. Biosensing with plasmonic nanosensors. *Nat Mater* **2008,** *7* (6), 442.

(22) Boisselier, E.; Astruc, D. Gold nanoparticles in nanomedicine: preparations, imaging, diagnostics, therapies and toxicity. *Chem Soc Rev* **2009,** *38* (6), 1759.

(23) Nam, J. M.; Stoeva, S. I.; Mirkin, C. A. Bio-bar-code-based DNA detection with PCR-like sensitivity. *J Am Chem Soc* **2004,** *126* (19), 5932.

(24) Gubala, V.; Harris, L. F.; Ricco, A. J.; Tan, M. X.; Williams, D. E. Point of care diagnostics: status and future. *Anal Chem* **2012,** *84* (2), 487.

(25) Han, K. N.; Choi, J. S.; Kwon, J. Three-dimensional paper-based slip device for one-step point-of-care testing. *Sci Rep* **2016,** *6*, 25710.

(26) Ngom, B.; Guo, Y.; Wang, X.; Bi, D. Development and application of lateral flow test strip technology for detection of infectious agents and chemical contaminants: a review. *Anal Bioanal Chem* **2010,** *397* (3), 1113.

(27) Lei, J.; Ju, H. Signal amplification using functional nanomaterials for biosensing. *Chem Soc Rev* **2012,** *41* (6), 2122.

(28) Cao, X.; Ye, Y.; Liu, S. Gold nanoparticle-based signal amplification for biosensing. *Anal Biochem* **2011,** *417* (1), 1.

(29) Cleator, G. M.; Klapper, P. E.; Thornton, J.; Cropper, L.; Reid, H.

Immuno-gold silver staining in the diagnosis of herpes encephalitis. *Journal of Neurology, Neurosurgery & Psychiatry* **1986,** *49* (10), 1209.

(30) Danscher, G.; Norgaard, J. O. Light microscopic visualization of colloidal gold on resin-embedded tissue. *J Histochem Cytochem* **1983,** *31* (12), 1394.

(31) Liu, R.; Zhang, Y.; Zhang, S.; Qiu, W.; Gao, Y. Silver Enhancement of Gold Nanoparticles for Biosensing: From Qualitative to Quantitative. *Applied Spectroscopy Reviews* **2013,** *49* (2), 121.

(32) Taton, T. A.; Mirkin, C. A.; Letsinger, R. L. Scanometric DNA array detection with nanoparticle probes. *Science* **2000,** *289* (5485), 1757.

(33) Cao, Y. C.; Jin, R.; Mirkin, C. A. Nanoparticles with Raman spectroscopic fingerprints for DNA and RNA detection. *Science* **2002,** *297* (5586), 1536.

(34) Park, S. J.; Taton, T. A.; Mirkin, C. A. Array-based electrical detection of DNA with nanoparticle probes. *Science* **2002,** *295* (5559), 1503.

(35) Xu, S.; Ji, X.; Xu, W.; Li, X.; Wang, L.; Bai, Y.; Zhao, B.; Ozaki, Y. Immunoassay using probe-labelling immunogold nanoparticles with silver staining enhancement via surface-enhanced Raman scattering. *Analyst* **2004,** *129* (1), 63.

(36) Alvarez-Puebla, R. A.; Liz-Marzan, L. M. SERS-based diagnosis and biodetection. *Small* **2010,** *6* (5), 604.

(37) Chevallet, M.; Luche, S.; Rabilloud, T. Silver staining of proteins in polyacrylamide gels. *Nat Protoc* **2006,** *1* (4), 1852.

(38) Kislenko, V. N.; Oliynyk, L. P. Complex formation of polyethyleneimine with copper(II), nickel(II), and cobalt(II) ions. *Journal of Polymer Science Part A: Polymer Chemistry* **2002,** *40* (7), 914.

(39) Moller, R.; Powell, R. D.; Hainfeld, J. F.; Fritzsche, W. Enzymatic control of metal deposition as key step for a low-background electrical detection for DNA chips. *Nano Lett* **2005,** *5* (7), 1475.

(40) Kim, D.; Daniel, W. L.; Mirkin, C. A. Microarray-based multiplexed scanometric immunoassay for protein cancer markers using gold nanoparticle probes. *Anal Chem* **2009,** *81* (21), 9183.

(41) Mott, D.; Galkowski, J.; Wang, L.; Luo, J.; Zhong, C. J. Synthesis of size-controlled and shaped copper nanoparticles. *Langmuir* **2007,** *23* (10), 5740.

(42) Kawamura, G.; Alvarez, S.; Stewart, I. E.; Catenacci, M.; Chen, Z.; Ha, Y. C. Production of Oxidation-Resistant Cu-Based Nanoparticles by Wire Explosion. *Sci Rep* **2015,** *5*, 18333.

(43) Owczarzy, R.; Moreira, B. G.; You, Y.; Behlke, M. A.; Walder, J. A. Predicting stability of DNA duplexes in solutions containing magnesium and monovalent cations. *Biochemistry* **2008,** *47* (19), 5336.

(44) Gawande, M. B.; Goswami, A.; Felpin, F. X.; Asefa, T.; Huang, X.; Silva, R.; Zou, X.; Zboril, R.; Varma, R. S. Cu and Cu-Based Nanoparticles: Synthesis and Applications in Catalysis. *Chem Rev* **2016,** *116* (6), 3722.

(45) Lee, Y. K.; Kim, S.; Oh, J. W.; Nam, J. M. Massively parallel and highly quantitative single-particle analysis on interactions between nanoparticles on supported lipid bilayer. *J Am Chem Soc* **2014,** *136* (10), 4081.

(46) Bragg, T. S.; Robertson, D. L. Nucleotide sequence and analysis of the lethal factor gene (lef) from Bacillus anthracis. *Gene* **1989,** *81* (1), 45.

(47) Inglesby, T. V.; O'Toole, T.; Henderson, D. A.; Bartlett, J. G.; Ascher, M. S.; Eitzen, E.; Friedlander, A. M.; Gerberding, J.; Hauer, J.; Hughes, J.et al. Anthrax as a biological weapon, 2002: updated recommendations for management. *JAMA* **2002,** *287* (17), 2236.

(48) Thomas, M. C.; Shields, M. J.; Hahn, K. R.; Janzen, T. W.; Goji, N.; Amoako, K. K. Evaluation of DNA extraction methods for Bacillus anthracis spores isolated from spiked food samples. *J Appl Microbiol* **2013,** *115* (1), 156.

(49) Rougeaux, C.; Becher, F.; Ezan, E.; Tournier, J. N.; Goossens, P. L. In vivo dynamics of active edema and lethal factors during anthrax. *Sci Rep* **2016,** *6*, 23346.

(50) Jones, M. K.; Watanabe, M.; Zhu, S.; Graves, C. L.; Keyes, L. R.; Grau, K. R.; Gonzalez-Hernandez, M. B.; Iovine, N. M.; Wobus, C. E.; Vinje, J.et al. Enteric bacteria promote human and mouse norovirus infection of B cells. *Science* **2014,** *346* (6210), 755.

(51) Knight, A.; Li, D.; Uyttendaele, M.; Jaykus, L. A. A critical review of methods for detecting human noroviruses and predicting their infectivity. *Crit Rev Microbiol* **2013,** *39* (3), 295.

(52) Xuan, Z.; Li, M.; Rong, P.; Wang, W.; Li, Y.; Liu, D. Plasmonic ELISA based on the controlled growth of silver nanoparticles. *Nanoscale* **2016,** *8* (39), 17271.

(53) Liu, D.; Yang, J.; Wang, H. F.; Wang, Z.; Huang, X.; Wang, Z.; Niu, G.; Hight Walker, A. R.; Chen, X. Glucose oxidase-catalyzed growth of gold nanoparticles enables quantitative detection of attomolar cancer biomarkers. *Anal Chem* **2014,** *86* (12), 5800.

(54) Liu, H.; Rong, P.; Jia, H.; Yang, J.; Dong, B.; Dong, Q.; Yang, C.; Hu, P.; Wang, W.; Liu, H.et al. A Wash-Free Homogeneous Colorimetric Immunoassay Method. *Theranostics* **2016,** *6* (1), 54.

(55) Rodriguez-Lorenzo, L.; de la Rica, R.; Alvarez-Puebla, R. A.; Liz-Marzan, L. M.; Stevens, M. M. Plasmonic nanosensors with inverse sensitivity by means of enzyme-guided crystal growth. *Nat Mater* **2012,** *11* (7), 604.

(56) Zhang, L.; Li, Y.; Li, D. W.; Jing, C.; Chen, X.; Lv, M.; Huang, Q.; Long, Y. T.; Willner, I. Single gold nanoparticles as real-time optical

probes for the detection of NADH-dependent intracellular metabolic enzymatic pathways. *Angew Chem Int Ed Engl* **2011,** *50* (30), 6789.

(57) Peng, T.; Qin, W.; Wang, K.; Shi, J.; Fan, C.; Li, D. Nanoplasmonic imaging of latent fingerprints with explosive RDX residues. *Anal Chem* **2015,** *87* (18), 9403.

(58) Xu, X.; Georganopoulou, D. G.; Hill, H. D.; Mirkin, C. A. Homogeneous detection of nucleic acids based upon the light scattering properties of silver-coated nanoparticle probes. *Anal Chem* **2007,** *79* (17), 6650.

(59) Zada, A.; Muhammad, P.; Ahmad, W.; Hussain, Z.; Ali, S.; Khan, M.; Khan, Q.; Maqbool, M. Surface Plasmonic-Assisted Photocatalysis and Optoelectronic Devices with Noble Metal Nanocrystals: Design, Synthesis, and Applications. *Advanced Functional Materials* **2019,** *30* (7).

(60) Hengelin, A.; Mulvany, P.; Linnert, T. Chemistry of Agn, Aggregates in Aqueous Solution: Non-metallic Oligomeric Clusters and Metallic Particles. *Faraday Discuss* **1991,** *92*, 31.

(61) Ung, T.; Giersig, M.; Dustan, D.; Mulvaney, P. Spectroelectrochemistry of Colloidal Silver. *Langmuir* **1997,** *13*, 1773.

(62) Hoener, B. S.; Kirchner, S. R.; Heiderscheit, T. S.; Collins, S. S. E.; Chang, W.-S.; Link, S.; Landes, C. F. Plasmonic Sensing and Control of Single-Nanoparticle Electrochemistry. *Chem* **2018,** *4* (7), 1560.

(63) Di Martino, G.; Turek, V. A.; Lombardi, A.; Szabo, I.; de Nijs, B.; Kuhn, A.; Rosta, E.; Baumberg, J. J. Tracking Nanoelectrochemistry Using Individual Plasmonic Nanocavities. *Nano Lett* **2017,** *17* (8), 4840.

(64) Jing, C.; Gu, Z.; Xie, T.; Long, Y. T. Color-coded imaging of electrochromic process at single nanoparticle level. *Chem Sci* **2016,** *7* (8), 5347.

(65) Willets, K. A. Supercharging Superlocalization Microscopy: How Electrochemical Charging of Plasmonic Nanostructures Uncovers Hidden Heterogeneity. *ACS Nano* **2019,** *13* (6), 6145.

(66) Chirea, M.; Collins, S. S.; Wei, X.; Mulvaney, P. Spectroelectrochemistry of Silver Deposition on Single Gold Nanocrystals. *J Phys Chem Lett* **2014,** *5* (24), 4331.

(67) Jing, C.; Gu, Z.; Long, Y. T. Imaging electrocatalytic processes on single gold nanorods. *Faraday Discuss* **2016,** *193*, 371.

(68) Novo, C.; Funston, A. M.; Mulvaney, P. Direct observation of chemical reactions on single gold nanocrystals using surface plasmon spectroscopy. *Nat Nanotechnol* **2008,** *3* (10), 598.

(69) Mulvaney, P. Surfacce plasmon spectroscopy of nanosized metal particles. *Langmuir* **1996,** *12* (3), 788.

(70) Runnerstrom, E. L.; Llordes, A.; Lounis, S. D.; Milliron, D. J. Nanostructured electrochromic smart windows: traditional materials

and NIR-selective plasmonic nanocrystals. *Chem Commun (Camb)* **2014,** *50* (73), 10555.

(71) Jeon, J.-W.; Ledin, P. A.; Geldmeier, J. A.; Ponder, J. F.; Mahmoud, M. A.; El-Sayed, M.; Reynolds, J. R.; Tsukruk, V. V. Electrically Controlled Plasmonic Behavior of Gold Nanocube@Polyaniline Nanostructures: Transparent Plasmonic Aggregates. *Chemistry of Materials* **2016,** *28* (8), 2868.

(72) Lu, W.; Jiang, N.; Wang, J. Active Electrochemical Plasmonic Switching on Polyaniline-Coated Gold Nanocrystals. *Adv Mater* **2017,** *29* (8).

(73) Stec, G. J.; Lauchner, A.; Cui, Y.; Nordlander, P.; Halas, N. J. Multicolor Electrochromic Devices Based on Molecular Plasmonics. *ACS Nano* **2017,** *11* (3), 3254.

(74) Byers, C. P.; Hoener, B. S.; Chang, W. S.; Yorulmaz, M.; Link, S.; Landes, C. F. Single-particle spectroscopy reveals heterogeneity in electrochemical tuning of the localized surface plasmon. *J Phys Chem B* **2014,** *118* (49), 14047.

(75) Novo, C.; Funston, A. M.; Gooding, A. K.; Mulvaney, P. Electrochemical charging of single gold nanorods. *J Am Chem Soc* **2009,** *131* (41), 14664.

(76) Brown, A. M.; Sheldon, M. T.; Atwater, H. A. Electrochemical Tuning of the Dielectric Function of Au Nanoparticles. *ACS Photonics* **2015,** *2* (4), 459.

(77) Mulvaney, P.; Pérez-Juste, J.; Giersig, M.; Liz-Marzán, L. M.; Pecharromán, C. Drastic Surface Plasmon Mode Shifts in Gold Nanorods Due to Electron Charging. *Plasmonics* **2006,** *1* (1), 61.

(78) Manjavacas, A.; Garcia de Abajo, F. J. Tunable plasmons in atomically thin gold nanodisks. *Nat Commun* **2014,** *5*, 3548.

(79) Hoener, B. S.; Zhang, H.; Heiderscheit, T. S.; Kirchner, S. R.; De Silva Indrasekara, A. S.; Baiyasi, R.; Cai, Y.; Nordlander, P.; Link, S.; Landes, C. F.et al. Spectral Response of Plasmonic Gold Nanoparticles to Capacitive Charging: Morphology Effects. *J Phys Chem Lett* **2017,** *8* (12), 2681.

(80) Zapata Herrera, M.; Aizpurua, J.; Kazansky, A. K.; Borisov, A. G. Plasmon Response and Electron Dynamics in Charged Metallic Nanoparticles. *Langmuir* **2016,** *32* (11), 2829.

(81) Park, J. E.; Lee, Y.; Nam, J. M. Precisely Shaped, Uniformly Formed Gold Nanocubes with Ultrahigh Reproducibility in Single-Particle Scattering and Surface-Enhanced Raman Scattering. *Nano Lett* **2018,** *18* (10), 6475.

(82) Meena, S. K.; Celiksoy, S.; Schafer, P.; Henkel, A.; Sonnichsen, C.; Sulpizi, M. The role of halide ions in the anisotropic growth of gold nanoparticles: a microscopic, atomistic perspective. *Phys Chem Chem Phys* **2016,** *18* (19), 13246.

(83) Al-Zubeidi, A.; Hoener, B. S.; Collins, S. S. E.; Wang, W.; Kirchner,

S. R.; Hosseini Jebeli, S. A.; Joplin, A.; Chang, W. S.; Link, S.; Landes, C. F. Hot Holes Assist Plasmonic Nanoelectrode Dissolution. *Nano Lett* **2019,** *19* (2), 1301.

(84) Aoki, K. J.; Chen, J.; Zeng, X.; Wang, Z. Decrease in the double layer capacitance by faradaic current. *RSC Advances* **2017,** *7* (36), 22501.

(85) Byers, C. P.; Hoener, B. S.; Chang, W. S.; Link, S.; Landes, C. F. Single-Particle Plasmon Voltammetry (spPV) for Detecting Anion Adsorption. *Nano Lett* **2016,** *16* (4), 2314.

(86) Rangel, T.; Kecik, D.; Trevisanutto, P. E.; Rignanese, G. M.; Van Swygenhoven, H.; Olevano, V. Band structure of gold from many-body perturbation theory. *Physical Review B* **2012,** *86* (12).

초 록

플라즈몬 공명은 외부 전기장에 따른 전도성 전자들의 정합 진동이며, 물질과 빛의 강력한 상호작용을 통하여 다양한 광학적 과정을 효과적으로 증대한다. 특히 플라즈모닉 나노물질은 비범할 정도의 효율로 빛을 산란하며, 증가된 원거리장 방사 세기는 바이오센서, 육안 검출을 위한 비색분석, 스마트 디스플레이 등의 발전된 설계를 위해 활용할 수 있다. 그러나 단조롭고 제한된 특성을 보이는 단일 조성의 나노 구조만으로는 플라즈모닉 나노물질의 산란이 갖는 모든 잠재력을 충분히 발휘할 수 없다. 반면 다조성계 기반 체계에서는 개별 요소로부터 오는 물리 화학적 특성의 상승적 조합이나 결합된 구조로부터 오는 새로운 특성과 같은 다양한 성질과 가능성을 보일 수 있다.

이 논문에서는 플라즈모닉 다조성계 나노구조의 산란 신호를 조절하기 위한 화학적 및 전기적 전략과 다조성계 시스템의 이점을 보여주는 최적의 예를 제시한다. 제1 장에서는 다조성계 나노구조의 플라즈몬 특성과 이를 응용할 때 플라즈모닉 산란의 조절 및 증강으로부터 기대할 수 있는 장점을 소개한다. 제2 장에서는 매우 특이적이고 잘 정의된 구리 다면체 나노쉘(CuPN)의 과성장을 위한 화학적 접근법 개발을 소개한다. 새로운 과성장 법은 바이오 검지를 위해 사용되는 금 나노입자 프로브의 빛 산란에 적용하였다. CuPN은 금 나노입자 표면에서만 선택적이고 제어 가능하도록 형성되었으며 비 특이적 신호 증폭을 나타내지 않았다. 이렇게 새로 개발된 다조성계 코어-쉘을 형성하는 고분자 기반 화학적 합성법이 DNA와

바이러스의 정량 가능한 고감도 육안 검출법의 개발에 사용됨을 보였다. 제3 장은 금 나노 큐브의 색전현상에서 새롭게 발견한 비정상적 거동을 포함한다. 나노 큐브의 플라즈몬 산란은 높은 음전위 영역에서 더 높은 진동수 변화율을 보였다. 고전적인 이해를 벗어나는 이러한 예기치 않은 변화는 플라즈모닉 재료의 물질 특이적인 양자 역학적 전자 구조에 기인한다. 플라즈모닉 재료를 구성하는 금속의 상태 밀도로부터 유도될 수 있는 양자 정전용량의 상당한 역할은, 은-금 코어-쉘 나노 큐브를 형성하여 표면 원소를 바꾸는 방법을 통해 처음으로 증명할 수 있었다.

주요어: 플라즈모닉 산란, 다조성계 나노입자, 다면체 코어-쉘 나노입자, 바이오센서, 육안 검지, 색전현상

학 번: 2014-21221